INNOVATIVE SENSORS USING NITRIDE SEMICONDUCTOR MATERIALS FOR THE DETECTION OF EXHAUST GASES AND WATER POLLUTANTS

A Dissertation
Presented to
The Academic Faculty

By

Chris Bishop

In Partial Fulfillment
of the Requirements for the Degree
Doctor of Philosophy
in
Electrical and Computer Engineering

School of Electrical and Computer Engineering
Georgia Institute of Technology
May 2015

INNOVATIVE SENSORS USING NITRIDE SEMICONDUCTOR MATERIALS FOR THE DETECTION OF EXHAUST GASES AND WATER POLLUTANTS

Approved by:

Dr. Jean Paul Salvestrini, Committee Chair
Professor, School of ECE
Georgia Institute of Technology

Dr. Jeffrey Davis
Professor, School of ECE
Georgia Institute of Technology

Dr. Abdallah Ougazzaden, Advisor
Professor, School of ECE
Georgia Institute of Technology

Dr. Alexandre Locquet
Professor, School of ECE
Georgia Institute of Technology

Dr. Paul Voss, Co-advisor
Professor, School of ECE
Georgia Institute of Technology

Dr. Thomas Sanders
Professor, School of Materials and Science Engineering
Georgia Institute of Technology

Date Approved: April 2, 2015

ACKNOWLEDGMENT

This work was supported by PSA Peugeot Citroën as part of the OpenLab of Metz, and by the Region of Lorraine. I would like to thank my advisers, Dr. Abdallah Ougazzaden and Dr. Paul Voss, for advising and teaching me during this research project. I would also like to thank the other committee members, Dr. Jean Paul Salvestrini, Dr. Tom Sanders, Dr. Jeff Davis, and Dr. Alexandre Locquet, for their input and advice during the proposal and defense. Dr. Jean Paul Salvestrini provided valuable input with the experimental portion of the research, including help with the experimental setups. He also provided in depth discussions regarding the physical interpretations of the sensor devices and chemical mechanisms. Yacine Halfaya contributed to the material characterizations and sensors experiments. Jeremy Streque and Laurent Bouvot provided cleanroom training and help with device processing. Ali Soltani also provided device processing that was essential for the HEMT sensor fabrication. Xin Li, Suresh Sundaram, Simon Gautier, and Tarik Moudakir contributed to the materials growth, and Youssef El Gmili contributed to characterization of the materials. Finally, I would like to thank my family and all of my friends, colleagues, and staff at Georgia Tech Lorraine for their encouragement and support throughout this thesis work. This especially includes my parents, Mary and John Duncan and Kip Bishop, my sister, Kelsey Bishop, and the Ph.D. students that I have gotten to know well over the last four years, Peter McKeon, Renaud Puybaret, Konstantinos Pantzas, Jeramy Dickerson, and Matthew Jordan.

TABLE OF CONTENTS

LIST OF TABLES

LIST OF FIGURES

CHAPTER 1

INTRODUCTION

1.1 Environmental and economic impact of detecting and controlling diesel exhaust gases

An important application of gas sensing is the detection of harmful gases and chemicals that are released as byproducts of the diesel automotive combustion process. In the combustion of diesel fuel, an excess of air is introduced in the combustion which results in the generation of harmful NO, NO_2, and NH_3 (nitric oxide, nitrogen dioxide, and ammonia, respectfully) that are not as prevalent in the combustion of regular gasoline. In addition to these gases, other gases and molecules such as CO, CO_2, hydrocarbons, and particulate matter are produced in the mixture of diesel exhaust gas, which is then released from the automobile into the atmosphere. When these gases are introduced into the atmosphere as automotive exhaust, they can be responsible for many negative health and environmental hazards. For example, nitrogen oxides and ammonia are known carcinogens, and they break down into nitric acid when exposed to moisture which can contribute to acid rain [7]. Additionally, CO_2 accounts for a large proportion of greenhouse gases which is a large contributor to global warming [8]. For these reasons, Europe, as well as the United States, Japan, and China, have enforced strict emission standards on all exhaust gases and are periodically updated and released by the respective regulatory authorities (e.g., the European Commission and United States Environmental Protection Agency). These regulations must be met by all automotive vehicles that are produced before they can be sold to the public, meaning that the ability to accurately control the emissions of these gases has a direct economic impact. Additionally, the emission standards are aligned to the needs of each location. For example, automotive vehicles using diesel fuel currently accounts for over 50% of the total automobiles in Europe [9], and therefore nitrogen oxides and particulate matter are among the main concerns for the present EU standards; the US is currently more

focused on CO and CO_2 emissions. It is interesting to note that there is currently a rapid decline in the production of diesel automobiles in Europe, mainly due to increasing taxes on diesel fuel that are largely due to the inability to control the pollution from diesel exhaust gases [10]. Diesel production in the US, on the other hand, is expected to increase in the next few years, and so the focus on regulations is predicted to shift more towards nitrogen oxides. In China, the emission standards are modeled after the EU regulations, but the exhaust systems currently in use are unable to meet the strict NO and NO_2 requirements. These are all indications of the severe environmental and economic impacts that are directly correlated with the ability to accurately and quickly detect and manage exhaust gases. The research presented in this thesis is being conducted at the Lorraine campus of Georgia Institute of Technology as part of an Open Lab project with Peugeot PSA in France. Therefore, the majority of the work focuses on meeting the needs of the upcoming EU diesel exhaust regulations, specifically regarding the detection of NO, NO_2, and NH_3 gases. We do, however, give consideration to other global needs as well as some other applications of gas and chemical detection.

1.2 EU emission standards for diesel automotives (past and current)

The various stages of EU diesel emission standards are listed in Table 1, beginning with Euro I (introduced in 1993) and showing the progression in regulations leading up to the current standards. In each stage, the maximum allowable emission of gas or particle is listed.

Note that each standard is given in units of mg/km, which is a method of accounting for variations depending in fuel consumption. For example, different regimes of operations of diesel vehicles such as highway driving, accelerating, climbing hills, etc., will consume different amounts of fuel and thus alter the total concentration of gas or particles in the exhaust. However, the common metric of interest in sensors applications is the amount of gas detected in parts per million (ppm); therefore, this metric is frequently used in this

Table 1. EU diesel emission standards (Euro 1 - Euro 6) for maximum allowable concentrations in exhaust gas. All units are mg/km.

Standard	Euro 1 (1993)	Euro 2 (1996)	Euro 3 (2000)	Euro 4 (2005)	Euro 5 (2008)	Euro 6 (2014)
Nitrogen oxides (NO_x)	-	-	500	250	180	80
Ammonia (NH_3)	-	-	-	-	-	-
Carbon monoxide (CO)	2720	1000	640	500	500	500
HC + NO_x	970	900	560	300	230	170
Particulate matter (PM)	140	100	50	25	5	5
Hydrocarbons (HC)	-	-	-	-	-	-

research when analyzing sensor performances for various operation regimes.

The important thing to note about the trend in the exhaust regulations is that the maximum allowable concentration of each standard continues to decrease with each new stage, and this trend is expected to continue into the next stage (Euro 7). To meet the regulations, several diesel exhaust components are in place to reduce or eliminate these gases from the exhaust, and many of these components include sensors that are able to detect the target molecules. In many cases, such as for NO_x, the current regulations are already at the limits of the sensor capabilities in the exhaust system. This means that there is a strong need for a new generation of sensors that will be able to keep up with the demand of future exhaust regulations.

1.3 Pollution control systems in diesel exhaust

This section explains the different components of the diesel exhaust system currently used by Peugeot PSA and how they work to reduce exhaust gas pollution. The diesel exhaust (Figure 1) is broken into 3 main systems that each function to reduce specific pollutants from the exhaust gas; these are the diesel oxidation catalyst (DOC), selective catalytic reduction (SCR), and the particulate filter.

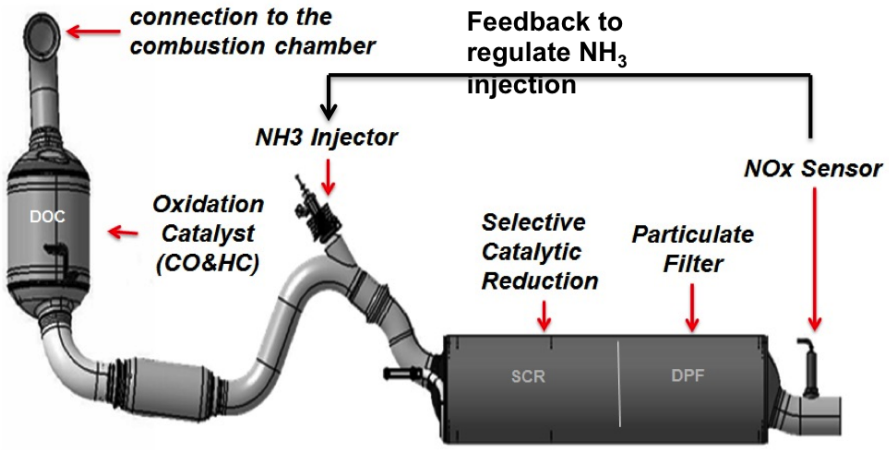

Figure 1. Diesel exhaust system including the DOC, SCR, and PF pollution control systems

After combustion of diesel fuel in the engine, the exhaust gas containing the pollutants first passes through the DOC. Here, oxidation reactions reduce unburned hydrocarbons and CO into water and CO_2 according to the following reactions [11]:

$$C_nH_m + O_2 \rightarrow CO_2 + H_2O \tag{1}$$

$$CO + 12O_2 \rightarrow CO_2 \tag{2}$$

Once the CO and HC is removed from the exhaust gas mixture, it passes into the SCR. A solution of urea, sold commercially as AdBlue, is also injected into the SCR and breaks down into ammonia at temperatures above 180°C. The SCR system uses the NH_3 to reduce NO and NO_2 into nitrogen and water according to the following reactions [12]:

$$4NH_3 + 4NO + O_2 \rightarrow 4N_2 + 6H_20 \tag{3}$$

$$2NH_3 + NO + NO_2 \rightarrow 2N_2 + 3H_2O \tag{4}$$

$$8NH_3 + 6NO_2 \rightarrow 7N_2 + 12H_2O \tag{5}$$

According to these reactions, the concentration of injected NH_3 depends on the relative amount of NO and NO_2 present in the exhaust gas. In current SCR systems, the concentration of injected NH_3 is controlled by an NO_x sensor at the exhaust output. Typically, the sensor is placed just after the particulate filter, which functions to remove particulate matter from the exhaust gas mixture. Temperatures at the output typically reach up to 600°C during normal operation, but can also reach up to 900°C for periods of 30s during the filter regeneration. At the output, the sensors measure the amount of NOx that was not reduced, and this information from this sensor is sent to the on-board diagnostic system (OBD) that uses a predictive algorithm to estimate the required adjustment of NH_3 injection. The sensors may also be placed just before the SCR where the temperature does not exceed 600°C; however, at this location it is subject to damage from contact with unfiltered particulate matter.

Current NO_x sensors used in these systems are based on the lambda probe/Nernst cell technology and cannot selectively detect between NO and NO_2, meaning that only the total NO_x is detected. Furthermore, they have limited detection limits (>10 ppm) that are already near the limit of the current regulation stage (Euro 6) and can only operate if heated above 350°C [13]. Because of these shortcomings, the current SCR system often results in either an excess of harmful NO_x or NH_3 being released into the atmosphere as pollutants. Clearly, the limiting factor for the accuracy and efficiency of the reduction of nitrogen oxides by the SCR system is the NO_x sensor. This means that the NO_x sensor plays a large role in the ability to meet EU exhaust regulations.

It should also be noted that the amount of NO and NO_2 in the exhaust gas is proportional to the fuel efficiency at which the vehicle is being operated. Operating at maximum fuel efficiency (1g fuel/18g air) means using a leaner mix (i.e. more oxygen) of diesel fuel, which naturally increases the nitrogen oxides in the combustion process. Thus, a more accurate NO_x sensor could be used by the OBD to control the fuel/air mixture, and could potentially allow for better fuel efficiency while remaining within the pollution restrictions

of the EU regulations. This would ultimately reduce costs to the customer.

There is not currently an NH_3 sensor included in the SCR system to accurately regulate the amount of NH_3 that is injected, and thus this process again relies on predictive algorithms. This is largely due to a technology gap in ammonia sensors; namely, there aren't any ammonia sensors designed for automotive exhausts that are reliable enough to be used commercially. Thus, including a sensor that could accurately detect NH_3 from exhaust gas would vastly improve the SCR system. Having an NH_3 sensor could also enable different SCR operation modes; for example, instead of only directly measuring the NO and NO_2 at the exhaust output, one could additionally measure the excess NH_3 from the reduction reactions to improve the overall SCR accuracy.

1.4 Predicted future EU emission standards and NO_x sensor requirements

Euro 7 will be the next stage in EU diesel emission standards and is expected in 2015, although the exact date and standards are not known. An estimate of the NO_x sensor capabilities necessary to meet the expected Euro 7 requirements is provided by PSA and is listed in Table 2.

Table 2. PSA estimates of Euro 7 NOx sensor requirements

System	Pollutant	Concentration range (ppm)	Concentration average (ppm)	Temperature (°C)	Response time (s)	Durability (km)
SCR	(NO)	10-2000	100	200-600	0.5	250000
SCR	(NO_2)	10-2000	100	200-600	0.5	250000
OBD	(NOx)	10-2000	20-30	200-1000	2	250000

The biggest change in the standards is that for NOx sensors in the SCR, it is expected that the sensors will need to selectively detect between NO and NO_2, both within a range of 10-2000ppm. As previously mentioned, the current lambda-probe NOx sensor is not selective, and cannot accurately detect below 10ppm. Additionally, they can only operate above 350°C, and therefore must be internally heated by a separate heating element. This

means that the new standards will likely require a completely new generation of NO and NO_2 sensors that can account for the shortcoming of the current commercial technology. It should be noted that neither the current standards nor the expected Euro 7 standards include emissions regulations for NH_3. However, this is expected to be incorporated in Euro 8 and therefore there is also a need for reliable NH_3 exhaust sensors. Even for Euro 7, the addition of NH_3 sensors could help control the NH_3 injection and improve the overall accuracy of the SCR system.

1.5 Sensor Performance Metrics

Several metrics are used to analyze the performance of solid-state sensors. In this section, each of the metrics is defined and explained in the context of automotive exhaust sensing. Each parameter is typically a function of several factors, including temperature and gas concentration.

1. **Absolute current change (Δ I):** This is the measured change in current between the steady state condition when no gas is applied and the steady state condition under a constant flow of a single concentration of gas. It is given by the equation

$$\Delta I = \left| I_{final} - I_0 \right| \tag{6}$$

   where I_0 is the initial current when no gas is applied (Figure 2).

2. **Sensitivity (S):** Sensitivity is defined as the relative change in signal at steady state after gas exposure and is defined as,

$$S = \frac{|\Delta I|}{I_0} \tag{7}$$

3. **Responsivity (R):** Responsivity is a metric that we have derived and is used to normalize different sensor types that may have different initial current values or sensing areas that affect the device performance. The equation for responsivity is,

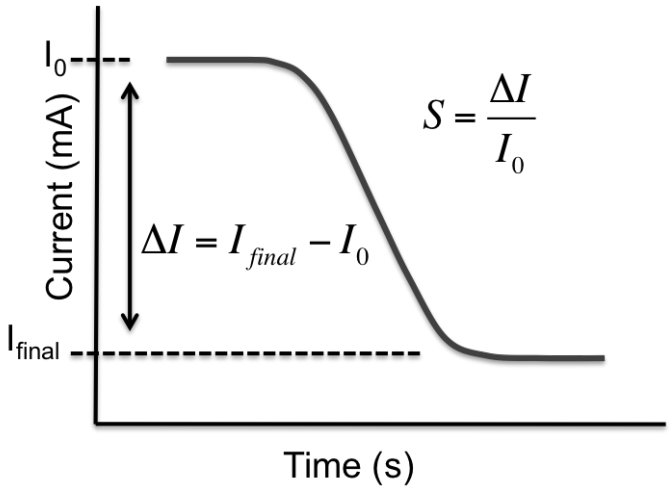

Figure 2. Definition of ΔI and sensitivity

$$R = \frac{\Delta J}{\Delta C} \tag{8}$$

where ΔJ is the current density change (ΔI divided by sensing area) and ΔC is the change in concentration of gas.

4. **Selectivity:** The selectivity is a measure of the cross-sensitivity to other molecules than the target gas. This is often given as a percentage indicating the relative amount of the signal change that can be caused by a non-target gas. A completely selective sensor is one that only detects the target gas and is insensitive to all other molecules.

5. **Response time** $_{10-90}$ **(**τ_r**):** This metric is used to characterize the transient response of a sensor after exposure to gas. The time is measured between 10 and 90% of the initial steady state value and the final steady state values under gas exposure (Figure 3a). This metric is typically used in situations where the sensor is allowed to reach steady state before the gas concentration is changed. For example, it may be used in diesel SCR applications when the vehicle is driving at a constant speed and using a relatively constant air/fuel mixture; it may also be used to measure gas changes inside the cockpit of the car, where the changes in concentration are more gradual.

6. **Recovery time$_{10-90}$ (τ_R):** This metric is used to characterize the transient response of the reset of a sensor after the test gas is turned off or decreased. The time is measured between 10 and 90% of the steady state value under gas exposure and the final steady state value.

7. **Dynamic response time ($\tau_{r,dynamic}$):** The dynamic response time gives the time between the exposure to gas and the first change in sensor signal (Figure 3b). This metric is used in cases where the gas concentration is changing rapidly, such as during vehicle acceleration/deceleration. In this case, instead of determining the gas concentration directly from the ΔI, the slope of the response is measured and used as an indication of the concentration change. In this case, $\tau_{r,dynamic}$ gives the limit of how fast a concentration change can be accurately measured.

8. **Reset temperature ($\mathbf{T}_{reset}$):** The reset temperature is the minimum temperature required for the sensor to break the chemical bonds on the sensing layer and return completely to its initial current value.

9. **Maximum temperature ($\mathbf{T}_{max}$):** The maximum temperature is the highest temperature at which the sensor can operate without irreversible damage to its material components.

10. **Repeatability/accuracy (% or ppm):** This metric is used to determine the accuracy of the sensor. The repeatability is the percent error between a statistically significant number of measurements using the same measurement conditions. The metric may also be given in units of ppm, indicating the possible deviation between the measured and actual concentration.

11. **Sensor lifetime (km or hr):** The number of km that a sensor can operate in the exhaust of a diesel automobile and still give readings with less than 10% error at 100ppm. For other applications, such as for liquid pollution detection, it may be

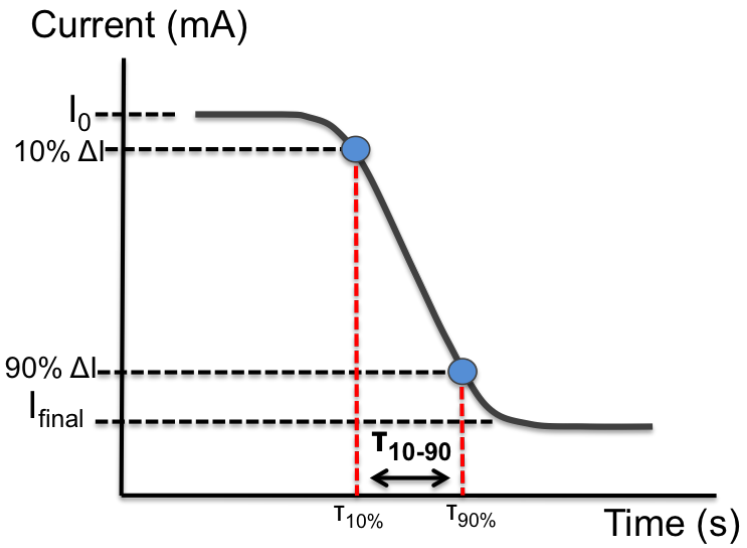

(a)

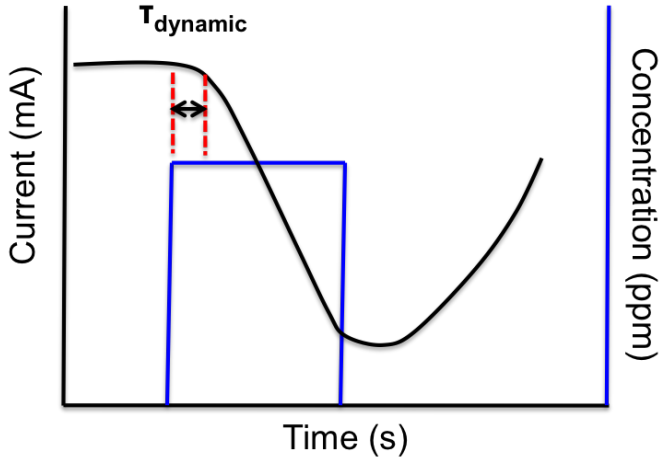

(b)

Figure 3. (a) Definition of 10-90% response time, τ_r (b) definition of dynamic response time, $\tau_{r,dynamic}$

measured in the number of hours of operation and the accuracy requirement may change depending on the needs of the application.

1.6 Current approaches for NOx and NH_3 sensors

This section outlines the most relevant solid-state exhaust gas sensors that are either commercially available or have been published in the literature. In this section, we focus on the detection of NO_x and NH_3 gases, but sensors for additional gases and molecules are

discussed when relevant. For this discussion, sensors are divided into three distinct types: (1) exhaust sensors currently used in industry, (2) conductance based sensors, and (3) work function-based sensors including Schottky diode, MOS, and HEMT sensors. In each case, the advantages and disadvantages of the sensor technologies are presented and compared. Finally, important considerations for our target applications and research objectives are discussed.

1.6.1 Commercial standards

Commercially available NO_x exhaust sensors are based on the lambda probe oxygen sensor technology developed by Robert Bosch GmbH in the 1960s [13] (Figure 4).

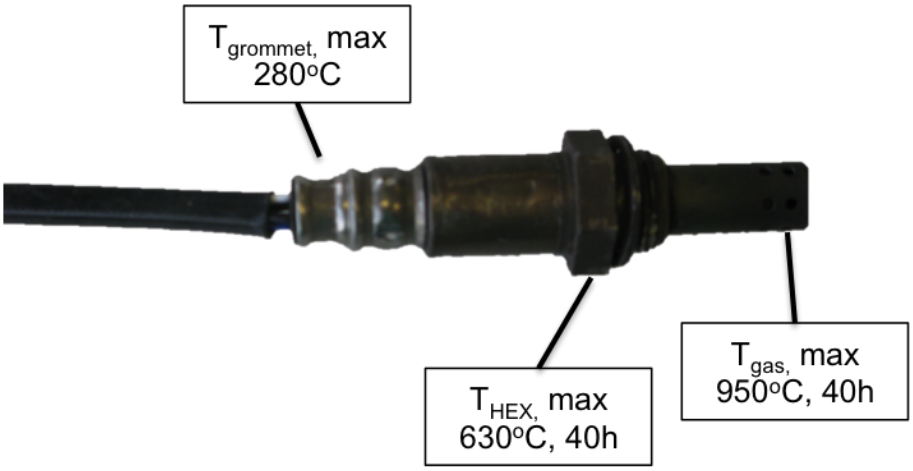

Figure 4. Bosch oxygen sensor (commercial standard) used in current diesel exhaust systems

The oxygen sensor, based on the concept of a Nernst potential cell, is comprised of a Zirconia membrane with a semi-permeable platinum electrode coated on both the inside and outside that act as the anode/cathode. Reference gas (ambient air) passes through a channel to the inside of the sensor in the Zirconia layer, while the outside is exposed to the exhaust gas. Above 350°C, oxygen ions are generated in the Zirconia layer due to partial dissociation and are free to move about within the Zirconia. This essentially

makes the Zirconium dioxide an electrolyte for oxygen atoms. The platinum electrodes enable the dissociation of oxygen atoms in both the exhaust and reference gases into oxygen ions. Then, differences in the concentration of oxygen on each side of the electrolyte (i.e. between the exhaust and reference gas) create a potential difference, or Nernst voltage, and is measured using a built-in voltmeter. This is then converted to the oxygen concentration in the exhaust according to the equation,

$$\Delta V_{Nernst} = \frac{-k_b T}{q} ln(\frac{C1}{C2}) \tag{9}$$

where k_b is the Boltzmann constant, T is temperature, q is the elementary charge, and C1 and C2 are the gas concentrations.

A higher concentration of oxygen will drive away oxygen ions from the reference gas causing a lower voltage. Typically, high air to fuel ratios (lean mixtures) will read voltages as low as 0.1V while low air to fuel ratios (rich mixtures) will read up to 0.9V. The dissection of a Bosch oxygen sensor, showing the internal components and sensing component, is shown in Figure 5. The zirconia sensing component and sensing mechanism is shown in Figure 6.

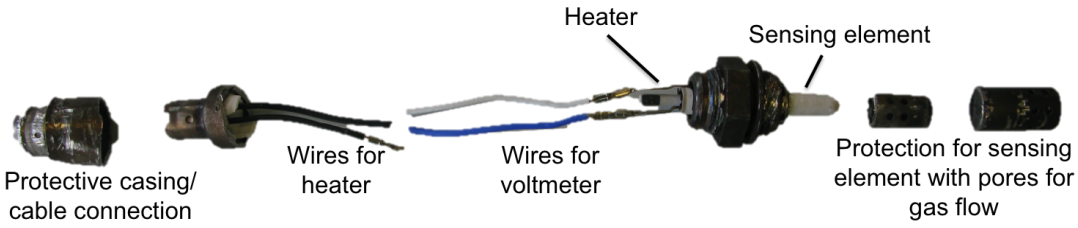

Figure 5. Dissection of the Bosch oxygen sensor showing internal components

Commercial NO_x sensors, also produced by Bosch, are based on the exact same principles as the oxygen sensor with one slight modification [14]. The sensor is divided into two chambers into which exhaust gas flows via a diffusion barrier on the outside of the sensor. The first chamber detects the oxygen concentration and then uses an electron pump to remove the oxygen atoms. The remaining exhaust gas is then pumped into the second

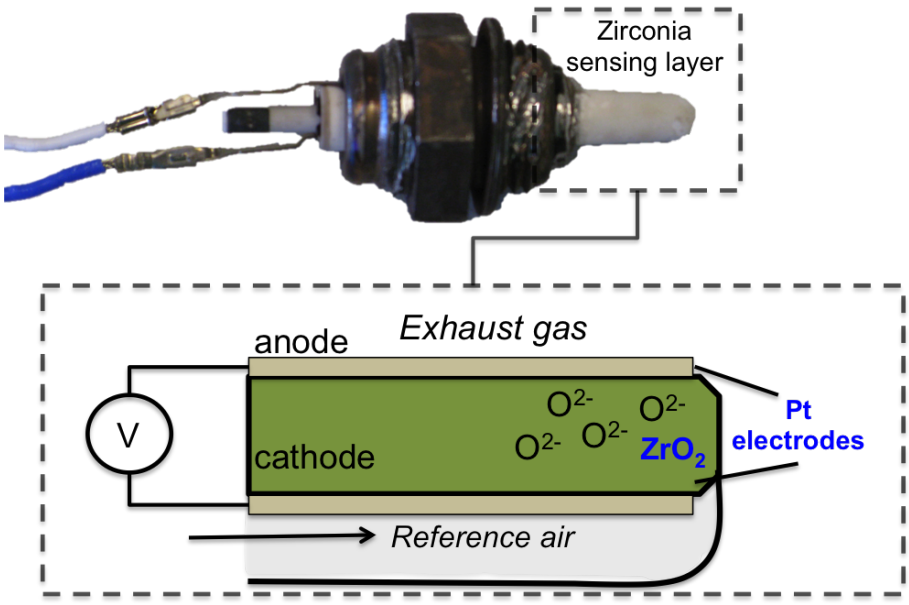

Figure 6. Sensing component and detection mechanism of Bosch oxygen sensor

chamber, where NOx dissociates into oxygen ions and the sensor behaves the same as an oxygen sensor. Since the concentration of oxygen is known, the sensor can calculate the NOx concentration based on the oxygen detected from the second chamber.

The main disadvantage of the lambda probe sensors is that it is not selective between NO and NO_2, and the detection limit is only around 10ppm which is already at the limit of the expected Euro 7 requirements. Additionally, it needs a reference gas and must be operated above 350°C using an external heater. The latter is an issue when operating the vehicle from a ”cold start.” The sensors are also nonlinear as a function of concentration, which makes the data processing more difficult for the OBD. Typically, the lifetime of these sensors is only 160000km, which is much shorter than the 250000km lifetime as desired by PSA. This is primarily due to the buildup of suit and other particles on the sensor, damage to the electrodes, and gradual drift in the voltage readings over time.

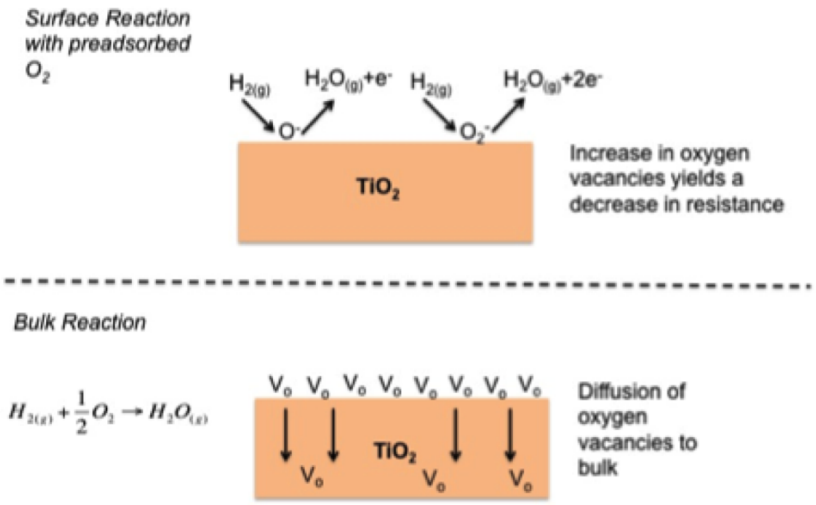

Figure 7. Semiconductor metal oxide sensor principle

1.6.2 Conductance-based sensors

Metal oxides such as SnO_2 and TiO_2 are used to detect gases by taking advantage of the numerous oxygen vacancies within the material, which effectively make them n-type semiconductors [16]. The principle of operation can be viewed as the combined effect of the surface and bulk interactions upon exposure to a gas mixture [17] (Figure 7).

The surface interaction is almost immediate upon exposure to gas, and involves reaction of the gas with preadsorbed oxgyen on the surface of the metal oxide. For oxidizing gases such as oxygen and NO_x, the oxygen ion fills an oxygen vacancy making the device less conductive; on the other hand, reducing gases such as H_2 or NH_3 remove an oxygen atom increasing the number of oxygen vacancies and thus the conductivity. This can also be viewed as a increase or reduction in the double Schottky barrier between grain boundaries upon adsorption of oxidizing or reducing gases, respectively. The bulk interaction occurs when the target gas reacts with other gases in the gas mixture, acting as an oxidizing or reducing agent and changing the equilibrium conditions in the gas phase which then alter the number of oxygen vacancies at the surface of the metal oxide.

This drives diffusion of oxygen vacancies either to or away from the bulk material, and is a much slower process than the surface interaction.

NO_x molecules (i.e. NO, NO_2) react with semiconductor metal oxide devices according to the following reactions [17]:

$$NO(gas) + O^- + e^- \rightarrow NO_2(gas) + O^- \tag{10}$$

$$NO_2(gas) + e^-(Zn) \rightarrow NO_2^- \tag{11}$$

The differences in the devices primarily come from the added materials, either as a dissociative electrode (Pt or Pd) or dopant. Table 3 lists the various device structures along with their performance specifications. [18–23]

Table 3. Performances of existing NO_x and NH_3 conduction-based sensors

Gas	Material	Concentrations Measured	Operating Temperatures	Reference
NH_3	ZnO or ZnO:Ni	10-100ppm	120-150°C	[18, 19]
NO	ZnO or ZnO:Ni	1000ppm	200°C	[19, 20]
	WO3/TiO_2:Pt	10-570ppm	300-500°C	[21]
NO_2	ZnO:Sn	1-1.5ppm	20-150°C	[19]
	ZnO:In	1ppm	300-350°C	[22]
	SNO_2:Zn	1.5ppm	100-500°C	[23]
	WO3/TiO_2:Pt	10-570ppm	500°C	[21]

The WO_2/TiO_2:Pt device also shows no interference with O_2 from 1- 99% and humidity up to 2.5%, which are relevant to conditions inside a car exhaust system.

Although these sensors can operate at high temperatures (up to 500°C), disadvantages include low detection limits and slow response times on the order of a few minutes. Perhaps the greatest disadvantage for our objectives is that they are not completely selective to different gases, although partial selectivity was shown in the doped materials.

Carbon nanotube based field-effect transistors (NTFET) also detect NO molecules via a change in device conductance [24]. The device is constructed of single-walled carbon nanotubes (SWNTs) with an Au/Ti source/drain and a SiO_2 back gate. A 10^{-3} mol/l PEI layer is coated on the NTFET surface, which changes the device from p-type to n-type. The

NO is oxidized to NO_2 using a CrO_3 converter, and the NO_2 withdraws electrons from the PEI layer thereby decreasing the conductance of the device. A detection limit of 5ppb and response time of 70 seconds have been achieved using this device, but recovery times are much slower at 30 minutes. The device is selective against NH_3, unlike other conductance based NO_x sensors. While O_2 does change the baseline by changing the conductivity of the SWNTs, it does not severely affect the detection limit for NO because the oxidation reaction between O_2 and NO is very slow. A disadvantage of NTFETs for exhaust sensing is that they are highly sensitive to humidity, which would introduce signal instability for this application. The optimal operating humidity for this device was found to be 15-30%. This range represents a balance between two effects: (1) increased humidity allows more efficient conversion between NO and NO_2; and (2) increased humidity decreases the signal to noise ratio of the device. The device also suffers from a strong cross-sensitivity to CO_2 in concentrations as low as 1% of the gas mixture. A bare NTFET device, however, does not show CO_2 cross-sensitivity, but has a higher detection limit of 200ppb and a slower response time of 250 seconds.

1.6.3 Work function-based sensors

The first work function-based sensor was a metal-semiconductor (MS) sensor using silicon by Lundstrom in 1975 [25, 26]. This device showed a voltage change upon exposure to hydrogen gas at a constant current. The mechanism for the voltage change was attributed to a dissociative reaction with the Pt Schottky contact; after diffusion through the Pt layer the hydrogen ions form a chemisorption with the SiO_2 layer, forming a dipole moment at the interface which changes the interface potential. This potential change leads to a change in work function and Schottky barrier, changing the current of the device. Lundstrom later showed that the same effect can be seen with NH_3 gas [27, 28], and that the Pt thickness and morphology (by various processing techniques) affects the sensitivity and selectivity of the device [29]. For example, evaporation and sputtering at higher pressures were linked to higher sensitivities than lower pressure sputtering.

After the groundwork of work function-based sensors was paved by Lundstrom and his group, the idea was expanded to include metal-semiconductor Schottky diode devices, MOSFET, and high electron mobility (HEMT) sensors by many different groups using a variety of semiconductor materials. By far, the most common gas detected using these devices is hydrogen and has been demonstrated by many groups [30, 64]. For Schottky diode devices, detection of hydrogen gas has been accomplished most commonly using Si, SiC, or GaN. Typically, Pt or Pd is used as the Schottky contact due to its catalytic nature. For HEMT devices, the gate acts as a Schottky barrier and thus the concept of the MOS and Schottky diode sensor can be readily integrated into the transistor device. While some AlGaAs/GaAs HEMTs have been used, there has been a shift to AlGaN/GaN as materials for HEMT sensing due to their high carrier mobilities.

While these sensors have readily been used to detect hydrogen gas, less work has been done on the detection of NH_3, and even less on NO_x. After Lundstrom and Spetz demonstrated NH_3 sensitivity using Si [28, 31], Lechuga accomplished a similar result using a porous Pt/GaAs Schottky diode [32]. Instead of measuring a voltage change, a capacitance change was measured. Concentrations between 8 and 58ppm were reported, with a relative sensitivity between 0.2 and 0.8%.

Schottky diode sensors based on 4H- and 6H-SiC with a thin Pt contact were shown to have a rather large value of sensitivity (S)=19.35% to 200ppm NO_2 at 300°C [33], but with a very low value of responsivity (R)=1.91 $\mu Acm^{-2}ppm^{-1}$ and slow response time, of the order of several minutes. A separate study [34] using n-type GaN Schottky diode sensors with a 75 nm-thick Pt contact showed an improved response to NO_2 at 300°C compared to SiC-based sensors, but a quantitative comparison of the responsivity and/or sensitivity was not possible using the reported metrics. A small response in the opposite direction (+50 mV) was also shown for NO gas. This indicates that the chemical mechanism for NO and NO_2 detection is not identical, but it the exact mechanisms have not yet been identified. A similar device was replicated by Tilak in 2006 using a GaN Schottky diode

with a 40nm Pt contact [37]. This device showed a 150mV shift under NO with an eventual memory effect after several pulses. Pt/AlGaN/GaN HEMT structures was shown to exhibit a decreased S=10% to NO_2 due to a higher initial current, but a significantly higher R=1.14 $mAcm^{-2}ppm^{-1}$ at 400°C [38]. The same device showed negligible response to NO gas. This tradeoff between the ΔI (and thus the responsivity) and sensitivity is explained by the fact that the ΔI for Schottky diodes is given by the expression $\Delta I=I_0 e^{\frac{\Delta\phi_B}{kT}} - 1$, which is derived from the thermionic emission transport model. Therefore, a high initial current results in high responsivity whereas the sensitivity is increased with a large increase in $\Delta\phi_B$ caused by a high concentration of interface traps, which results in a lowering of the initial current. The importance of finding the best balance between ΔI and I_0 is exemplified by the work of Quang et al. [39] who reached large ΔI for NO_2 while maintaining relatively large I_0 in SNO_2 nanowires-based Schottky junction (SJ) gas sensor, and thus coming out with outstanding values of both sensitivity and responsivity. Furthermore, even if limited to very low gas concentration (tens of ppb) and rather low operating temperature (150°C), the response time of the device was shown to be relatively fast. HEMT sensors for NH_3 detection have also been developed, showing sensitivity to concentrations as low as 35ppm, with a memory effect below 200°C; at a temperature of 200°C, the recovery time is on the order of a few seconds [41]. It is important to note that complete selectivity between NO_2 and NH_3 has not yet been demonstrated in these types of devices. A summary of device performances of the reported work function-based sensors is presented in table 4.

It is clear from the literature review that work function devices provide a viable option for high sensitivity gas detection. However, the application of these devices for NO, NO_2, and NH_3 gases has not yet been fully explored. Furthermore, fully selective, high sensitivity devices operating over a wide temperature range have not yet been realized. Therefore, providing viable sensing options to obtain these features is the goal of this research and dissertation.

Table 4. Summary of NO_2, NO, and NH_3 sensor performances, including sensitivity (S), responsivity (R), response time (τ_r) and recovery time (τ_R).

Gas	Device	Catalyzer	I_0 (mA)	ΔI (μA)	S (%)	R ($\frac{mA}{cm^2*ppm}$)	C ppm	T (C)	τ_r/τ_R (s)	Ref.
NO_2	SiC Schottky Diode	20-40nm Pt	0.02	3.8	25	0.002	200	300	90/120	[33]
	SNO_2 Schottky Diode	-	0.42	243	58.3	648	0.1	150	43/37	[39]
	GaN Schottky Diode	Pd/ZnO	4.5	860	19.1	2.74	10-100	250	60/120	[42]
	AlGaN/GaN HEMT	Pt	5	500	10	1.43	1000	400	n/a	[34]
NO	SiC Schottky Diode	20-40nm Pt	0.108	10	9.26	0.03	40	400	188/99	[33]
	GaN Schottky Diode	Pd/ZnO	4.5	160	3.56	0.51	10-100	250	60/120	[42]
	AlGaN/GaN HEMT	Pt	5	negligible	negligible	negligible	1000	400	n/a	[34]
NH_3	AlGaN/GaN Schottky	20nm Pt	nA range	nA range	3000	1.4e-8	35	70	600/900	[41]
	AlGaN/GaN Schottky	10nm Pt	21.5	640	2.98	18286	35	30	n/a	[43]

1.7 Our research approach

1.7.1 Research goals

The research presented in this dissertation is part of a larger Open Lab project aimed at developing next generation NO, NO_2, and NH_3 sensors for diesel SCR systems. The main goals of this thesis are to study and explore various technology options in order to develop sensors that have the following attributes:

1. Detection of total NO_x and NH_3 in the 0-1000 ppm range
2. Operation over a wide range of temperatures (25-600°C) in an unstable environment
3. Selectivity between different gases, especially NO and NO_2

In addition to these primary goals, we also explore options for decreasing the response time of the sensors and increasing their overall lifetime. One of the other goals of this research is to gain a better understanding of the chemistry of the sensing mechanisms in work-function based sensors and to apply this information to design more sensitive and selective sensors.

While we focus heavily on the diesel SCR application, we also explore methods of adapting our technology to other applications. Such applications include the detection of NO, NO_2, and NH_3 in the cockpit of automotives or airplanes, NH_3 sensing for quality control in industrial settings, and detection of nitrates and phosphates in liquid environments.

1.7.2 Strategy and methodology

In this work we focus on a microtechnology approach using high bandgap, III-V nitride-based semiconductor materials such as GaN, BGaN, and AlGaN. These materials have gained interest for over the last several years due to their many attractive properties. For example, the high, direct bandgap of GaN (3.4eV) makes it suitable for optoelectronic devices such as LEDs, lasers, solar cells, and photodiodes [44]. In 2014, the Nobel Prize in physics was awarded for the invention of the energy-efficient blue LED using GaN [45]. These materials also have high breakdown voltages and high electron mobilities, making them suitable for high-power and high frequency devices such as transistors. Ternary alloys of III-V nitride materials allow tuning of the bandgap which is useful in designing devices for specific applications. These materials are also good candidates for sensing applications in harsh environments due to their high mechanical, chemical, and thermal stability (the melting temperature of GaN is 2500°C).

We propose two main solutions for meeting the research objectives, both of which utilize microtechnology approaches: (1) Schottky diode and MSM sensors using GaN and BGaN materials; and (2) AlGaN/GaN HEMT sensors. These two options are not mutually exclusive, but rather can be explored in parallel (Figure 8). For example, the Schottky diode sensors are easier to fabricate and can be used as method of studying the sensing mechanisms, sensing properties of new materials (e.g. BGaN), and developing strategies for gas selectivity. Since the HEMT gate is essentially a Schottky diode, Schottky diode sensors can either be used as a stand-alone sensor or as a building block to develop improved HEMT sensor devices. Since HEMT sensors offer some additional advantages over diodes (e.g. tunable sensitivity, lower detection limits), we plan to develop these sensors in parallel and optimize them for exhaust gas sensing.

The general process flow used to accomplish the research objectives is shown in Figure 9. This process is used for both Schottky and HEMT sensors in parallel. In the first step, a comprehensive Matlab program is developed to simulate both HEMT and Schottky

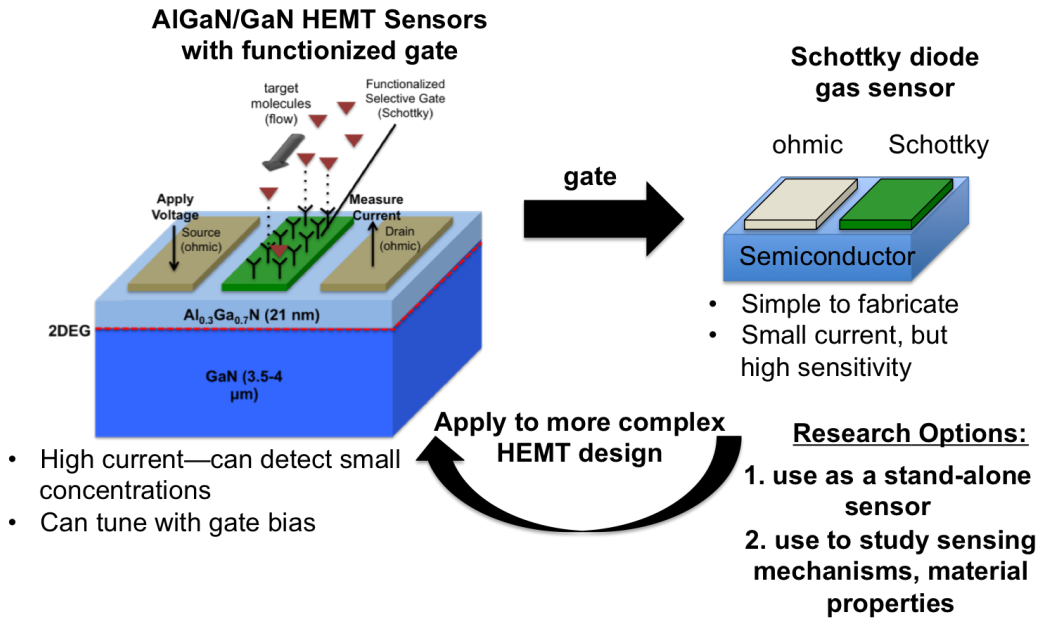

Figure 8. Overview of our research strategy

device physics. The analytical model is expanded to include both semiconductor physics and chemical reaction kinetics in order to simulate sensor behavior for a variety of factors (semiconductor material properties, gas type, temperature, etc). Commercial software (Silvaco) is also used in conjunction with the in-house developed program to design the sensors. The simulations are used to design both the materials growth plan and the metal contacts, including the sensing layer. Masks for photolithography are designed using Layout Editor and purchased from Selba in Switzerland. The semiconductor materials growth is conducted at Georgia Tech Lorraine using an MOCVD T-shaped reactor. The materials are characterized at Georgia Tech Lorraine using AFM, SEM, XRD, and Hall Effect measurement systems in order to determine the crystalline quality, composition, and electrical properties of the layers. The sensors are fabricated using photolithography at either the University of Lorraine in Nancy for Schottky devices or at IEMN in Lille for HEMT devices. The sensors are then tested at a laboratory built at the Laboratoire Materiaux Optiques, Photonique et Systemes (LMOPS) in Metz. The laboratory is designed specifically

for microsensor testing and includes setups for both gas and liquid pollution sensors. After device testing, the process flow takes two simultaneous paths. On one side, the results from device testing give insight into how the sensors can be optimized, and these optimizations are used in new generations of sensors. At the same time, the processed sensors can packaged and used for testing in real-life environments (e.g. in a car exhaust). The packaging and real-life testing stages are outside of the scope of this thesis and represent the future work of the overall project. The focus of this this thesis is on the conception, design, fabrication, and testing of the first generations of HEMT and Schottky diode sensors for automotive exhaust gases (NO, NO_2, and NH_3). Analysis of these results is used in theee ways: (1) to study the sensing characteristics to each test gas, (2) to validate and improve the analytical modeling program and use this to extract valuable information about the device physics and chemical mechanisms, and (3) to optimize and design future iterations of sensors with improved device performance, especially regarding sensitivity and selectivity.

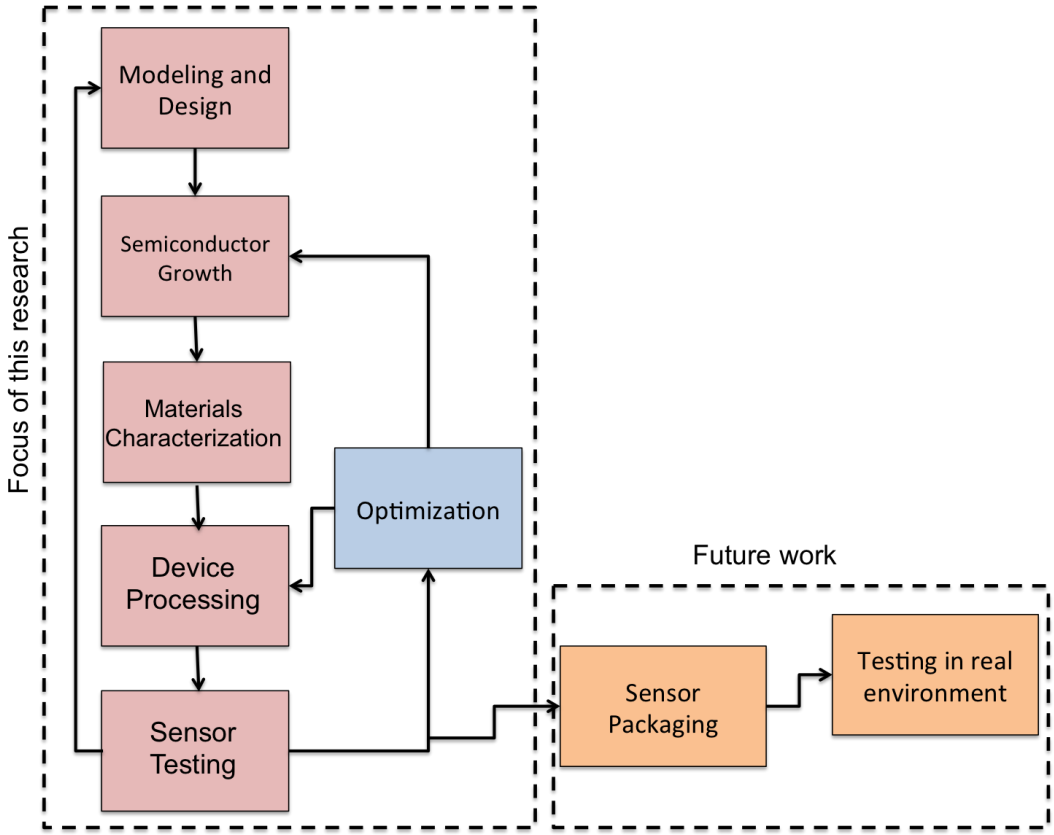

Figure 9. Process flow of the research strategy for this project

CHAPTER 2

SCHOTTKY DIODE-BASED SENSORS USING GAN AND BGAN MATERIALS

2.1 BGaN: A Novel Material for Gas Sensing Applications

boron nitride-based alloys such as BGaN offer many potential advantages for gas sensing, but have not yet been extensively explored for these applications. Specifically, high thermal and mechanical resistance and the ability to withstand harsh chemicals and gas exposure make this material promising for the detection of exhaust gases in unstable environments [46]. Studies involving BGaN growth using MOCVD and the properties of BGaN materials have already been carried out at Georgia Tech Lorraine. One of the challenges involved with MOCVD growth of BGaN is the lattice mismatch between BN and GaN, which causes strain relaxation of the layers for boron incorporations above 2% [47]. While it is expected that the theoretical bandgap of BGaN should increase linearly between the bandgaps of GaN and BN, it turns out that there is bowing of the bandgap with a bowing parameter of C=8.7-9.7eV [48]. The maximum boron incorporation is a function of the layer thickness, with thicker layers limiting the amount of boron. Typically, 300-400nm monolayers are the maximum thickness for successful incorporation of 0.7% boron. One way to compensate for this is to use several GaN/BGaN interlayers of 10-20nm each, known as a superlattice (SL) structure. This allows for thicker overall BGaN layers compared to the monolayer structure for an equivalent boron incorporation. BGaN/GaN superlattice layers of 400nm have been grown with boron incorporations of 3.6% for each BGaN layer. It has been also been shown that the BGaN growth is columnar, leading to zinc-blende cubic nanoclusters of BGaN material on the surface that contain up to 20% boron [46]. Deep level transient spectroscopy (DLTS) measurements have been performed in a separate thesis study that show that the trap levels in BGaN are more numerous and have deeper energies with increasing boron incorporation. The latter two points are features of BGaN

that can be exploited for improved selectivity and sensitivity of gas detection, as will be discussed in the following sections. It has already been shown that the properties of BGaN are advantageous for other applications, such as resistive back-barriers for AlGaN/GaN HEMT structures [49, 50] and photocurrent devices with increased responsivity [51, 52].

2.2 Schottky diode sensor device physics and reaction chemistry at the metal-semiconductor interface

The gas detection mechanisms of metal-semiconductor devices involve a multistep process of adsorption, dissociation, and diffusion. Several different mechanisms exist depending on the target gas and its interaction with the catalytic sensing area [34]. In this work, we use Pt as the sensing contact. Although the exact mechanisms for each gas are not completely understood, a summary of the mechanisms that have been proposed in the literature is depicted in Figure 10.

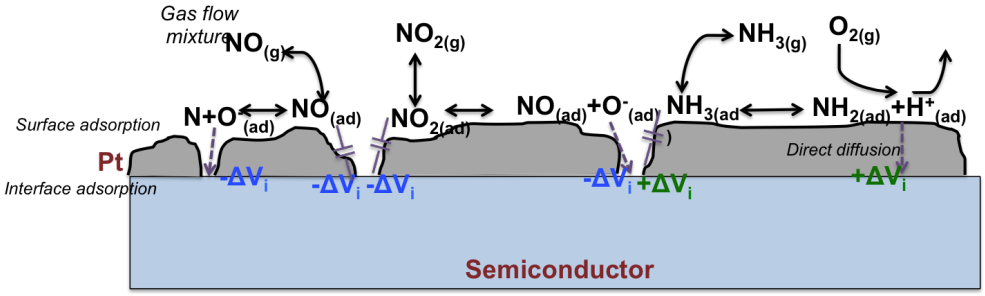

Figure 10. Reaction mechanisms of various exhaust gases with Pt gate contact

For each gas, the first step of gas detection is physisorption on the Pt surface according to a sticking coefficient given by,

$$S(\theta) = S_0(1 - \theta) \tag{12}$$

For detection of hydrogen gas, it is generally accepted that the hydrogen dissociates into two positive hydrogen ions on the Pt catalyst. These gas ions then rapidly diffuse through the continuous Pt and chemisorb to the AlGaN surface at available adsorption sites, forming a dipole layer between the AlGaN and Pt layers [35]. Viewed purely from an electrostatic

perspective, a charged ion can be treated as additional charge at this interface. Without gas, the charges present at the interface are comprised of a positive depletion charge on the semiconductor side and a negative image charge on the metal. The additional positive charge at the interface due to the positive hydrogen ion must be compensated by a more negative depletion region, which is accounted for as an decrease in the Schottky barrier height. This can also be viewed in terms of the dipole moment between the chemisorbed gas ion and the interface trap.

In this work, we extend this physical description by interpreting the adsorption sites as electrically charged interface states, most commonly resulting from Ga or N vacancies in the crystal lattice, threading dislocations, or dangling bonds on the surface. To electrostatically balance the charge changes at the interface due to the gas ions, the work function and Schottky barrier height of the Pt contact is changed, which changes the current passing through the semiconductor material. This interface trap interpretation allows us to more precisely model the gas interactions with the physical parameters of the semiconductor material. It also allows us to better understand the chemical nature of the reactions between the gas and semiconductor that may be utilized to improve the sensitivity and selectivity of our sensor devices.

The adsorption of the gas is modeled using a Tempkin isotherm, which gives a relation of the concentration of gas available for adsorption to the equilibrium state coverage of molecules on the Pt contact [53]. The Schottky barrier height change is expressed as [34]

$$\triangle\phi_B = \frac{\rho N_i \theta}{\varepsilon\varepsilon_0} \tag{13}$$

where N_i is the concentration of available interface states, ρ is the dipole moment associated with the chemisorption between the gas ion and interface traps, ε is the permittivity of the dipole layer. θ is the fraction of interface traps bonded by ionized gas molecules and is given by [36]

$$\theta = \frac{K\sqrt{P_{gas}}}{1 + K\sqrt{P_{gas}}} \tag{14}$$

where K is the equilibrium rate constant that balances the rates of adsorption and desorption, and P_{gas} is the partial pressure of gas. K is a function of both temperature and gas concentration, and can be obtained from thermodynamic experiments. The rates of adsorption and desorption, respectively, are given by,

$$k_a = r_a e^{\frac{-\Delta H_a}{kT}} \tag{15}$$

$$k_d = r_d e^{\frac{-\Delta H_d}{kT}} \tag{16}$$

where r_a and r_d are the reaction rates of adsorption and desorption, respectively, and ΔH_a and ΔH_d are the enthalpies of adsorption and desorption, respectively.

For our model, we assume that each of the gas/interface state interactions behaves identically for a particular gas, meaning that we are considering an overall, average effect from these interface states for each gas. Other assumptions include that the probability of dissociation is 1, which is realistic based on experimental observations [34], that all of the reactions occur either on the surface of the Pt gate or at the Pt/AlGaN interface (i.e. there are no adsorption sites within the continuous Pt layer) and that the ions diffuse readily and rapidly through the thin Pt layer via grain boundaries or pores. We also assume that the sticking coefficient is 1.

In general, oxidizing gases such as NO_2 dissociate on the Pt surface according to the reaction [54]

$$NO_2 + Pt \rightarrow NO + O_2^- \tag{17}$$

Unlike hydrogen, the oxygen ions are too large to diffuse through the continuous Pt layer and therefore must diffuse through grain boundaries or pores. The negative oxygen

ions create a negative potential at the Pt/AlGaN interface which is compensated by an increase in the Schottky barrier height.

The reducing gas NH_3 undergoes a similar dissociation reaction on the Pt surface according to the reaction [55]

$$NH_3 + Pt \rightarrow NH_2 + H^+ \tag{18}$$

The dissociation of NH_3 has also been reported to occur only at triple points, where the Pt, gas, and semiconductor surface are all in contact at once [29]. This requires the presence of larger pores for the entire NH_3 molecule to reach the AlGaN surface. It has also been reported that NO sometimes behaves as a reducing gas, and instead of dissociating it interacts directly with traps on the interface (also requiring pores) or capacitively from the Pt surface [34].

For NO_2, NH_3, and NO gases, the adsorption isotherm must be altered slightly from the one used for hydrogen detection. This is because for these gases, the dissociation does not necessarily produce two separate ions that diffuse through the Pt layer. When only one ion diffuses, the coverage term is modeled as,

$$\theta = \frac{KP_{gas}}{1 + KP_{gas}} \tag{19}$$

NH_3 can dissociate into either one or two positive hydrogen ions, and therefore may be described either coverage equation. We have so far looked at the mechanisms of individual gases and made the assumption that each gas binds to one or more interface state types without interference. When modeling a mixture of the three exhaust gases, which is the realistic environment inside and automotive exhaust system, this assumption no longer holds true since different gases can likely bind to the same types of interface states. This type of behavior is described using a competitive adsorption model, where the coverage term for each gas is modeled as,

$$\begin{cases} \theta_{NO_2} = \frac{KP_{NO_2}}{1+KP_{NO_2}+KP_{NO}+KPNH_3} \\ \theta_{NO} = \frac{KP_{NO}}{1+KP_{NO_2}+KP_{NO}+KPNH_3} \\ \theta_{NH_3} = \frac{KP_{NO_2}}{1+KP_{NO_2}+KP_{NO}+KPNH_3} \end{cases} \tag{20}$$

In a gas mixture, it is also possible for the gases to react with each other before adsorption, creating additional reaction intermediates that can participate in the adsorption. In the scope of this thesis, we do not consider the competitive adsorption model but rather focus on studying and understanding the gas mechanisms for each individual gas. In later sections, we do approach the issue of gas mixtures experimentally, but updating the adsorption model for multiple gas species is included in the future work for this project.

2.3 Device design and modeling of GaN and BGaN Schottky-based sensors

2.3.1 Effects of interface traps on gas sensing

Using our interface trap interpretation, the performance of Schottky sensor devices can be linked directly to a change in the concentration of interface traps available for gas adsorption according to equation 13. Figures 11, 12, and 13 show the effects of interface traps on both the current-voltage characteristics and the energy band structure of the metal-semiconductor diode without applied gas.

In an ideal diode (Figure 11), there are no interface traps and the primary transport mechanism in both forward and reverse biases is thermionic emission (TEM) [56]. This current transport mechanism dominates when the carriers have energy higher than the Schottky barrier height. In the forward bias, the conduction band of the semiconductor is raised relative to the Fermi level of the metal and a large number of carriers can cross the potential barrier, increasing the current of the device. The current for TEM transport is given by the expression,

$$I_{TEM} = I_{sat} e^{\frac{V}{kT}-1} \tag{21}$$

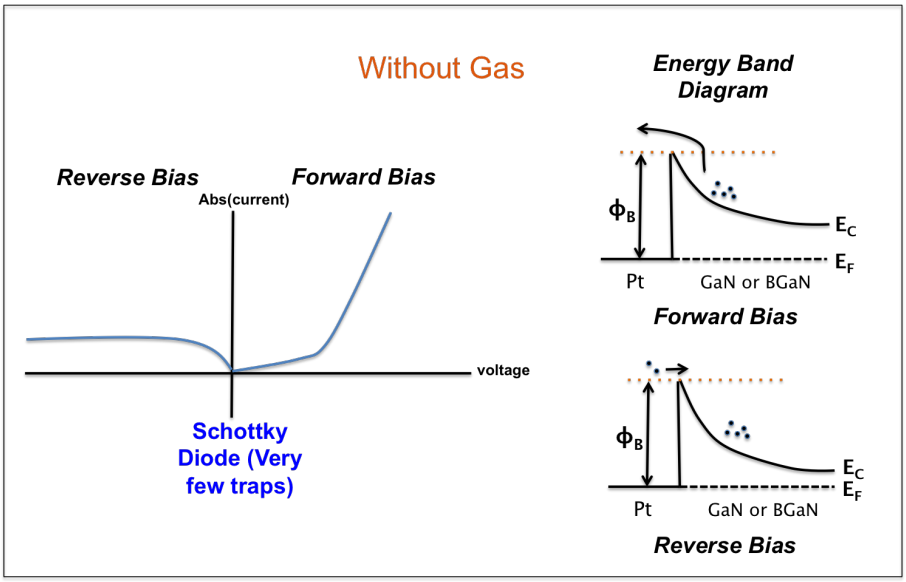

Figure 11. Current-voltage and energy band effects in Schottky diodes as a function of very low interface traps (ideal diode)

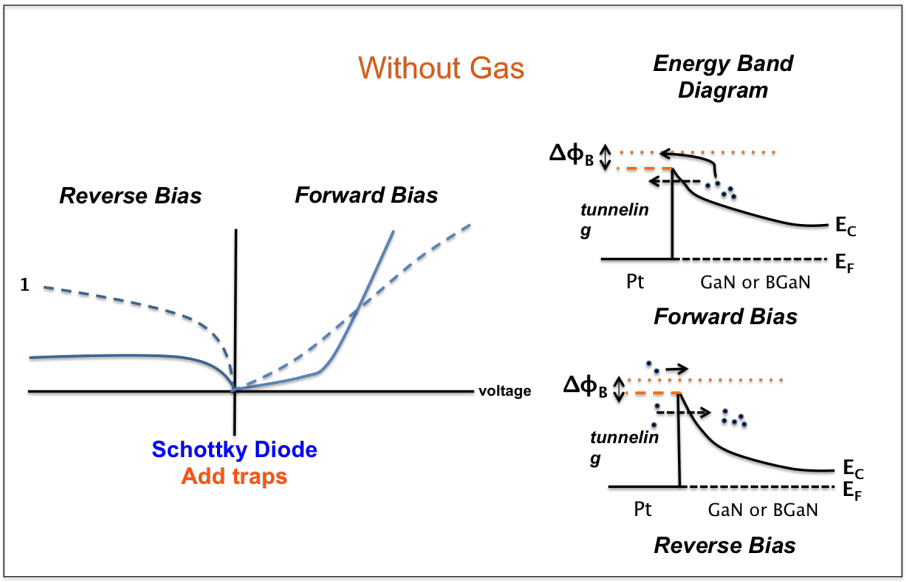

Figure 12. Current-voltage and energy band effects in Schottky diodes as a function of interface traps

where V is the applied bias, k is the Boltzmann constant, and T is the temperature in Kelvin. I_{sat} is the reverse saturation bias given by,

$$I_{sat} = A^* A T^2 e^{\frac{-\phi_B}{kT}} \tag{22}$$

where A^* is the Richardson constant given by [57],

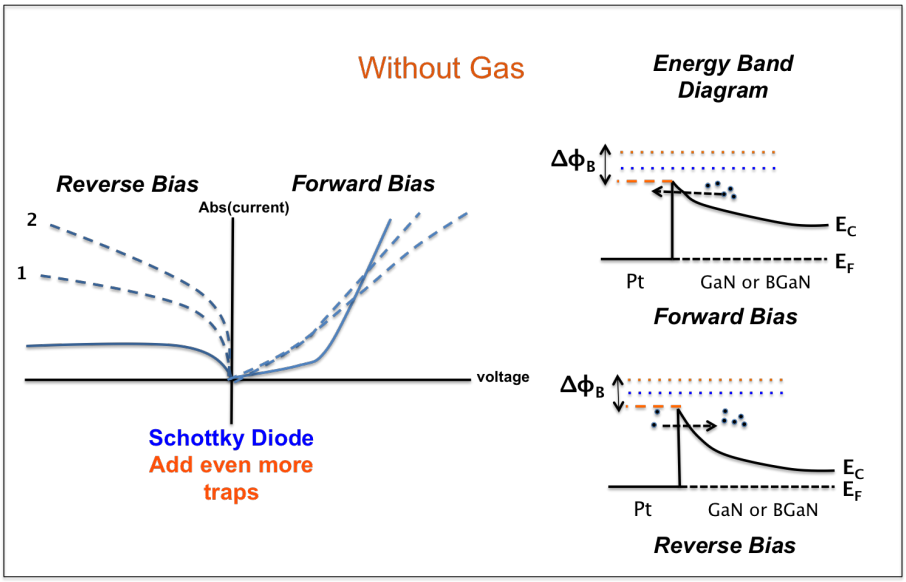

Figure 13. Current-voltage and energy band effects in Schottky diodes as a function of high interface trap concentration

$$A^* = \frac{4\pi q m^* k^2}{h^3} \tag{23}$$

where m^* is the effective mass of electrons in the semiconductor material and h is Planck's constant. In GaN, m^* is assumed to be $0.2m_0$ and A^* is assumed to be $26.4\text{x}10^4 \text{A/m}^2K^2$ [58].

In the reverse bias, the exponential dependence of the current on voltage means that the numerator approaches negative infinity, causing the term to reduce to 1. This leaves only the reverse saturation current after voltages much higher than the thermal voltage, kT/q. Physically, this can be described as electrons crossing the barrier from the metal contact to the semiconductor over the Schottky barrier. In the TEM transport model, this is only possible if the thermal energy is sufficient to increase the carrier energy above the barrier. Since this is not probable for most Schottky barriers with energy significantly higher than the metal work function (e.g. Pt on GaN), the reverse bias current is significantly limited compared to the forward bias current.

If interface traps are included in the model (Figure 12), a quantum effect known as

trap-assisted tunneling acts as a second transport mechanism that contributes to the overall device current. In both forward and reverse bias, some electrons can tunnel through the barrier with a certain probability that is related to the number of available electrons, the velocity of the carriers (proportional to the electric field and applied bias), and the height of the energy barrier. If the potential barrier is assumed to be triangular shaped, the trap-assisted tunneling current is given by the expression [59],

$$I_{tat} = qv_R n\theta_{tunnel} \tag{24}$$

where v_R is the voltage-dependent Richardson velocity given by,

$$v_R = (\frac{kT}{2\pi m})^{0.5} \tag{25}$$

and θ_{tunnel} is the tunneling probability given by,

$$\theta_{tunnel} = exp(\frac{-4}{3}\frac{\sqrt{2qm*}}{\hbar}\frac{\phi_B^{\frac{3}{2}}}{\varepsilon}) \tag{26}$$

The tunneling current can also be written as [59],

$$I_{tat} = \frac{\pi^2 q^2 A m^* V_t M^2 N_i}{h^3 \phi_B} \times exp(\frac{-8\pi(2m^*)^{1/2}(\phi_B)^{3/2}}{31hE(V)}) \tag{27}$$

where V_t is the difference between the built-in voltage and the applied bias, and M is a matrix element used to describe the trap energies (assumed to be 10e-23 eV^2cm^3.

The interface traps act as intermediate energy steps for carriers and effectively lower the Schottky barrier. The higher energy electrons have a thinner potential barrier to pass since they are closer to the top of the triangle, and so the tunneling probability is increased. This increases the initial current of the device. In the current-voltage characteristic, this effect can be seen as an increased slope in the current for reverse biases; in forward bias, traps result in a lower threshold voltage and higher current at low voltages followed by a decreased current at higher voltages where TEM is dominant. These effects are more prominent with

an increase in interface traps (Figure 13). The reason for a decreased current at high forward biases is due to the fact that an increase in interface traps is accompanied by an increase in bulk traps, which trap electrons in the semiconductor layer and reduce the overall current.

The contribution of both current transport mechanisms in the ideal diode case for Pt on GaN is modeled in Matlab using equations 21-27 (Figure 14).

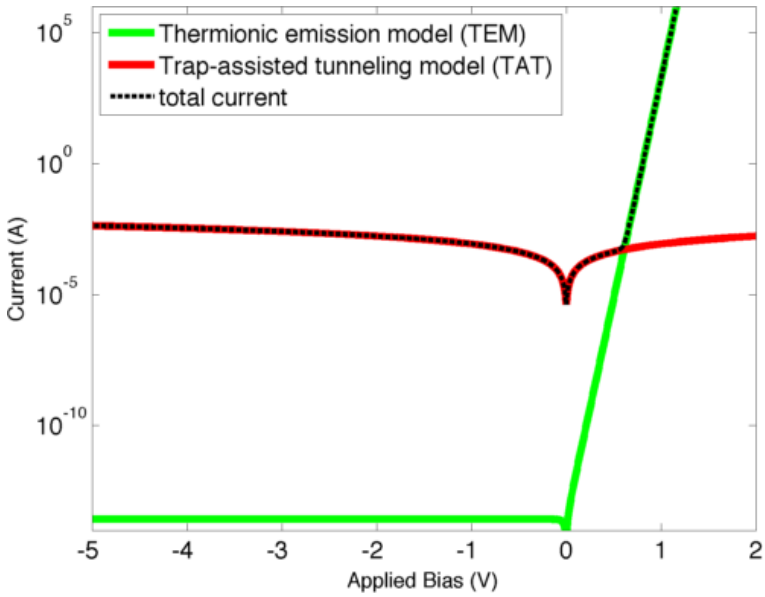

Figure 14. Schottky diode model for different transport mechanisms

Note that in this model, only TAT and TEM mechanisms are considered. Other transport mechanisms, such as diffusion and recombination-generation currents, account for currents that are typically several orders of magnitude lower and can therefore be ignored for this analysis [59]. It is clear from the transport curves that the dominant mechanism in reverse bias and forward biases greater than $3kt/q$ is TAT, while TEM is the dominant mechanism in forward biases greater than $3kt/q$.

When a gas is applied to the metal-semiconductor diode, the work function of the metal is changed as described in section 2 of this chapter. For the oxidizing gas NO_2, the ionized oxygen molecule is trapped at the interface via a chemisorption between the interface traps and the gas ion. This results in an increase in the barrier height and decrease in device current (Figures 15 and 16). Note that if no traps were present at the interface, as in an

ideal diode, there would be no sensitivity to the gas.

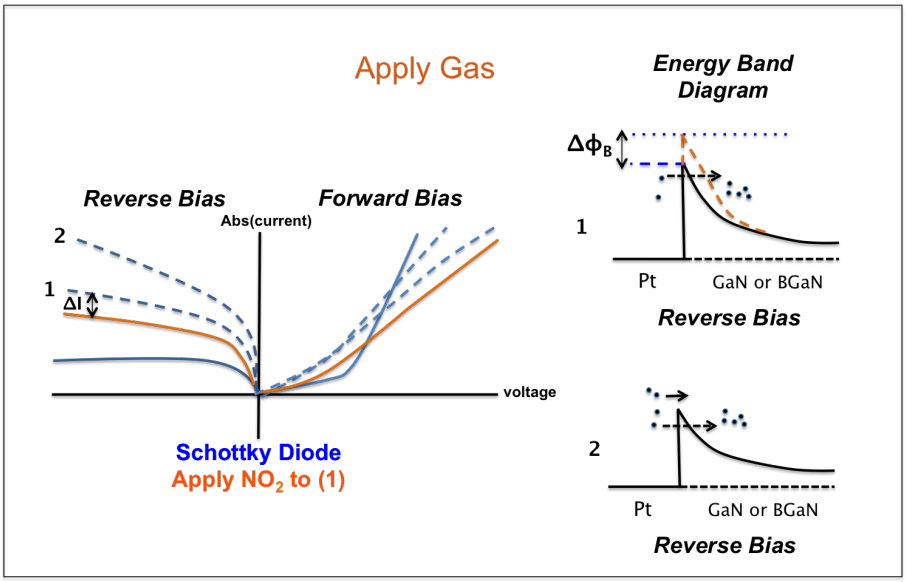

Figure 15. Current-voltage and energy band effects in Schottky diodes under NO_2 gas flow (low initial current)

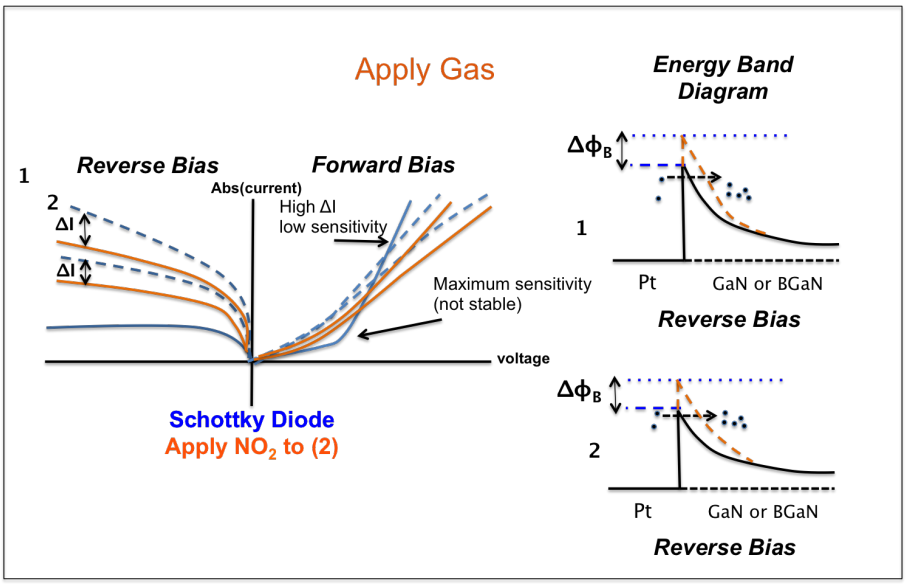

Figure 16. Current-voltage and energy band effects in Schottky diodes under NO_2 gas flow (high initial current)

In the forward bias, where TEM is the dominant mechanism, we see from equation 22 that the current is a function of ϕ_B, and therefore the current changes upon gas exposure due to a change in ϕ_B. This ΔI and sensitivity in the forward bias are then derived as,

$$\Delta I_{forward} = I_0(e^{\frac{-\Delta\phi_B}{kT}} - 1) \tag{28}$$

$$S_{forward} = e^{\frac{-\Delta\phi_B}{kT}} - 1 \tag{29}$$

where I_0 is the initial current from TEM transport when no gas is present (or in our experimental conditions, when the device is only exposed to a constant flow of inert N_2). The initial current is a function of the device area and temperature, and applied bias; these parameters will therefore affect the ΔI. The sensitivity, on the other hand, is divided by the initial current and is therefore only dependent on the change in barrier potential from exposure to gas. In forward biases much greater than kT/q, the ΔI is increased due to the applied bias, while the limiting factor in sensitivity is the exponential of ϕ_B to the first power. This is consistent with our physical interpretation; if a large proportion of carriers already have sufficient energy to pass over the potential barrier, a small increase or decrease in the barrier height will not have a significant effect on the relative current change. For small forward biases and reverse biases, on the other hand, the dominant transport mechanism is trap-assisted tunneling, where the sensitivity is a function of the exponential of $\phi_B^{3/2}$. From equations 24-27, we derive the equation for ΔI and sensitivity in the reverse bias as,

$$\Delta I_{reverse} = I_0 \left\{ exp\left(\frac{-4}{3} \frac{\sqrt{2qm^*}}{\hbar} \frac{\left(\phi_{B,gas}^{3/2} - \phi_{B,initial}^{3/2}\right)}{\varepsilon} \right) - 1 \right\} \tag{30}$$

$$S_{reverse} = exp\left(\frac{-4}{3} \frac{\sqrt{2qm^*}}{\hbar} \frac{\left(\phi_{B,gas}^{3/2} - \phi_{B,initial}^{3/2}\right)}{\varepsilon} \right) - 1 \tag{31}$$

Therefore, we can expect the sensitivity to be maximized in these regions due to an exponential change in tunneling probability, with the tradeoff that ΔI will be lower due to the absence of TEM and low initial current.

2.3.2 Device consideration 1: Double Schottky junction sensors for increased sensitivity

We have already identified that the maximum sensitivity is in the regions where trap-assisted tunneling is the dominant transport mechanism. Therefore, we choose to design our sensors to operate in these regions. We have two options for accomplishing this. First, we can operate in low forward biases where the tunneling current is still a large proportion of the total current. This is essentially a voltage lower than the threshold voltage. However, this limits the device to a small window of operating voltages, and is not ideal for realistic device operation. The second option is to operate the device in reverse bias, where trap-assisted tunneling is the dominant mechanism for all negative biases. If we wish to ensure that the device is always in reverse bias, we can design the sensor as a double Schottky junction device by using Pt for both contacts (Figure 17). In this circuit configuration, the current from a forward bias on one Schottky contact passes this potential barrier by TEM and tunnels through the second barrier. In this way the device current is always limited by the tunneling current and essentially in reverse bias for both positive and negative voltages.

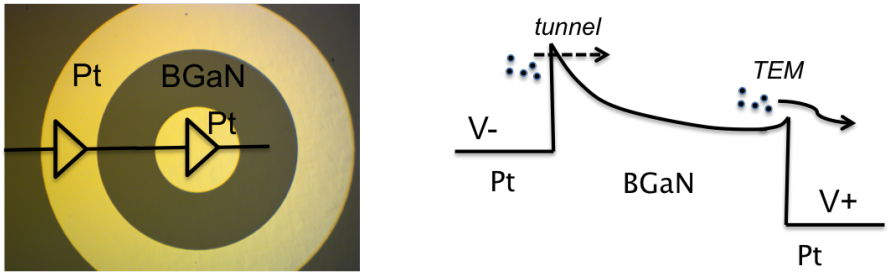

Figure 17. Metal-semiconductor-metal device (double Schottky design)

The added advantage of using a double Schottky junction with Pt contacts is that it reduces the number of steps during device processing. Pt contacts require photolithography using one mask, followed by one step of metal deposition and lift-off. In a standard MS

Schottky diode device, on the other hand, the ohmic contact must be deposited separately and annealed at high temperatures to ensure a low potential barrier. Therefore, using a double Schottky junction as opposed to an ohmic/Schottky configuration provides us with an easier and faster path for device fabrication. This also has implications for manufacturing of commercial devices; fewer processing steps greatly enhances the ability to mass produce sensor devices by increasing throughput.

2.3.3 Device Consideration 2: Quasi-alloy BGaN/GaN superlattice structures for tunable sensitivity

As mentioned, operating in the reverse bias increases sensitivity but decreases the initial current and ΔI of the sensor. The physical explanation for this stems from the assumption that as the interface trap concentration is increased, the bulk concentration increases as well. According to our equations for ΔI in both the forward and reverse bias, ΔI increases as a function of (1) the Schottky barrier height, which is proportional to the number of interface traps, and (2) the initial current. If we then include our assumption regarding the link between interface traps and bulk traps, the initial current should decrease as the number of interface traps increases. Therefore, there is a direct tradeoff and we expect to see an optimal value of total traps that maximizes the ΔI. The sensitivity, on the other hand, is not a function of the initial current and therefore we expect S to always increase as a function of total traps. From a design perspective, it would be ideal if we had a method of tuning both the total traps and initial current at the same time. As mentioned in section 1 of this chapter, the incorporation of boron in the crystal lattice increases the total trap density and also leads to deeper trap energies. This has previously been shown in a separate study by deep level transient spectroscopy (DLTS) measurements. However, the link between interface and total traps has not yet been decoupled, and therefore the interface trap density as a function of boron incorporation is not yet completely understood. If the ternary alloy BGaN is used as the semiconductor layer, it provides a method of tuning the total trap density and thus the sensitivity, but affects the initial current and thus ΔI as well. For example, a BGaN

monolayer with very high boron incorporation should yield a high S with a low ΔI, and visa versa. We propose the following model to explain the behavior of the initial current as a function of boron incorporation (Figure 18).

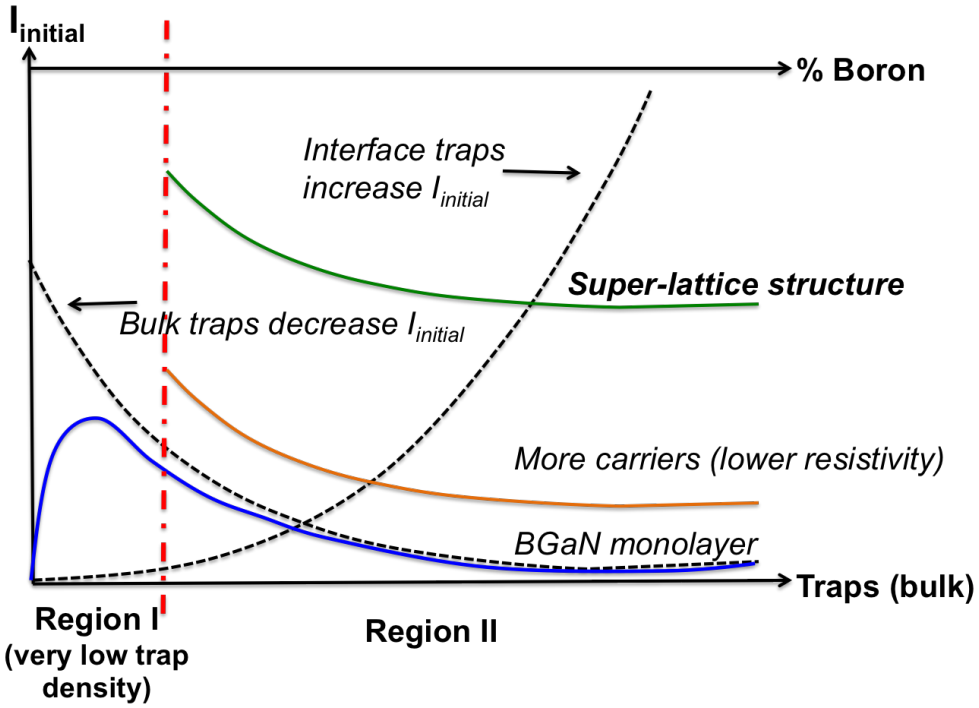

Figure 18. Proposed model of Schottky current as a function of total trap density

We divide the current vs. total drap density into two regions. In region I, the trap density is very low and the current increase from interface traps can increase the initial current. Again, it is important to point out that we are making the assumption that if the concentration of interface traps is increased then the bulk trap concentration will increase as well. When more traps are added by incorporating more boron in the crystal lattice, the resistivity increases exponentially and the dark current decreases. This is represented by region II, and is the most likely regime for our devices. The exact barrier between the two regions is, for the moment, purely theoretical and cannot be calculated without further DLTS studies. This is currently being undertaken as a part of another thesis and may be linked to our study at a later time.

If the resistivity of the device is decreased because of an increase in carriers, but not

due to a change in traps, the initial current for a given trap density is shifted up. Another option for decreasing the resistivity as a function of traps is to use a quasi-alloy of BGaN and GaN, known as a super-lattice structure (Figure 19).

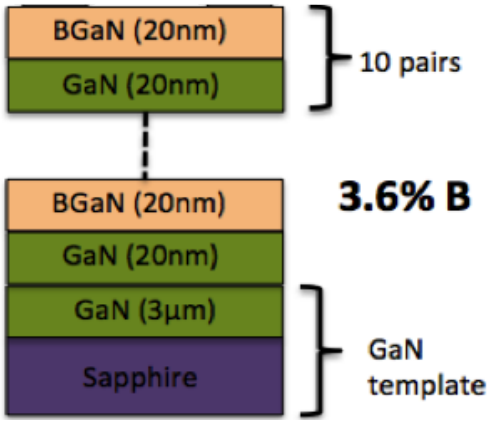

Figure 19. BGaN/GaN superlattice structure

In this structure, the resistivity is reduced drastically for a given trap density because the current passes through the BGaN layers and less resistive GaN layers in parallel, and thus the curve for dark current vs trap density is shifted up even further. This behavior is verified by the experimental current-voltage characteristics of BGaN monolayers with various boron incorporations as well as a BGaN/GaN superlattice with 3.6%B (Figure 20). From these experimental curves, it is evident that the initial current of the BGaN monolayers decreases as a function of boron incorporation. The BGaN/GaN superlattice shows an initial current that is a good balance between the BGaN monolayers and the GaN monolayer with much higher boron incorporation. The main advantage of this structure for sensing devices is that we can tune both the boron incorporation, and thus the interface trap density, and the dark current at the same time to obtain an optimal balance between sensitivity and ΔI. This also allows us to tailor the sensor performance for a particular application. For example, if a low detection limit is required, the BGaN structure can be tuned to have the maximum ΔI; conversely, if the signal is within the limits of the equipment it can be tuned to have a higher sensitivity at the cost of some ΔI.

Analytical modeling of the BGaN monolayer and BGaN/GaN superlattice-based double

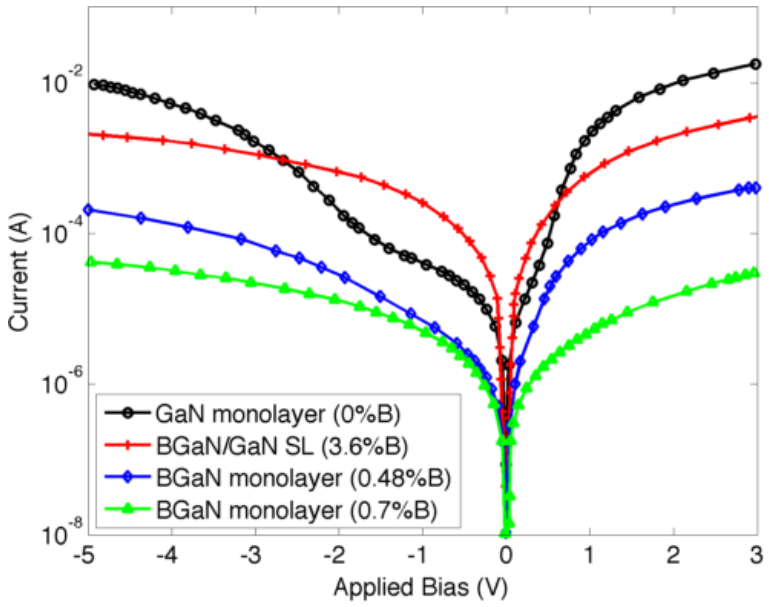

Figure 20. Current-voltage characteristics of BGaN monolayer and BGaN/GaN superlattice structures with various boron incorporations

Schottky junction sensors was performed to analyze the behavior of ΔI and S as a function of the total trap concentration. This will later be extended to include the boron incorporation when the study is linked with current DLTS studies (in a separate thesis) aimed at decoupling the interface and bulk trap densities as a function of the boron incorporation. For the modeling, NO_2 was used as the test gas using the adsorption isotherm and chemical model outlined in section 2 of this chapter. Since we are limited in our knowledge of the device current as a function of total trap density, we are forced to make assumptions about these functions for each device. We model the behavior for three devices: (1) a BGaN monolayer, (2) a BGaN monolayer with a higher background concentration, and (3) a BGaN/GaN superlattice structure. As mentioned, in our proposed model we assume that the initial current in Region II decreases exponentially as a function of total trap density.

In Figure 18, we assume three decreasing exponential functions. The exact exponential functions may vary in reality, but we use the assumption from our proposed model that the current for a given trap density will increase for the three modeled devices, respectively.

Using these functions, the ΔI and S is modeled as a function of the same total trap concentration (Figure 21). As predicted, the ΔI reaches an optimal value at an intermediate trap concentration while S increases due to increased interface traps and does not depend on the initial current (linked to bulk traps) of the device. For a given sensitivity, the BGaN/GaN superlattice structure shows the highest ΔI, indicating that it gives a good balance between the two metrics.

The same behavior is realized when the ΔI and S are modeled as a function of the initial current. The optimal ΔI (Figure 22) occurs at an intermediate initial current value that balances the Schottky barrier height change due to interface traps and initial current decrease due to bulk traps. For a given current, the BGaN/GaN superlattice device shows the highest ΔI value. Regarding the sensitivity, it is clear that S is maximized by increasing the number of interface traps, but since this is coupled with an increase in bulk traps it means that S is maximized at lower initial currents. Additionally, for a given value of S, the initial current is highest in the BGaN/GaN superlattice structure due to the parallel passage of current through less resistive materials while maintaining a high interface trap concentration from the terminating BGaN layer.

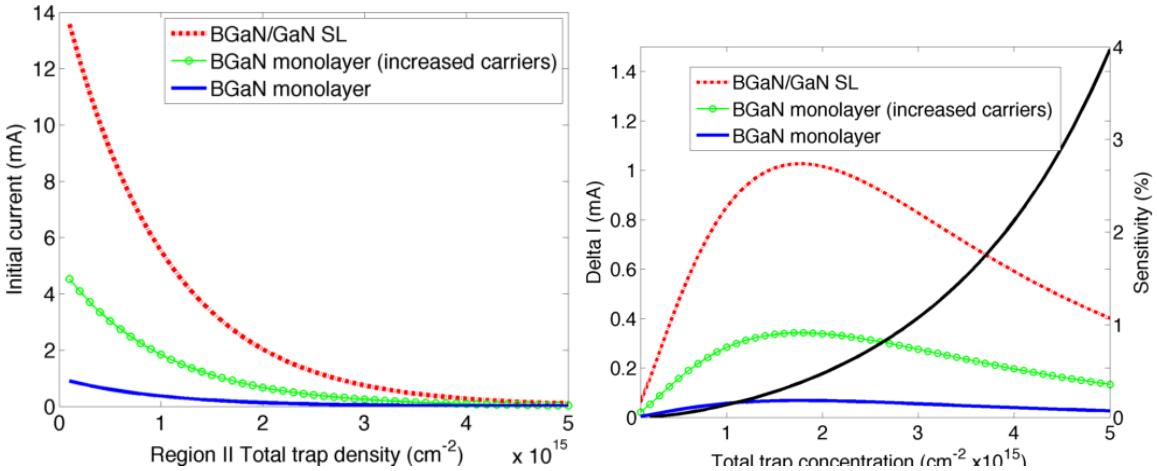

Figure 21. (a) Model of initial current as a function of total trap density in region II of our proposed model for BGaN devices (b) Model of ΔI and S as a function of total trap density for various BGaN devices

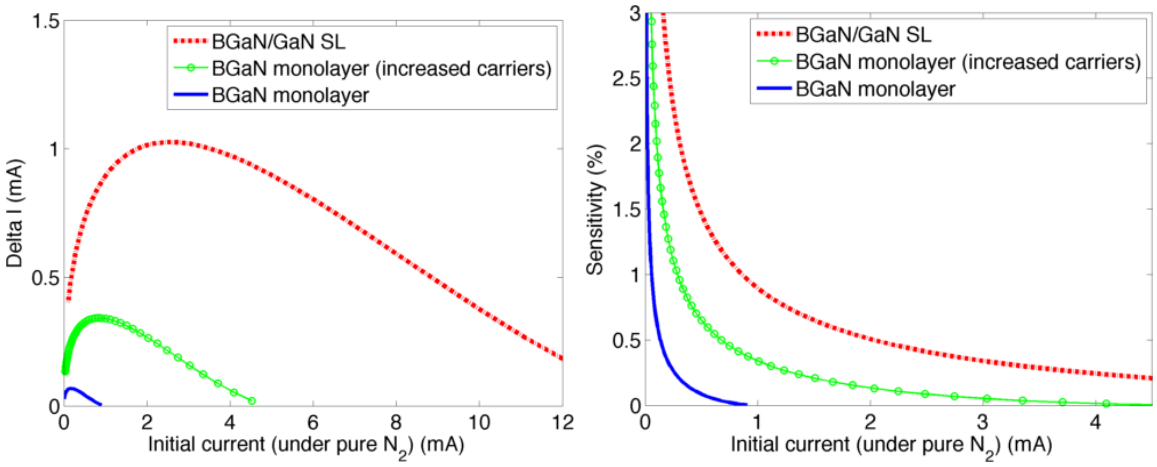

Figure 22. (a) Model of ΔI for BGaN devices as a function of initial current (b) Model of S for BGaN devices as a function of initial current

2.4 Gas sensors testing setup and experimental procedures

For experimental testing, a complete sensors testing lab was built in the Laboratoire Materiaux Optiques, Photonique et Systemes (LMOPS) (Figures 23 and 24).

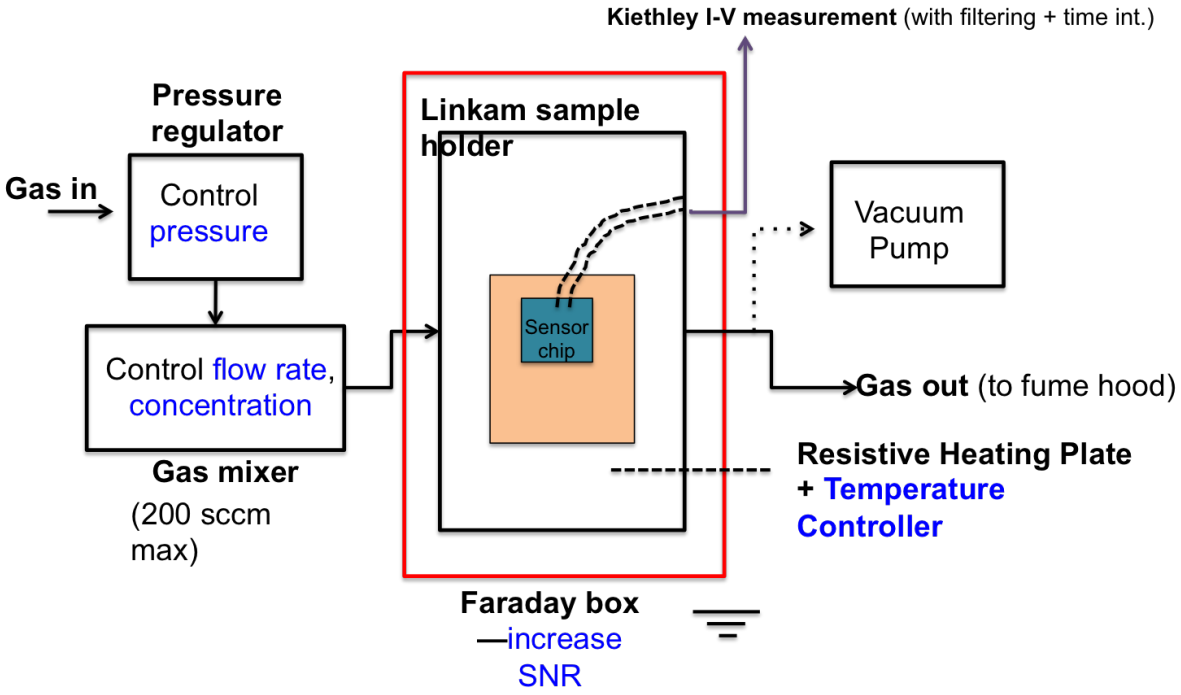

Figure 23. Experimental setup built at LMOPS for dynamic gas sensor testing

The devices were connected with probes in a Linkam gas chamber and connected to a Keithley 236 IV measurement system (Figure 25). In order to increase the signal-to-noise

Figure 24. Photo of the lab constructed for gas sensor testing

ratio, the gas chamber with all electrical connections was placed inside a Faraday cage. Gas sources of pure N_2 and 450ppm NO_2 with pressure regulators were connected to the testing chamber via a gas blender so that the pressure, concentration, and flow rate were all controlled during the measurements. The minimum concentration allowed using the gas blender was 1% of the compressed gas mixture (4.5ppm for NO_2). The temperature was controlled using an external temperature controller, and a vacuum pump was used to purge the chamber between gas measurements. A flow rate of 100sccm was used and with all external factors controlled, we can attribute any changes in the steady state signal to the gas detection mechanism previously described. For each measurement, the signal under pure N_2 was used as a reference for comparison with the signal under NO_2 in a background of nitrogen.

2.5 Highly Sensitive and Selective Detection of NO_2 Gas Using BGaN/GaN Superlattice-Based double Schottky Junction Sensors

In this section, we report a double Schottky junction gas sensor based on a BGaN/GaN superlattice and Pt contacts. NO_2 is detected at concentrations from 4.5-450 ppm with current responsivity of 6.7 mA/(cm^2*ppm) at 250 C with a response time of 5 seconds. The

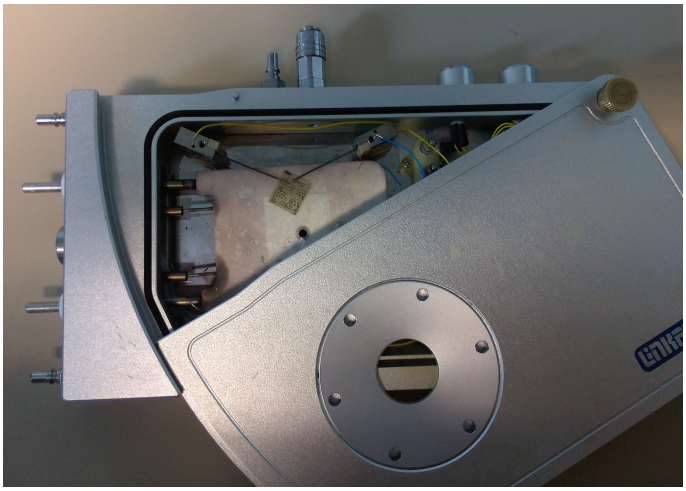

Figure 25. Linkam gas chamber used to connect sensor devices to the measurement system

sensor is also selective against NH_3. The BGaN layer at the surface increases surface trap density and trap depth, which improves responsivity and high temperature stability while the GaN layer improves the magnitude of the diode current. The BGaN layer's columnar growth structure also causes a Pt morphology that improves O_2^- diffusion.

2.5.1 Background

Nitride-based semiconductors are attractive materials for gas sensing applications due to their wide bandgap properties. Specifically, the high breakdown voltages and thermal stability of these materials make them suitable for high temperature applications in harsh environments (e.g. automotive exhaust systems or engines). Schottky diodes and MOSFET devices using a variety of semiconductor materials have previously been demonstrated for detection of hydrogen and other gases [34, 35, 60, 61], but their use for NO_2 sensing has not been widely explored. One potential application for NO_2 sensing is in the selective catalytic reduction of NO_x by injection of NH_3 in an automotive exhaust. Requirements for this application are high sensitivity and responsivity to the target gas, high thermal stability, and complete selectivity between NO_x and NH_3. The general mechanism of gas detection by Schottky diode sensors is attributed to the dissociation of gas molecules after physisorption on the catalytic Pt surface [27]. The charged gas ions (negative oxygen

ions in the case of NO_2) then diffuse through available grain boundaries or pores in the Pt contact and are chemisorbed at available interface traps on the semiconductor surface. The additional negative charge at the interface must be compensated by a more positive depletion region and an increase in the Schottky barrier height (SBH) $\Delta\phi_B = \frac{N_i\rho\theta}{\epsilon\epsilon_0}$, where N_i is the interface trap concentration, ρ is the dipole moment between the gas and the traps, and θ is the fraction of interface traps occupied by gas ions [62]. The increase of the SBH corresponds to a lowering of the device current. A second mechanism may also occur where the molecule or reaction intermediates interact either capacitively or directly with the interface traps via pores in the metal contact [38]. Furthermore, the thickness and morphology of the contacts has been shown to affect gas sensitivity [29] and is a possible strategy for selective detection of different species of gas. To analyze sensor performance, one can measure the absolute current change, $\Delta I = I_{gas} - I_0$, or the relative sensitivity, $S = \frac{\Delta I}{I_0}$, where I_0 is the initial current when no gas is applied. In order to compare sensors that have different initial current values or measure different concentration ranges, we also can use the sensor responsivity $R = \frac{\Delta I}{area \times \Delta C}$, where ΔC is the change in concentration of gas. Schottky diode sensors based on 4H- and 6H-SiC with a thin Pt contact were shown to have a rather large value of S=19.35% to 200ppm NO_2 at 300°C [33], but with a very low value of R=.002 $mAcm^{-2}ppm^{-1}$ and slow response time, of the order of several minutes (see table 4). A separate study [34] using n-type GaN Schottky diode sensors with a 75 nm-thick Pt contact showed an improved response to NO_2 at 300°C compared to SiC-based sensors, but a quantitative comparison of the responsivity and/or sensitivity was not possible using the reported metrics. A Pt/AlGaN/GaN HEMT structure was shown to exhibit a decreased S=10% due to a higher initial current, but a significantly higher R=1.14 $mAcm^{-2}ppm^{-1}$ at 400°C [38]. This tradeoff between the ΔI (and thus the responsivity) and sensitivity is explained by the fact that the ΔI for Schottky diodes is given by the expression $\Delta I = I_0 e^{\frac{\Delta\phi_B}{kT}} - 1$, which is derived from the thermionic emission transport model. Therefore, a high initial current results in high responsivity whereas the sensitivity is increased with a large increase

Table 5. Comparison of NO_2 sensor performances, including sensitivity (S), responsivity (R), response time (τ_r) and recovery time (τ_R).

Device	Catalyzer	I_0 (mA)	ΔI (μA)	S (%)	R ($\frac{mA}{cm^2 * ppm}$)	T (C)	τ_r/τ_R (s)	Ref.
SiC Schottky Diode	20-40nm Pt	0.02	3.8	19.35	0.002	300	90/120	[33]
SNO_2 Schottky Diode	-	0.42	243	58.3	⩽648	150	43/37	[38]
AlGaN/GaN HEMT	Pt	5	500	10	1.43	400	n/a	[29]
GaN Schottky Diode	20 nm Pt	11.5	370	3.2	1.14	200	300/300	This work
BGaN SL MSM	100 nm Pt	7.07 ± 0.3	2140 ±105	**30** ±**1.5**	**6.7** ±**0.3**	250	**5/80**	This work

in $\Delta\phi_B$ caused by a high concentration of interface traps, which results in a lowering of the initial current. Finding a balance between ΔI and I_0 is exemplified by the work of Quang et al. [39] who reached large ΔI while maintaining relatively large I_0 in SNO_2 nanowires-based Schottky junction (SJ) gas sensor, and thus resulting in outstanding values of both sensitivity and responsivity (see table 5). Furthermore, even if limited to very low gas concentration (tens of ppb) and rather low operating temperature (150°C), the response time (τ_r) of the device was shown to be relatively fast at 43 seconds with a recovery time (τ_R) of 37 seconds. Finally, Schottky sensors for NH_3 detection have also been reported [40, 41], but complete selectivity between NO_x and NH_3 has not yet been demonstrated with these types of devices.

In this work, we report double SJ NO_2 sensors based on GaN materials that exhibit large sensitivity and responsivity with tunable electrical conductivity (to adjust I_0) and carrier trapping efficiency (to adjust $\Delta\phi_B$ and thus ΔI). To achieve this, quasi-alloys of BGaN/GaN superlattices (SL) were used as active layers. Indeed, we have shown previously that the electrical conductivity of the BGaN alloy can be tuned over more than seven orders of magnitude using low boron incorporation concentration (less than 2%) [63]. Furthermore, we have also shown an enhancement of the $\Delta\phi_B$ originating from an increase of the trapping efficiency due to boron incorporation in the BGaN quasi-alloy. BGaN/GaN SL structures allow more flexibility in the tuning of the boron incorporation in thick layers compared to BGaN monolayers [47]. We also choose to use a double SJ MSM design that is more

simple to fabricate compared to Schottky diode or HEMT structure. The performance of this device for NO_2 detection is compared to double SJ Pt/GaN reference devices that we have fabricated and other reported Schottky and HEMT devices for NO_2 detection.

2.5.2 Device Fabrication

The reference device used in this work is a commercially available 400nm thick n-type GaN (Si-doped). The BGaN/GaN SL structure was grown using 10 periods of 20nm thick un-doped GaN and 20nm thick BGaN with an average boron concentration of the quasi-alloy of 3.6%. The structure was grown by MOCVD in a T-shaped reactor using trimethylgallium, triethyl boron, and ammonia as the gallium, boron, and nitrogen sources, respectively, with nitrogen as the carrier gas. For device processing, the layers were first cleaned using acetone and isopropynol, followed by 10 minutes in HCL to remove the oxide layer. After lithography and lift off, Pt was sputtered at a pressure of 3μbar at a thickness of 100nm, followed by liftoff. Another device was processed with 20nm Pt using the same conditions on the n-type GaN sample. The circular diodes have a 300μm diameter with a 200μm spacing between the two Pt contacts (see Figure 26).

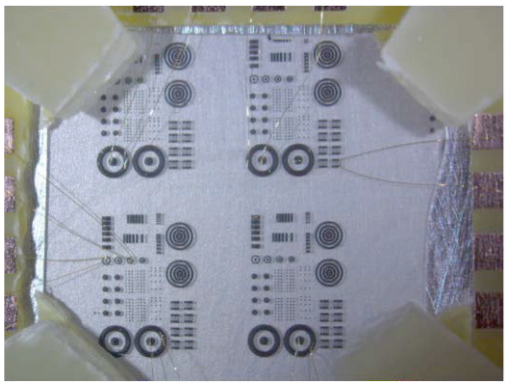

Figure 26. Optical image of the sensor device bonded with gold microwires to copper electrodes; the circuit board was designed for use in the Linkam measurement system

2.5.3 Experimental results

The ΔI and S of the GaN and BGaN/GaN SL devices upon exposure to 450ppm NO_2 gas are shown as a function of temperature in Fig.27.

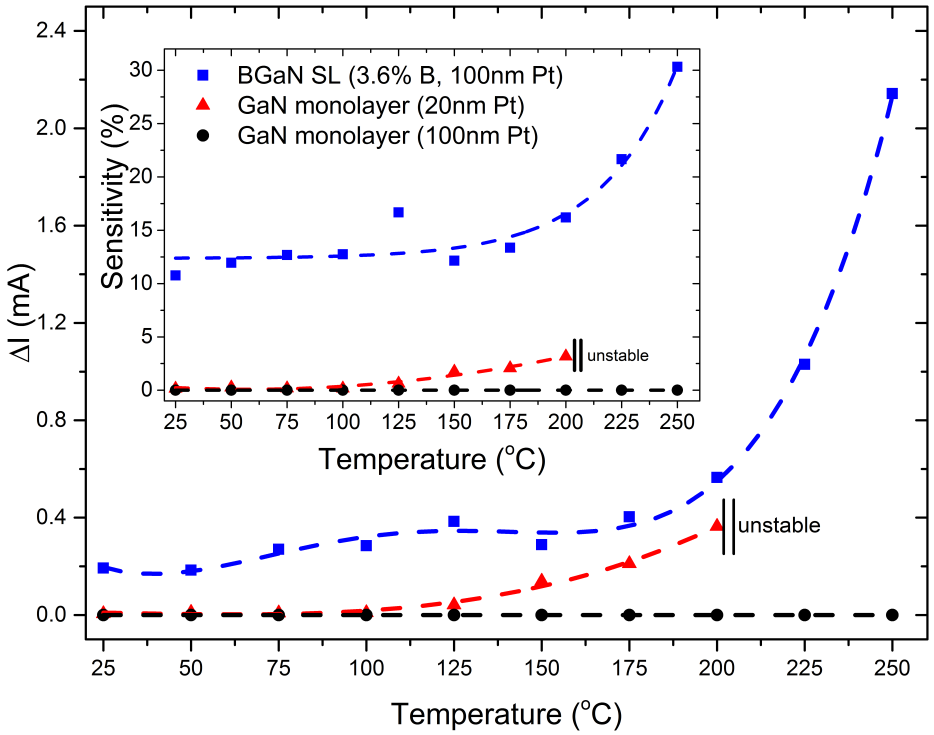

Figure 27. Comparison of the temperature dependence of ΔI and S (inset) of BGaN/GaN SL and GaN sensors to 450 ppm NO_2 at 5V bias.

For the BGaN/GaN SL device with 100nm thick Pt layer, a ΔI of 215 μA and S of 12% were obtained at 25°C, compared to 14μA and 0.1%, respectively, for the GaN device with a 20nm thick Pt layer. It is important to note that the GaN device with a Pt thickness of 100nm showed no sensitivity or current change with gas exposure, likely due to a continuous Pt layer with no grain boundaries for oxygen diffusion as shown by scanning electron microscopy (SEM) images of the device surfaces (see Fig.28).

For both samples, the ΔI and S are shown to increase with temperature. In the case of the BGaN/GaN SL device, the measured values of ΔI fluctuate slightly, which is probably due to motion of the contact point of the electrical probe tips, observed with increasing the temperature. This did not occur with GaN devices which were wire-bonded to the contact pad. Nevertheless, according to these results, the ΔI and S of the BGaN SL device are significantly higher than both the GaN reference device and the devices reported in literature (see table 5), reaching values of 2140μA and 30%, respectively, at 250°C. This

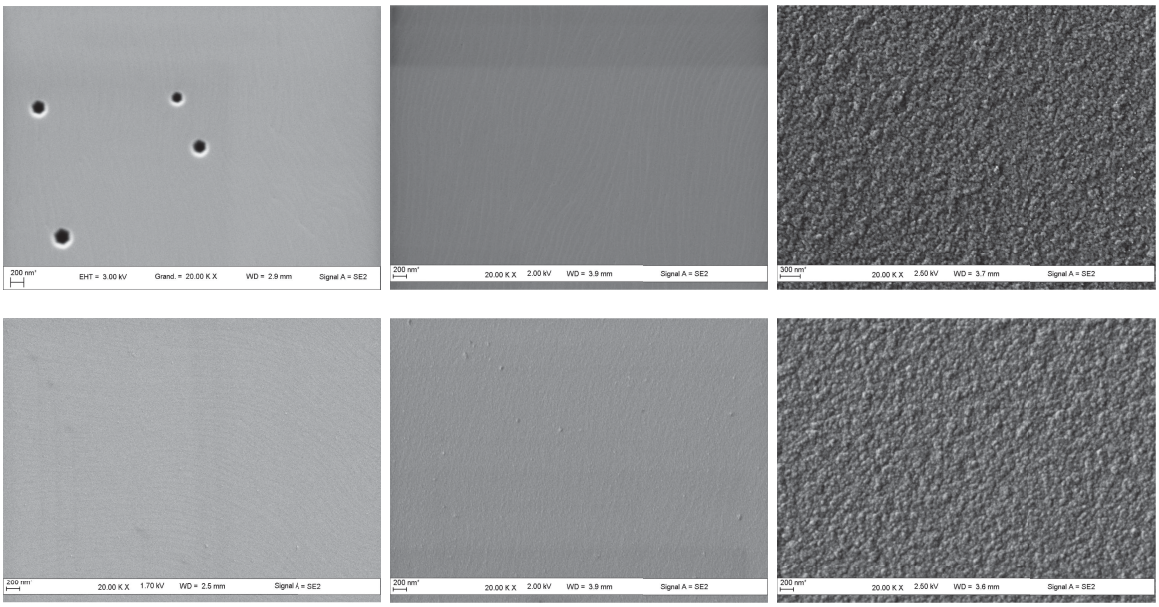

(a) (b) (c)

Figure 28. Device surfaces before (top) and after (bottom) Pt deposition for (a) GaN monolayer with 20nm thick Pt layer (b) GaN monolayer with 100nm thick Pt layer c) BGaN/GaN SL with 100nm thick Pt layer.

means that the BGaN superlattice structure offers a good balance for high S and ΔI, whereas other devices show a significant tradeoff between the two metrics. The improved sensitivity of the BGaN SL sensor can be explained by a combination of two mechanisms. The first is that BGaN material has more interface traps than GaN and thus more adsorption sites for the oxygen ions. This results in more gas coverage at the interface and a larger SBH change. The secondary advantage of the BGaN layer is that it exhibits columnar growth (Figure28c (top)), decreasing the volume-to-area ratio at the interface. This means that it is possible to have more interface traps within a given area. Additionally, the columnar surface of BGaN causes the Pt layer to have more grain boundaries (Figure 28c (bottom)), increasing the diffusion of the oxygen ions through the Pt contact to the interface traps. Furthermore, ΔI is not sacrificed due to the higher-conductivity GaN interlayers in the superlattice structure, which serve to increase the I_0. This leads to both high responsivity and sensitivity to NO_2 for the BGaN/GaN SL sensor, with a responsivity of $6.7\pm0.3 mAcm^{-2}ppm^{-1}$ at 250°C, as shown in table 5. This is significantly higher than the responsivity for other reported devices

except the SNO_2 nanowires-based SJ gas sensor.

For all samples tested, we found that there was a memory effect after gas exposure and that it was necessary to reset the sensor by increasing the temperature and purging the test chamber between each measurement. Temperatures of 100°C and 300°C were required to reset the GaN and BGaN/GaN SL samples, respectively. This result is consistent with chemisorption at the interface as the mechanism responsible for the SBH change. Chemisorption requires the additional energy present at higher temperatures in order for desorption to to break the bonds of absorption. DLTS measurements, not shown here, indicate that electron traps in BGaN material become deeper with boron incorporation, which can explain the higher reset temperature required for the BGaN/GaN SL sensor. It is to be noticed that the GaN sensor becomes unstable above 200°C due to a drift in baseline current, making it impossible to take a reliable measurement at these temperatures. The cause of this drift is currently being explored, but may be due to the thin Pt layer used. After returning to temperatures below 200°C the baseline remains stable.

To further analyze the thermal stability of the devices, measurements were taken as a function of applied bias at 150°C. In SJ device gas sensor, in opposite to S which is only a function of the change in SBH and is expected to remain constant after a steady state value is obtained, ΔI and R are proportional to I_0 and thus their values should increase with increasing bias voltage. The dependence of ΔI and S on applied bias is shown for the BGaN/GaN SL and GaN sensors at 150°C (Figure 29). As expected, ΔI increases with increasing bias voltage up to 5V for both devices (see inset), but S reaches a constant value only for the BGaN/GaN SL device and bias larger than 2V. On the contrary, the GaN sensor exhibits a maximum S followed by a decrease at higher voltages. This decrease could be attributed to a temperature-dependent avalanche effect that is proportional to the initial current. Under high electric fields there is an increase in tunneling through the barrier and a reduction of the effective barrier height. This additional tunneling current diminishes the effect of the increase in barrier height due to the gas, thereby reducing the sensitivity. At

150°C, BGaN does not exhibit the same avalanche effect due to a lower initial current and therefore does not exhibit the loss in sensitivity at increased voltages as does GaN at the same temperature. This result further demonstrates the improved thermal stability of the BGaN sample compared to GaN.

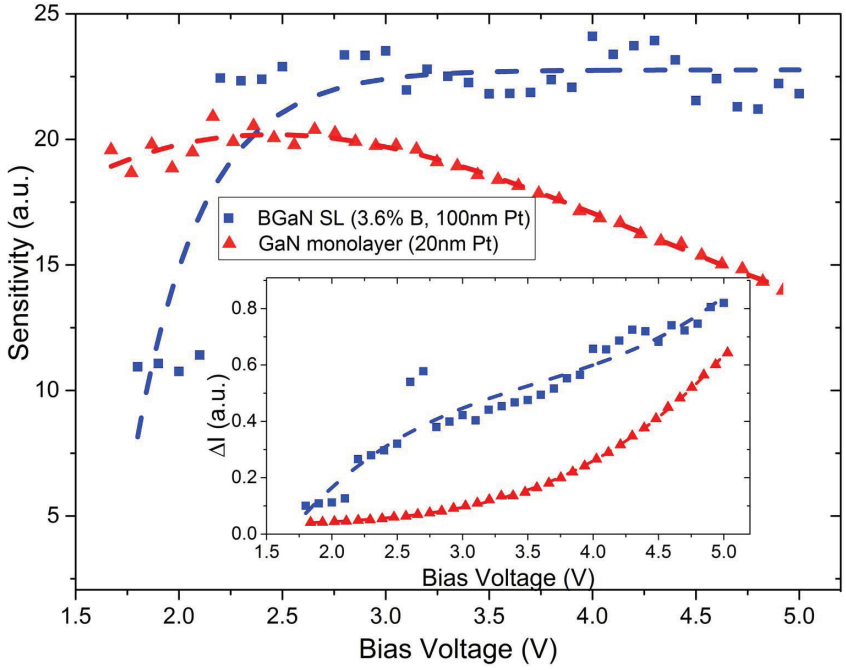

Figure 29. ΔI and S of the BGaN/GaN SL and GaN sensors in 450ppm NO_2 as a function of applied bias at 150°C. Values are given in arbitrary units so that the trends can be placed on the same scale.

The evolution of the electrical current for the BGaN/GaN SL sensors under intermittent flows of 450ppm NO_2 and pure N_2 gas at 300°C and 5V bias is exemplified in Figure 30. The signal for the BGaN/GaN SL device is shown to decrease to a steady-state value under NO_2 proportional to the concentration, and to recover to the initial value under a flow of pure N_2. The response time, τ_r, was measured by allowing the signal to reach steady state under NO_2 and calculating the time between 10-90% of the steady state value. At 300°C, the response time was 5s for the BGaN/GaN SL device, and was indeterminable for the GaN device due to the instability at this temperature. Measurements at 150°C showed response time for the GaN device on the order of a few minutes. The full recovery time, τ_R for the BGaN/GaN SL device was measured to be 80 seconds at 300°C.

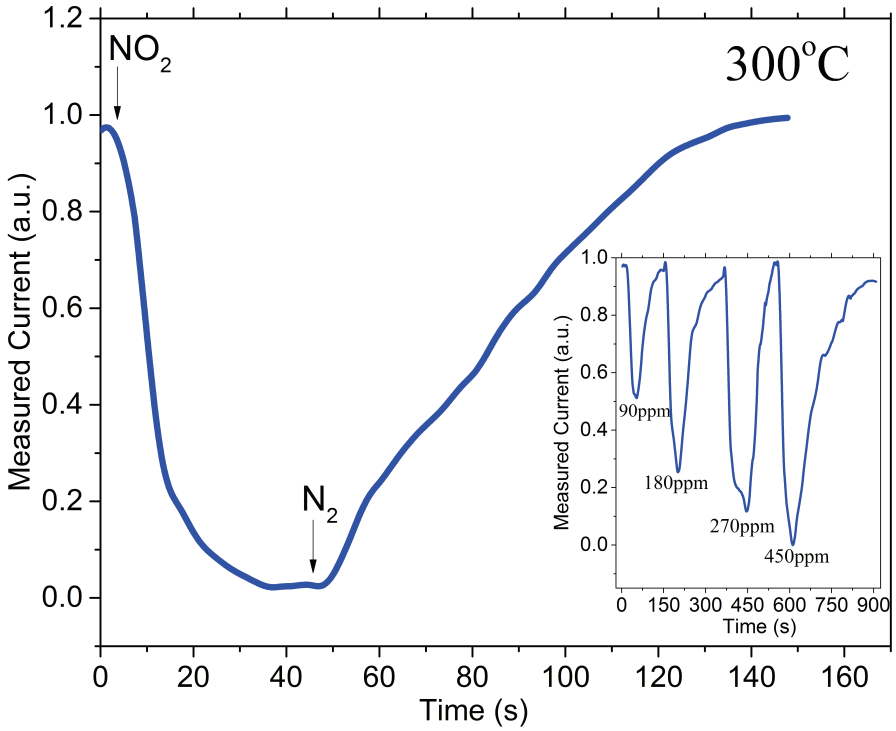

Figure 30. Measured current (in arbitrary units) for the BGaN/GaN SL sensors under intermittent flows 450ppm NO_2 and pure N_2 gas at 300°C and 5V bias. The inset shows the measurement repeated between 90-450ppm NO_2

.

The measurement was repeated with varying NO_2 concentrations from 90-450ppm at 300°C, showing that the ΔI is proportional to the concentration of gas (see inset of Figure 30). We notice that at different concentrations, the recovery time is not always the same. This could be due to a difference in trap energies affecting the chemisorption of the gas. At this temperature, we begin to see saturation of the signal change leading to a nonlinear response for the BGaN/GaN SL as a function of concentration, whereas it remains linear at 150°C for both the BGaN/GaN SL and GaN monolayer devices (see Figure 31). This means that at higher temperatures and concentrations, it is possible to have a decrease in the responsivity of the device.

Finally, the BGaN/GaN SL device was tested in 15ppm of NH_3, and showed no current change under the applied gas even at a temperature of 250°C. At this temperature we measured a sensitivity of more than 2% to 15ppm NO_2, indicating that the BGaN device

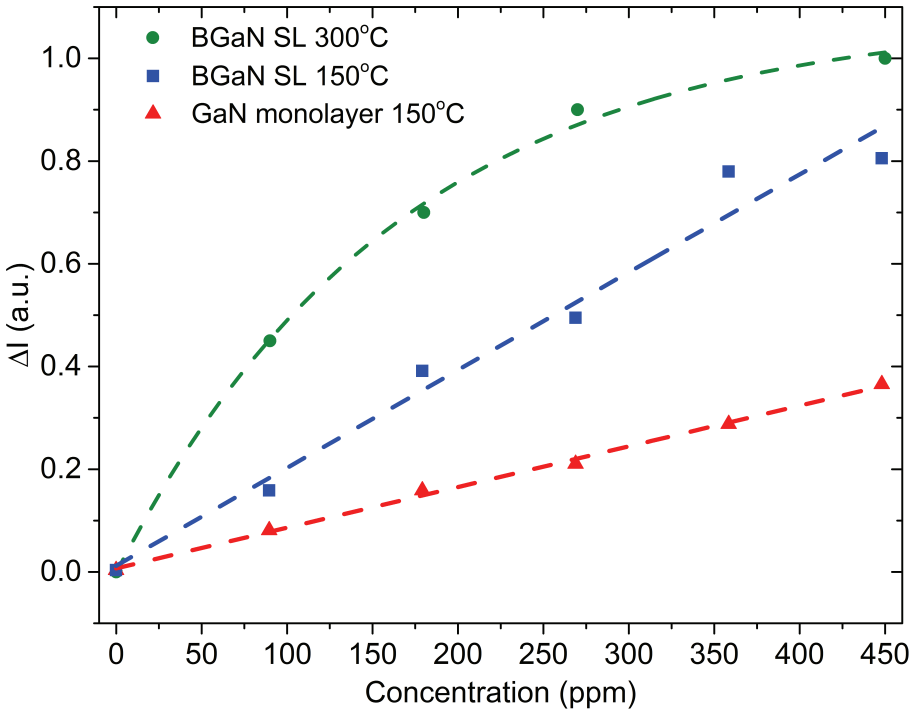

Figure 31. ΔI as a function of concentration for various temperatures, showing a linear response below 300°C

.

shows a very good selectivity between NH_3 and NO_2. This has not yet been demonstrated by other SJ or MOSFET sensor devices. The GaN device was not responsive to 15ppm of either NO_2 or NH_3, most likely because this concentration of NO_2 is below the detection limit of GaN sensor. The selectivity for the BGaN/GaN SL device may be attributed to a different detection mechanism for NH_3. One possible mechanism predicts that NH_3 dissociation occurs most readily at triple points where the Pt, semiconductor, and gas are all in contact simultaneously [29]. Typically, these triple points require pores in the Pt layer; however, in the BGaN/GaN SL device no pores can be observed from the SEM images (Figure 28c (bottom)) due to the thick Pt contacts. Instead, we only see grain boundaries which allow O_2 ion diffusion, but not NH_3 dissociation/diffusion. Therefore, we may be able to alter the Pt thickness or morphology to obtain sensitivity to NH_3 in addition to NO_2, as well as further selectivity between different gases. This is currently being investigated.

2.5.4 Conclusions

We have shown that SJ gas sensors based on a BGaN/GaN SL structure exhibit high responsivity and a good balance between responsivity and sensitivity. At the same time, the sensitivity of the BGaN/GaN SL sensor is also significantly higher, making it the best choice for balancing the responsivity and sensitivity. This means that the BGaN/GaN SL sensor can be operated at a target detection limit while maintaining a higher SNR compared to the other sensors. Additionally, the BGaN/GaN SL sensor shows better thermal stability and a faster response time than the GaN-based sensor, and the ability to selectively detect between NH_3 and NO_2.

2.6 Selectivity study for NO_2, NO, and NH_3 using various Pt thicknesses and morphologies

We have shown in the previous section that selectivity to NO_2 was achievable for our double Schottky junction device by carefully designing the thickness and morphology of the Pt sensing layer such that it favors the diffusion mechanism of ionized oxygen while preventing the detection mechanisms of NO or NH_3. This was accomplished using a thickness of 100nm such that no pores are present in the Pt layer, while grain boundaries are formed due to the columnar growth of the BGaN surface morphology.

Since the sensitivity of different gases depends on both the thickness and morphology of the Pt contact, one strategy we wish to explore for obtaining complete selectivity between different gases is to alter these parameters to isolate the different detection mechanisms. We outline several pathways for this study (Figure 32).

A two-inch wafer of BGaN/GaN superlattice structure was grown using the same design and growth parameters as in the previous study. XRD and cathodoluminescence measurements verify the boron incorporation to be approximately 1.3% for each layer and AFM shows a surface roughness of 3.8nm; these characterizations are consistent with the structure previously used. Cathodoluminescence measurements revealed clear peaks at 367nm

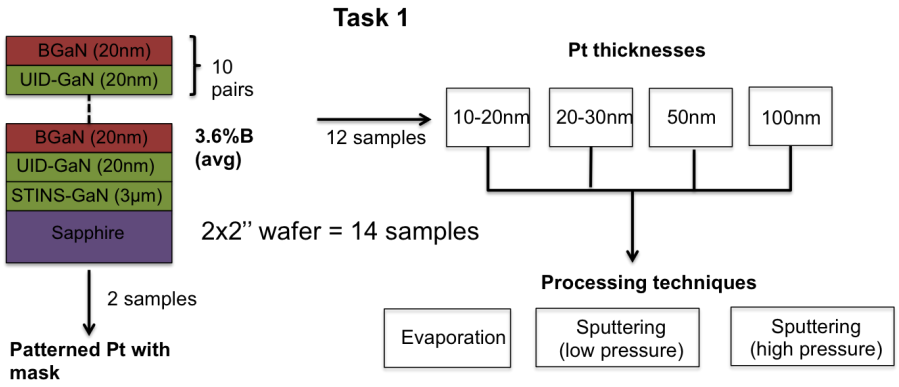

Figure 32. Process flow for selectivity study

and 380nm, corresponding to the GaN and BGaN layers, respectively, matching the measurements on the previous sample and are consistent with the expected bandgap bowing of BGaN. However, a larger defect band in the blue wavelength region was present; this defect band was also present in other samples grown around the same time and is likely an issue with the reactor. For this reason, the sensing properties cannot be directly compared to the results obtained in the previous section, and a new reference sample will be processed using the same conditions (100nm Pt sputtered at 3μbar) to account for this.

The morphology of the Pt sensing layer can be modified using different processing techniques (i.e. sputtering vs evaporation) or by patterning the Pt into nanocolumns or other structures using a mask. We have also demonstrated that it is possible to form nanocolumns of BGaN at the semiconductor surface by using hydrogen as the carrier gas during MOCVD (Figure 33). This provides a possibility of patterning the Pt without the use of a mask, which will later be explored. For this study, the BGaN wafer was cut into 1cm squares and is currently being processed at IEMN following the process flow depicted in Figure 32.

(a)

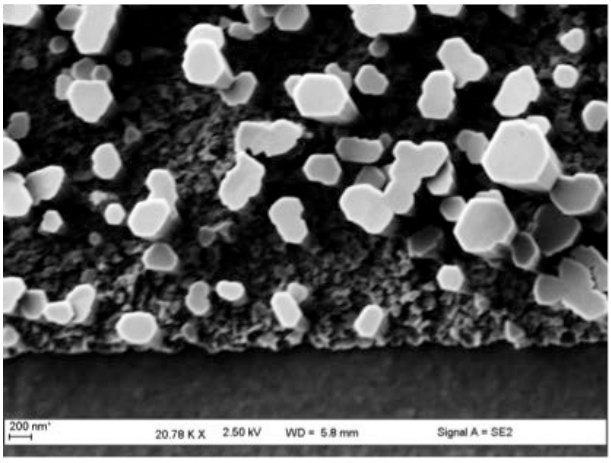

(b)

Figure 33. (a) BGaN monolayer surface (300nm, 1.45%boron) grown on GaN template under hydrogen with nonhomogenous distribution of nanocolumns (b) BGaN monolayer surface (300nm, 1.45%boron) grown on AlN/Si template under hydrogen with tall homogenous nanocolumns

CHAPTER 3

ALGAN/GAN HIGH ELECTRON MOBILITY TRANSISTOR SENSORS

3.1 HEMT sensor theory and principle

In recent years, AlGaN/GaN high electron mobility transistors (HEMTs) have been shown to be an attractive option for high sensitivity detection of molecules in gas and liquid mediums. Due to the high gain property of transistor devices, HEMTs with functionalized gates have been shown to reach sub ppm sensitivities to their target molecules [64]. In addition, the high bandgap of nitride materials causes the device to be resistant to degradation in harsh chemical and high temperature environments [65]. AlGaN/GaN HEMT sensors are attractive options for gas sensing due to their material and electrical properties. Spontaneous and piezoelectric polarization induced at the AlGaN/GaN interface results in a net positive charge at this heterointerface and a net negative charge on the surface. It is electrostatically favorable to balance this positive charge as close to the charge layer as possible, so as the AlGaN layer thickness increases a negatively charged two-dimensional electron gas (2DEG) forms at the heterointerface and a 2DEG hole gas forms near the surface [66] (Figure 34). The carriers in the 2DEG are free to move with low probability of obstruction from other carriers or phonons; mobilities have been measured at values up to 2050 cm^2/Vs [67]. On the top of the AlGaN layer, two ohmic contacts labeled the source and drain form a circuit with a voltage source and act as the source of electrons in the 2DEG channel. A Schottky contact, known as the gate, adds a potential barrier that the electrons must cross to enter the channel and is controlled using a bias voltage. Compared to other MOSFET devices, AlGaN/GaN HEMTs have the advantage that they do not need to be doped due to the inherent polarization charges, resulting in a higher mobility.

For sensing applications AlGaN/GaN HEMT devices can be modified using a functionalized gate that allows detection of specific molecules (Figure 35). When a molecule

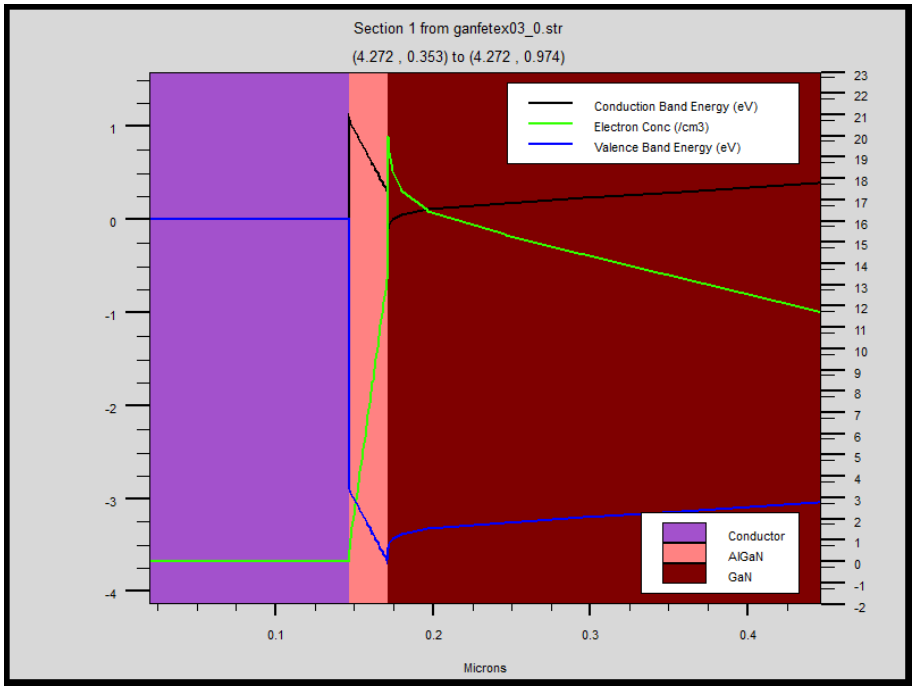

Figure 34. Band diagram of AlGaN/GaN HEMT structure with a Pt gate, showing the formation of a 2DEG quantum well with high carrier concentration

is adsorbed on the functionalized gate, the molecule or its reaction intermediates diffuse through the gate and form a chemisorption with interface traps, changing the potential at the metal/semiconductor interface following the same adsorption isotherms as the Schottky diode sensors previously discussed. The change in Schottky barrier height, $\Delta\phi_B$, is equivalent to a change in bias voltage of the same magnitude and induces a change in carrier concentration in the 2DEG; since the output signal is highly sensitive to the channel concentration, the result is a large change in current in the presence of the target molecule capable of sub-ppb level detection with a response time on the order of minutes or seconds [30]. In general, nitride semiconductor materials are attractive for automotive exhaust applications due to their high thermal and chemical stability. Sensors based on AlGaN and GaN have been operated at temperatures of 600°C with little degradation or irreversible effects [53]. Pt is a good choice for the sensing contact due to its exceptionally high melting temperature of 1772°C as well as its ease of use in contact processing on nitride materials. These materials are also relatively inexpensive, making them viable options for commercial

products.

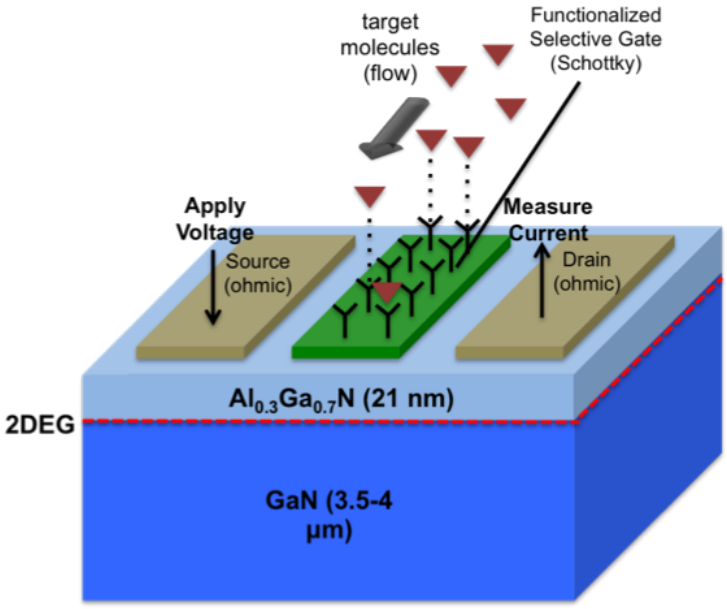

Figure 35. Operating principle of AlgaN/GaN HEMT sensor with functionalized gate

3.2 Analytical modeling of AlGaN/GaN HEMT sensors

An analytical model for AlGaN/GaN HEMT response to various gas species was developed in order to optimize the design of HEMT sensor parameters including the composition of semiconductor materials, functionalized sensing contacts, operating parameters such as applied bias, and environmental parameters such as temperature and gas concentration. This type of model can also give valuable insight into the chemical reactions occurring at the AlGaN surface, which may provide a pathway for selective devices. Both of these points will be discussed in detail in the following sections, and the model will be outlined in the current section. While several analytical and physics-based models for the current-voltage characteristics of AlGaN/GaN HEMTs have already been developed, and kinetic analysis of metal-semiconductor based sensors has been studied for hydrogen gas detection, there has never been a complete, comprehensive model that can predict the response of HEMT sensors as a function of all of these physical and chemical parameters.

The model by Li and Wang [68] develops an analytical expression for mobility that

takes into account the effects of the electric field in the channel and models the drain current as a function of drain and gate voltage biases. An analytical model for the nonlinear polarization effects have been modeled in [69], and analytical expressions to model the temperature effects of each of the HEMT parameters has been developed in [70]. The chemical mechanisms for hydrogen detection for AlGaN/GaN HEMT sensors utilizing a Pt gate have been studied using analytical expressions for the surface charge changes at the Pt/AlGaN interface, and has been extended to include thermodynamic effects at various temperatures for hydrogen gas detection by [53]. Several experimental studies on AlGaN/GaN HEMTs have been carried out that show a measurable current change upon exposure of the device to different gases, although there is variation in the reported current and sensitivity values [38, 71–73]. An AlGaN/GaN HEMT sensor for hydrogen detection has also been modeled and experimentally tested to examine the sensitivity as a function of temperature and gate bias [74].

It is known that the sensitivity of the HEMT sensor to a target gas is related to the interaction of the reaction intermediates with interface states between the gate and the semiconductor layer. As explained in chapter 2.2, the exact interaction mechanism depends on the total number of interface states, the coverage by gas molecules, and the type of interface state. However, it is difficult to measure the exact interface state concentration for a HEMT device because it is a dynamic system that responds to changes in the ambient conditions and depends on defects and other properties of the AlGaN surface that are often difficult to quantify. This makes it difficult to understand exactly how the material properties affect the sensing mechanism. In previous HEMT sensor experiments, reported current changes for 500ppm of hydrogen range from hundreds of microamps to a few milliamps even when the known physical parameters of the devices are comparable [38, 71–73]. This disparity in results has not yet been explained. We predict that the disparity may be in part due to differences in interface state concentrations which stems from different growth and processing steps.

In this section, we give a detailed description of the HEMT sensor model including the calculation of charge control and current-voltage characteristics of AlGaN/GaN HEMTs and combine this with the modeling of the chemical interactions of gas molecules with the Pt gate that was described in chapter 2.2. The first model was developed for detection of hydrogen gas since it has the most understood and simplest reaction mechanism and is the most studied type of HEMT sensor. This allows us to make the fewest assumptions and more easily validate our model with reported experimental results. The model is later extended to include the detection mechanisms of NO, NO_2, and NH_3 and compared with our own experimental results for those gases.

3.2.1 Overview of Device Simulations

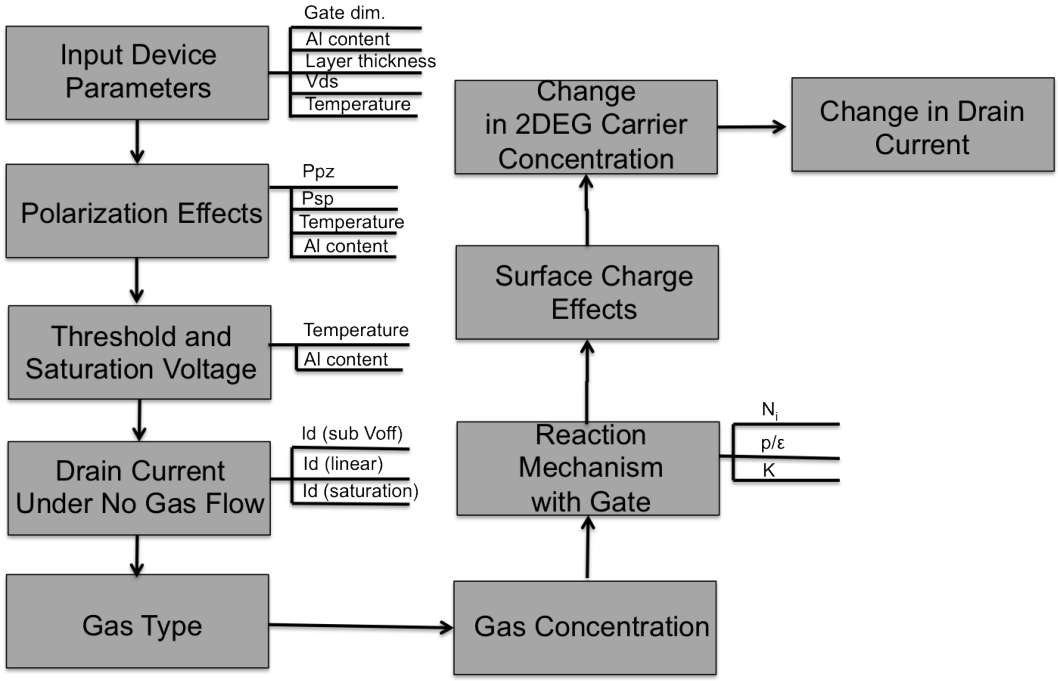

Figure 36. Flow chart depicting the components of the device simulation

The HEMT sensor simulation is comprised of several analytical expressions that are implemented in MATLAB and used to model the device behavior for specific inputs. The outline of the simulation is depicted in Figure 36. The primary inputs required for the simulation are the gate dimensions, aluminum mole fraction, AlGaN thickness, source-drain

voltage, and operating temperature. The piezoelectric and spontaneous polarization are determined for the primary inputs, and the threshold and saturation voltages are calculated. The drain current as a function of the gate and drain biases (without the presence of gas) is solved using a charge control model. The reaction mechanism between the gas and the gate is then modeled for the specific gas type and concentration. For optimization purposes, the simulation is run using a range of gas concentrations in order to identify ΔI and sensitivity trends for a given device parameter. The analytical model for the surface charge effects determines the change in the 2DEG carrier concentration for each gas concentration, which is used to find the new I-V characteristic in the presence of the target gas. This is compared to the I-V characteristic without the presence of gas to determine the absolute current change and device sensitivity. The chemical interactions of hydrogen and other gases with the Pt gate is described using a Tempkin isotherm and was explained in more detail, including an in depth discussion of all of our assumptions, in chapter 2.2.

3.2.2 Charge control and I-V characteristics as a function of temperature

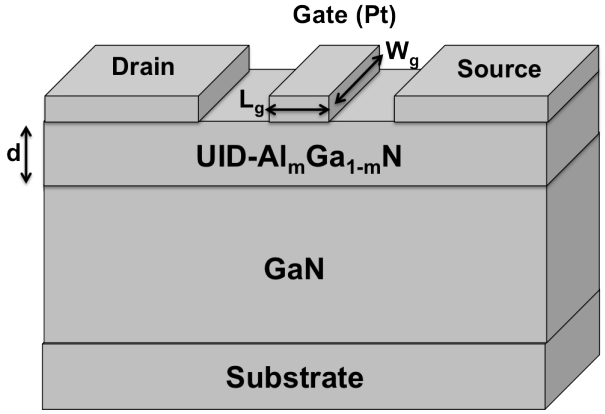

Figure 37. AlGaN/GaN HEMT sensor structure used in device simulations

The current-voltage charactaristics of the AlGaN/GaN HEMT device shown in Figure 37 was modeled using the technique by Li and Wang [68]. The current in the channel is given by

$$I_{ds} = W_g q v(x) n_s(x) \tag{32}$$

where W_g is the gate width and $v(x)$ and $n_s(x)$ are the carrier velocity and sheet carrier density, respectfully, at position x in the channel. The expression for the sheet carrier density is given by the self-consistent solution of the 1-D Poisson's and Schrodinger equations

$$n_s = \frac{\varepsilon}{qd}\left(V_{gs} - V_{off} - E_F\right) \tag{33}$$

where n_s is the sheet carrier density in the channel, ε is the permittivity of the $Al_mGa_{1-m}N$ layer given by 9.5-0.5m [66], d is the thickness of the AlGaN layer, q is the electron charge, V_{gs} is the applied gate-to-source bias, V_{off} is the threshold voltage where the device turns off, and E_F is the Fermi level with respect to the GaN layer conduction band. E_F is modeled using the equation $E_F = k_1 + k_2 n_s^{1/2} + k_3 n_s$ where k_1, k_2, and k_3 are calculated for a given temperature using [75]. The nonlinear equations for E_F and n_s are solved simulataneously to solve for these parameters. Voff is given by

$$V_{off}(m) = \phi_b(m) - \Delta E_C(m) - \frac{qN_D d^2}{2\varepsilon(m)} - \frac{\sigma_{pz}(m)d}{\varepsilon(m)} \tag{34}$$

where ϕ_b is the Schottky barrier height, ΔE_C is the conduction band discontinuity at the AlGaN/GaN interface, N_D is the doping concentration of the AlGaN layer (0 for nonintentionally doped AlGaN), and σ_{pz} is the polarization sheet charge density at the interface. For σ_{pz}, we use a nonlinear model that includes the spontaneous and piezoelectric polarization as a function of the aluminum mole fraction of the AlGaN layer [69] .

The electron drift velocity as a function of the electric field is modeled for the drift velocity in both the low-field and velocity-saturation regions as [76]

$$v(E) = \frac{\mu_0 E + v_{sat}\left(\frac{E}{E_T}\right)^4}{1 + \left(\frac{E}{E_T}\right)^4 + a\left(\frac{E}{E_T}\right)} \tag{35}$$

where $v(E)$ is the carrier drift velocity, μ_0 is the low-field carrier mobility, E is the electric field in the channel, v_{sat} is the saturation carrier velocity, E_T is the critical electric field where $v(E_T) = v_{sat}$, and a models the velocity overshoot effect. We model the low field mobility as a function of the gate voltage using the expression from [75]

$$\mu_0 = \frac{p_1}{p_2 + \left(V_{gs} + p_3\right)^2} \tag{36}$$

where p_1, p_2, and p_3 are experimental parameters reported in literature [75].

Analytical expressions for carrier mobility, saturation drift velocity, and energy band offset are implemented to model each of these parameters as a function of temperature [70]. The I-V characteristics are then derived by integrating the channel current along the length of the channel, and applying appropriate boundary conditions to the result in order to obtain two systems of nonlinear equations. Solving these systems of equations gives the drain current for both the low-field and the velocity-saturation regions, which are then combined to give the I-V curve over both regions [68].

$$low{-}field \begin{cases} \frac{I}{\lambda E_T}\left(1 + ae_0 + e_0^4\right) = \left(e_0 + be_0^4\right)\left(V_{gt} - IR_s\right) \\ \frac{I}{\lambda E_T}\left(1 + ae_L + e_L^4\right) = \left(e_L + be_L^4\right)\left(V_{gt} - V_{ds} + IR_d\right) \\ \frac{I}{\lambda E_T}\left(\frac{e_L}{2e_o} - \frac{e_L}{2e_L} + a\left(e_L - e_0\right)\right) = V_g t\left(e_L - e_0\right) + e_0\left(V_{ds} - IR_d\right) - e_L IR_s - e_0 e_L E_T L \end{cases} \tag{37}$$

$$high - field \begin{cases} \frac{I}{\lambda E_T}\left(1 + ae_0 + e_0^4\right) = \left(e_0 + be_0^4\right)\left(V_{gt} - IR_s\right) \\ \frac{I}{\lambda E_T}\left(2 + a\right) = \left(1 + b\right)\left(V_{gt} - V_{L1}\right) \\ \frac{I}{\lambda E_T}\left(\frac{1}{2e_0} - \frac{e_0}{2} + a\left(1 - e_0\right)\right) = V_{gt}\left(1 - e_0\right) + e_0 V_{L1} - IR_s - e_0 E_T L_1 \\ V_{L1} + pE_T sinh\left(\frac{L - L1}{p}\right) = V_{ds} - IR_d \end{cases} \tag{38}$$

The regions are calculated separately to account for the velocity before and after saturation. The low-field region uses the boundary conditions of x=0 at the source end and x=L representing the position of the 2DEG channel in the x-direction where the carrier velocity

becomes saturated. V(0) is taken to be the current times the source resistance, R_s, and V(L) is the current times the drain resistance, R_d, subtracted from the bias applied between the drain and the source from the drain end, $V_d s$. The ratio of electric field to the critical electric field required for velocity saturation of carriers, $E(x)/E_T$, as a function of position x in the channel is represented by e(x), where e_0=e(0) and e_L=e(L). In the high-field region, where carrier velocity is saturated, another voltage, V(L1) is included to represent the difference in voltage where e(x)=1 which corresponds to E(x)=E_T. V_{gt} is the difference between the gate-to-source bias and the threshold voltage. The variable $\lambda = W_g \epsilon \mu_0 d$, and b=$v_{sat}/(\mu_0 E_T)$. A complete list of the equations used to model each of the input parameters, along with their references, is given in Table 6.

Table 6. Relevant equations and parameters for the HEMT charge control model used to determine current-voltage characteristics as a function of temperature

Parameter	Equation Used	Reference
Channel current	$I_{ds} = W_g q \nu(x) n_s(x)$	[68]
Sheet carrier density	$n_s = \frac{\varepsilon}{qd}\left(V_{gs} - V_{off} - E_F\right)$	[68]
AlGaN permittivity	$\varepsilon = 9.5 - 0.5m$	[66]
Fermi level	$E_F = k1 + k_2 n_s^{1/2} + k_3 n_s$	[75]
Threshold voltage	$V_{off}(m) = \phi_b(m) - \Delta E_C(m) - \frac{qN_D d^2}{2\varepsilon(m)} - \frac{\sigma_{pz}(m)d}{\varepsilon(m)}$	[68]
Electron drift velocity	$\nu(E) = \frac{\mu_0 E + \nu_{sat}\left(\frac{E}{E_T}\right)^4}{1+\left(\frac{E}{E_T}\right)^4 + a\left(\frac{E}{E_T}\right)}$	[68]
GaN lattice constant	$a_0 = .31986e - 10$	[69]
AlGaN lattice constant	$a(m) = (.31986 - .00891 * m) * 1e - 10$	[69]
Piezoelectric polarization AlGaN	$P_{pz}^{AlGaN} = m * P_{pz}^{AlN} * \epsilon_b + (1-m) * P_{pz}^{GaN} * \epsilon_b$	[69]
Spontaneous polarization AlGaN	$-0.09 * m - .0034 * (1-m) + .019 * (1-m)$	[69]
Bandgap of AlGaN	$E_g^{AlGaN} = m * E_g^{AlN} + (1-m) * E_g^{GaN} + m * (1-m)$	[70]
Bandgap of GaN	$3.582 - 9.04e - 4 * (T^2/(T+830))$	[70]
Conduction band discontinuity	$0.75 * (E_g^{AlGaN} - E_g^{GaN}))$	[70]
Carrier mobility (25°C)	$\mu_{25C} = \frac{p_1}{p_2 + \left(V_{gs}+p_3\right)^2}$	[75]
Carrier mobility (>25°C)	$\mu_T = \mu_{25C}(\frac{T}{300})^{-1.6}$	[70]

The current-voltage characteristics of the HEMT device is simulated by calculating the drain current for a range of drain and gate biases (Figure 38). This is done in MATLAB using the parameters in Table 7. The simulated HEMT device behaves according to typical experimental and theoretical results, with the drain current increasing with drain voltage in the low-field region and eventually saturating after the carriers reach ν_{sat} [77]. The drain current for a given drain voltage is increased by increasing the gate bias. The simulation

of drain current as a function of gate voltage at various temperatures is shown in Figure 39. The drain current decreases with increasing temperature, which is consistent with the fact that the carrier mobility decreases for higher temperatures [78]. These simulation results verify that the HEMT physics are modeled realistically and yield reasonable device characteristics in our simulations.

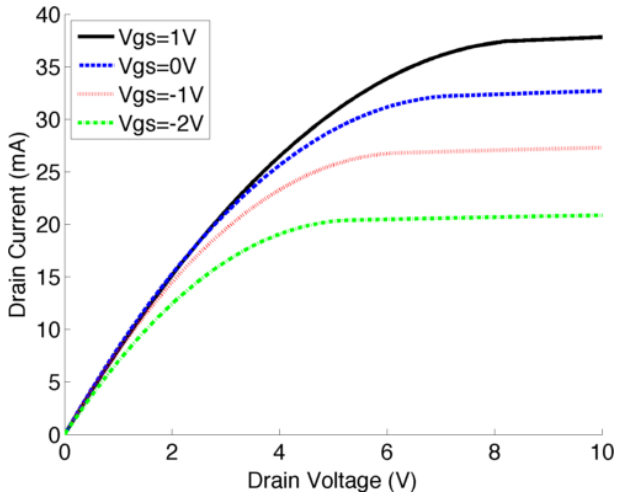

Figure 38. Simulation of AlGaN/GaN HEMT current-voltage characteristics for various gate biases

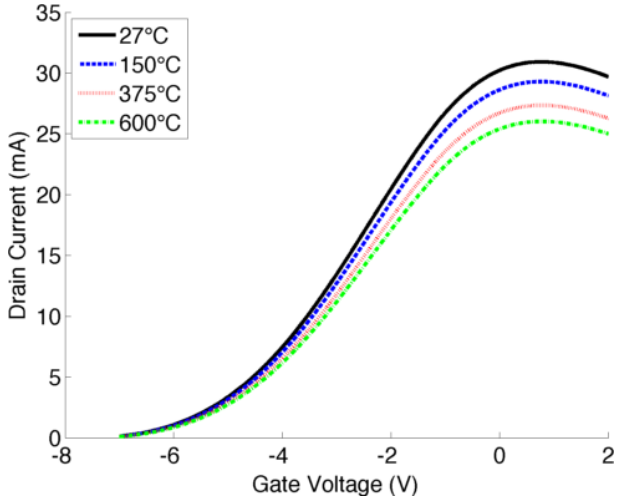

Figure 39. Simulation of AlGaN/GaN HEMT drain current as a function of gate bias for different temperatures

Table 7. Device parameters used in HEMT sensor simulations

Device Parameter	Description	Value
dipole moment	of hydrogen gas	0.2
Lg (μm)	gate length	10
Wg (μm)	gate width	100
Vds (V)	drain-sorce voltage	5V
Vgs (V)	gate-source voltage	0V
K ($torr^{-1/2}$)	equilibrium rate constant	1
$E_T(V/m)$	critical electric field	$150e^5$
vsat (m/s)	velocity saturation	$1.7e^5$
$R_d(\ \Omega)$	parasitic drain resistance	8
$R_s(\ \Omega)$	parasitic source resistace	8
Al mole fraction	of AlGaN layer	0.3
d (nm)	thickness of AlGaN layer	21
$p_1(m^2V/s)$	parameter from [75]	0.84
$p_2(V^2)$	parameter from [75]	21
$p_3(V)$	parameter from [75]	1.8

3.2.3 HEMT sensor response for hydrogen gas

Simulations were implemented to characterize the sensitivity of the sensor as a function of hydrogen concentration for various interface state concentrations (Figure 40). The results show a general increase in both current change and sensitivity for higher hydrogen concentrations, as well as increases in both metrics for increased interface state densities. The measured signal is on the order of a few milliamps for concentrations above 100ppm, and hundreds of microamps between 1-10ppm. While these values are easily detectable using standard characterization equipment, it may be difficult to detect concentrations on the order of ppb using the same circuitry. At these concentration levels, the measured signal may be on the order of nanoamps, which is comparable to the noise level for the system. In this case, a viable option could be to use a lock-in amplifier circuit to isolate the current change upon gas exposure from the noise and amplify it in order to obtain a detectable signal [79].

For the simulated device, we see an increase in current change of 2.2mA as the surface state concentration is increased from $1x10^{13}cm^{-2}$ to $1x10^{15}cm^{-2}$ (Figure 41). This provides

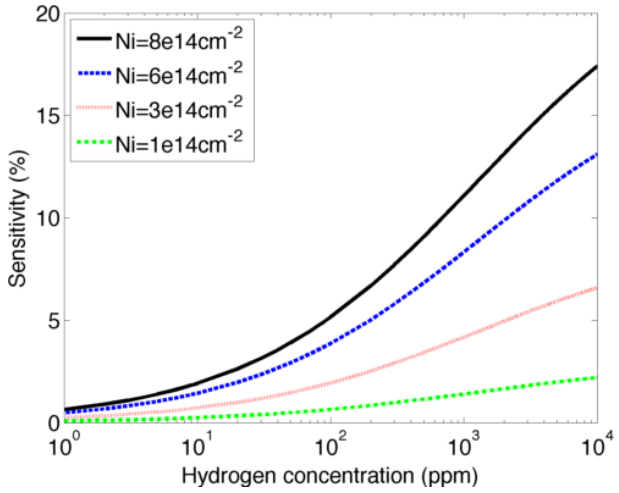

Figure 40. Simulation of the sensitivity of the HEMT sensor for different hydrogen concentrations

a possible explanation for the disparity in previous HEMT sensor measurements. Furthermore, this result provides a method of estimating the interface state concentration if the other parameters are known by matching experimental current change or sensitivity to the simulated results as a function of different interface state densities. Likewise, if information about the interface trap density is known by DLTS or other characterization techniques, information regarding the chemical interactions between the gas and AlGaN surface can be extracted from the model. It should also be noted that the both the sensitivity and current change are proportional to the magnitude of the dipole moment, which is specific to the target gas. One strategy for obtaining complete device selectivity can be achieved by implementing a differential sensor system on a single chip that utilizes different chemical mechanisms that are specific to each gas.

The device sensitivity as a function of the equilibrium rate constant, K. is shown if Figure 42. The simulation shows an increase in sensitivity with an increase in K which is a function of the temperature. This indicates that the temperature effects on the sensor device are dominated by the effects of K rather than the effects of temperature on the semiconductor parameters. In general, K increases with the temperature while the mobility of the HEMT decreases; however the contribution from the equilibrium constant dominates

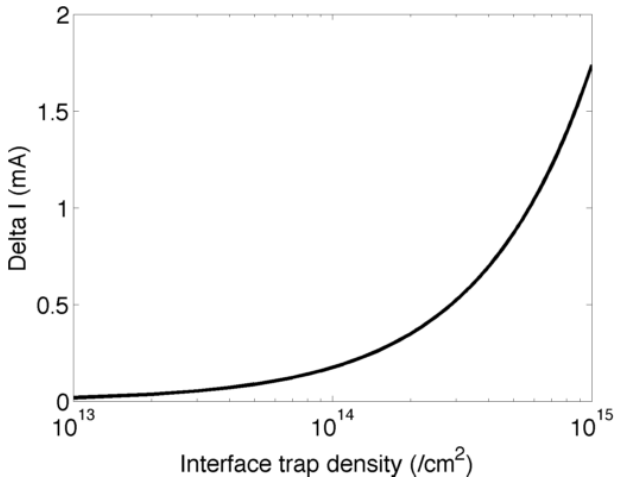

Figure 41. Simulation of the ΔI as a function of interface trap density

the total sensor response in the temperature ranges of interest in this study. At 1000 ppm, the sensitivity begins to saturate at K=78, which corresponds to a temperature of 600°C for the hydrogen/Pt interaction [53]. This closely matches the experimental measurements from Song and Lu. It is also possible for the rate of desorption to be greater than the rate of adsorption after some optimal temperature that depends on the gas. This causes the equilibrium constant to exhibit a decrease at temperatures higher than the optimal temperature, which results in a decrease in ΔI. Indeed, it has been shown in some studies that there is an optimal temperature that depends on both the gas and semiconductor material, but this phenomenon has not been fully modeled or explained from a physics perspective; furthermore, this observation has not yet been utilized. In a later section, we will further analyze this point using our own experimental results and discuss how this phenomenon can be useful as another strategy for obtaining device selectivity between the different gases.

3.3 Optimization of HEMT sensor design using the analytical model

Simulations were carried out using our analytical modeling software in MATLAB for a large range of several device parameters. Using the simulation results, we gain insight into how to design and operate our HEMT sensors for optimal sensor performance. For the purposes of optimization, the simulations are carried out for hydrogen detection. This is

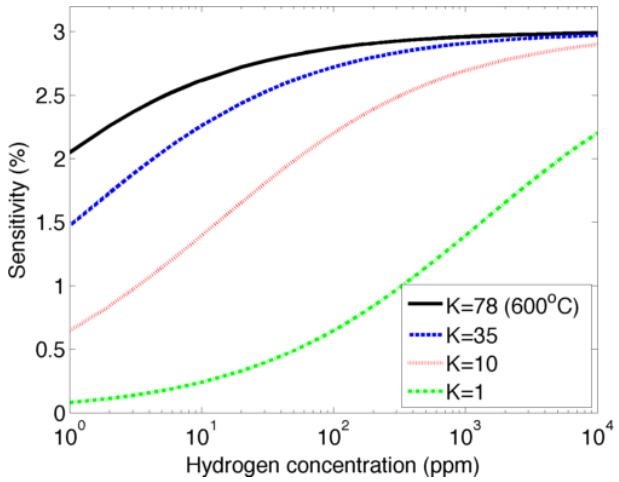

Figure 42. Simulation of the sensitivity of the HEMT sensor as a function of temperature and concentration

because the gas sensing mechanisms for hydrogen are both simpler and better understood, allowing us to make fewer assumptions in our model. In later parts of this chapter, we discuss the modeling of exhaust gases (NO, NO_2, and NH_3) that are less studied and not as well understood; we then extract information regarding different chemical mechanisms by fitting our model to experimental results.

3.3.1 Gate bias

While the voltage change at the Pt/AlGaN interface is caused by the interaction of the gate with the hydrogen gas molecules, it is also possible to apply an additional gate bias to the surface of the gate. This provides a means of tuning the device characteristics in real-time during sensor operation. Simulations of the HEMT sensor sensitivity and absolute current change as a function of the applied gate voltage are shown in Figure 43. From these results, it is apparent that there is an optimal choice for gate bias in terms of maximizing the current change induced by the presence of the target gas and thus reducing the detection limit. For each gas concentration simulated, the current change approaches zero near the negative threshold voltage, increases as the bias is increased until a maximum value at -1.7V, and then decreases again as the bias becomes more positive. This second decrease is associated with the gate voltage that provides the maximum drain current (see Figure 39). This is the

same general trend found in experimental measurements, further supporting the validity of our model [71] . An important observation is that the device sensitivity follows a different trend, where sensitivity is maximized near the threshold voltage and decreases as the bias is increased. For example, for 100ppm hydrogen we see an increase in sensitivity of at least 1 order of magnitude (up to 68% sensitivity) by changing the bias from 2V to -7.2805V, which is 1mV above the threshold voltage for this device configuration. This means that if the device is operated near the threshold voltage, a much higher sensitivity can be achieved at the cost of increasing the detection limit. Therefore, the modulation of gate bias allows for a large adjustable range of sensitivities and detection limits.

Another consideration when applying a bias to the gate is how it will affect the chemical mechanisms regarding the gas adsorption, dissociation, and diffusion on the catalytic sensing area. Localized heating of the gate from an applied bias may also affect the sensing mechanism. As a side note, this heat source may in fact be utilized as method for regenerating the sensor during operation. Since the ΔI is nearly optimal around a 0V gate bias, we choose to use this as an operating point in our first measurements, with the understanding that in during real usage the sensitivity can be adjusted by decreasing the bias.

3.3.2 Gate dimensions

The gate dimensions and material used in a HEMT sensor are important design considerations because the gate directly interacts with the target gas and acts as a catalyst. In order to evaluate the sensor performance for different gate designs, the sensitivity of the HEMT sensor was simulated for various gate lengths while maintaing a constant gate width of 100μm and gate bias of 0V. The results are plotted in Figure 44. From these results, we find that the sensitivity is inversely proportional to the aspect ratio (W_g/L_g), with a decrease in sensitivity of 25% at 1000ppm when the gate length is decreased from 100μm to 2μm). For shorter gate lengths, a higher proportion of the carriers in the 2DEG are above the critical electric field and have saturated velocity, resulting in an increased current over the length of the channel. Since the baseline current is increased, the relative change in

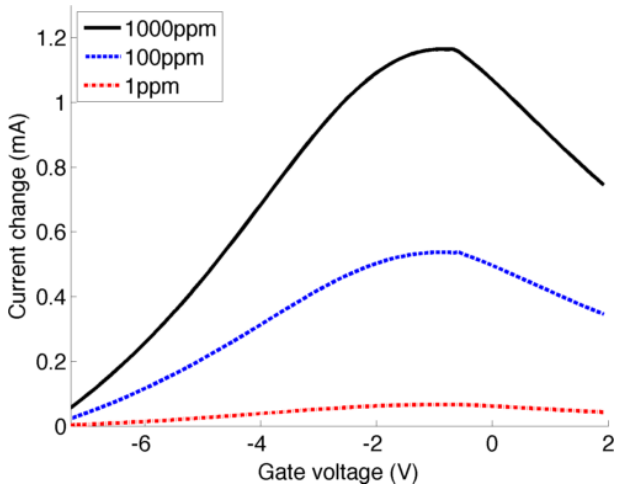

(a)

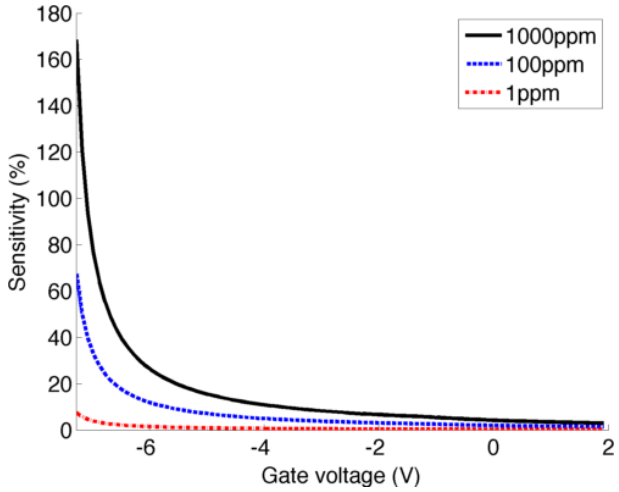

(b)

Figure 43. Simulations of HEMT sensitivity and absolute current change as a function of gate bias

current upon gas exposure is decreased, resulting in the observed decrease in sensitivity. Interestingly, the effect of the gate length on sensitivity is less than than the effect on ΔI. Another design consideration is the effect of bulk traps and defects on the device current. A longer distance between the source and drain provides a higher probability of an electron interacting with traps and may provide issues with the stability of the device. Therefore it may be beneficial to use a smaller gate length so that we have a large ΔI with a small tradeoff in sensitivity. An advantage of our microtechnology approach is that hundreds of devices can be processed on a single semiconductor wafer. In our first mask designs, we

include several different contact designs with several gate dimensions, so that this part of the model can be experimentally verified.

Other design considerations for the gate include the morphology of the gate material (e.g. nanowires, nanoclusters). In this work, we have only considered a thin homogenous Pt-gate, but other studies have shown that utilizing these alternative gate morphologies can enhance the sensing capabilities of the HEMT sensor [80]. We plan to explore this and adapt our model for these gate structures in future work.

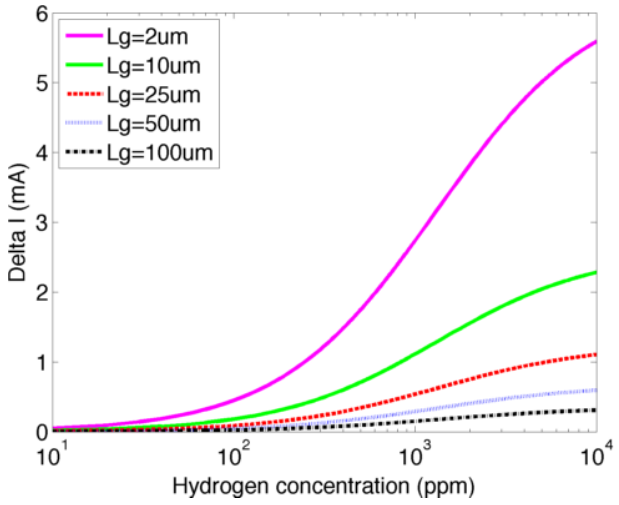

(a)

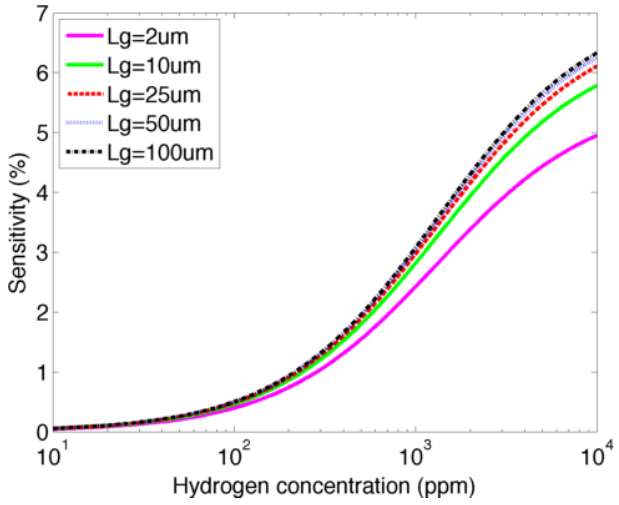

(b)

Figure 44. Simulations of HEMT sensitivity and absolute current change for various gate lengths

In order to further optimize the HEMT sensor sensitivity as a function of both the

gate dimensions and gate bias in parallel, a simulation was carried out by varying the gate dimensions while operating the sensor at a gate bias 1mV above the threshold voltage. The results are plotted in Figure 45. At this gate bias, a maximum sensitivity is obtained for each combination of gate length and width. The measured maximum sensitivity ranges from 68-68.8%, indicating that this device parameter is a relatively stable device measurement relative to the gate dimensions. Accordingly, if the HEMT sensor is operated using the optimal gate bias, the design choice of the gate dimensions does not greatly affect the maximum sensitivity of the device. The implication of this result is that the HEMT sensor is a very robust device, and small errors in the processing of the gate dimensions can be adjusted for by choosing different operating points. This greatly enhances the ability of HEMT sensors to be produced commercially at high throughput.

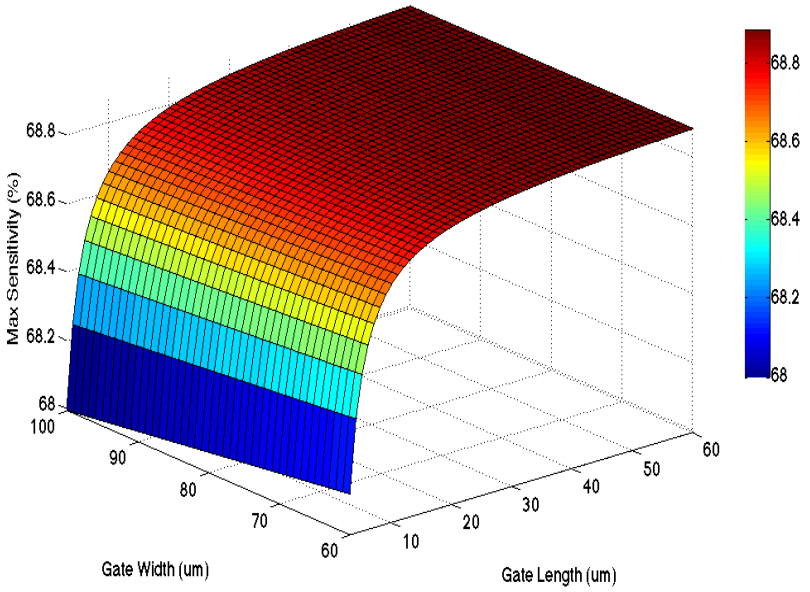

Figure 45. Simulation of the maximized sensitivity (using gate bias tuning) as a function of the AlGaN thickness and the Al composition

3.3.3 Aluminum incorporation and AlGaN thickness

A final design consideration for fabrication of an AlGaN/GaN HEMT sensor is the thickness of the AlGaN layer and the amount of aluminum incorporated in the lattice. The thickness of the AlGaN layer is directly related to the presence and size of the 2DEG. This is due to the polarization induced at the AlGaN/GaN interface that results in a net positive charge at this heterointerface and a net negative charge on the surface. Since it is electrostatically favorable to balance this positive charge as close to the charge layer as possible, as the AlGaN layer thickness increases a negatively charged 2DEG gas forms at the heterointerface and a 2DEG hole gas forms near the surface [66]. Thus, modifying the AlGaN thickness directly changes the effects of the 2DEG as well as the carriers in channel. In addition, the percentage of aluminum used in the AlGaN layer of the HEMT sensor determines the threshold voltage due to polarization effects at the AlGaN/GaN interface from equation 34.

The sensitivity of the HEMT sensor as a function of the aluminum incorporation while operating at a fixed 0V gate bias is shown in Figure 46. The results follow the same general trend as the gate bias modulation, where the sensitivity of the device is inversely proportional to the aluminum content. The sensitivity of the device at 1000ppm hydrogen increases from 4.2% to 11.8% when the aluminum content is decreased from 35% to 15%. The physical explanation for this stems from the fact that a lower aluminum incorporation decreases the initial current of the HEMT, so that the relative change in current is greater when the 2DEG is barely present. In fact, if the HEMT is designed so that the 2DEG is not present in ambient conditions but is turned on due to the presence of the gas, the sensitivity would be infinite. However, the actual current, and therefore the ΔI, measured in this case would be very low, which is seen in our simulation of ΔI with varying aluminum incorporation. We see that the ΔI is optimized at an aluminum incorporation of 20%.

The sensitivity and ΔI of the HEMT sensor as a function of AlGaN thickness is shown

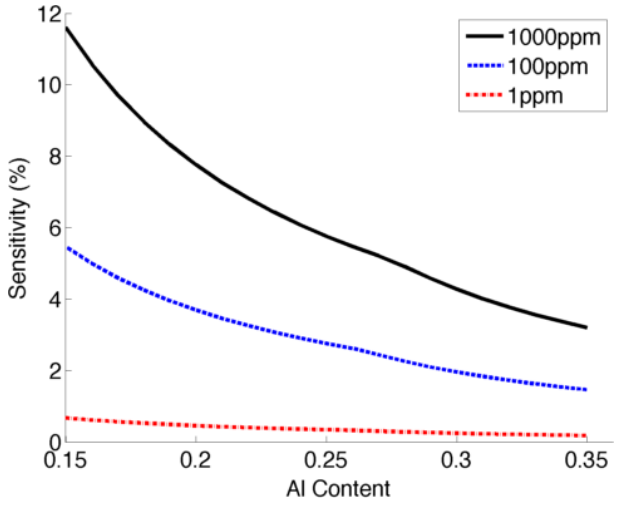

(a)

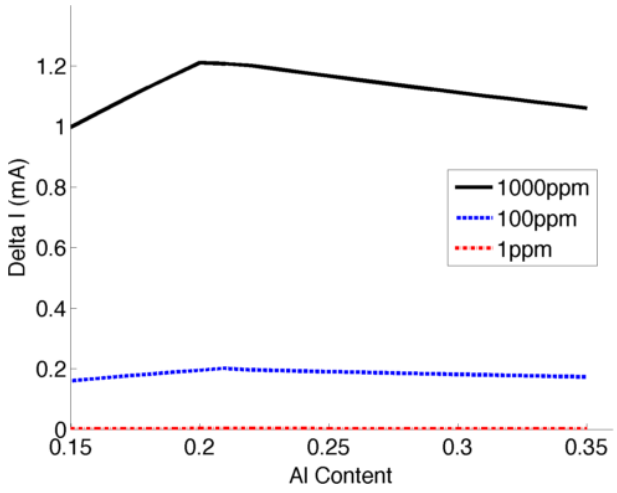

(b)

Figure 46. Simulations of the ΔI and sensitivity of the HEMT sensor as a function of aluminum incorporation in the AlgaN layer

in Figure 47. In both cases, the sensor performance is decreased as the thickness is increased. The explanation of this phenomenon stems from the following phenomenon: once the thickness and accompanying electric field are large enough to place carriers in the quantum well, further increases in the AlGaN thickness do not drastically change the carrier density in the well [81]. Additionally, since the threshold voltage decreases with increased AlGaN thickness and Al content above the critical values, increasing these parameters while operating at a fixed 0V bias is effectively equivalent to increasing the gate bias.

In order to further optimize the HEMT sensor sensitivity as a function of both the AlGaN layer and gate bias in parallel, a simulation was carried out with varying AlGaN thicknesses and aluminum incorporations while operating the sensor at a gate bias 1mV above the threshold voltage. The resulting maximum sensitivity is shown in Figure 48. We observe that the maximum sensitivity again serves as a relatively stable parameter even when using varying combinations of AlGaN thickness and Al content, further demonstrating the robustness of the HEMT sensor design.

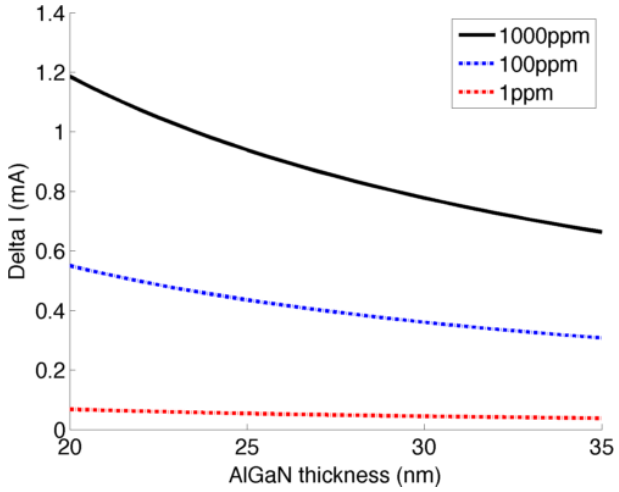

(a)

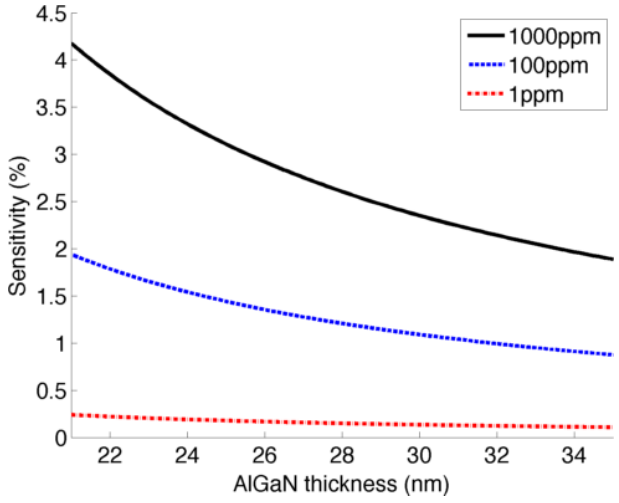

(b)

Figure 47. Simulations of the ΔI and sensitivity of the HEMT sensor as a function of AlGaN thickness

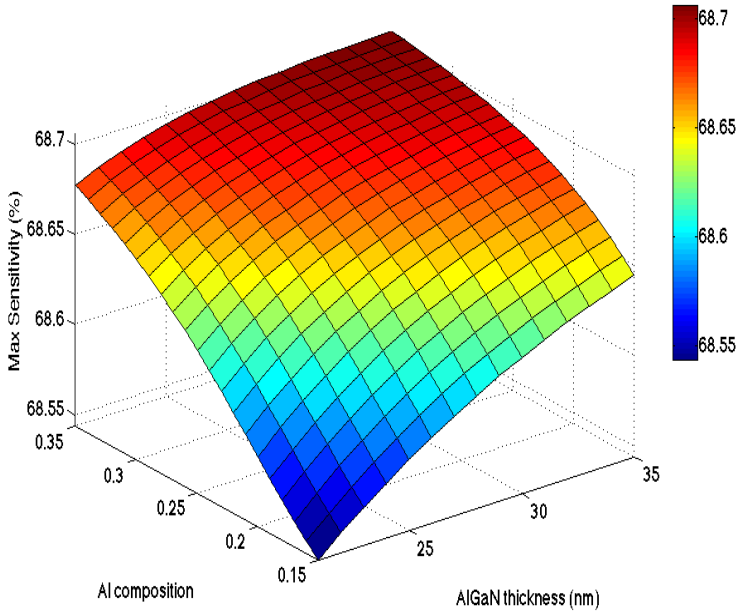

Figure 48. Simulation of the maximized sensitivity (using gate bias tuning) as a function of the AlGaN thickness and the aluminum incorporation

3.4 Device design and fabrication

Based on the optimization results, the AlGaN/GaN HEMT structure was grown according to schematic in Figure 49. Four growths were done in total, with three using the same recipe and one (T1172) using the same recipe but switching the carrier gas from nitrogen to hydrogen. The full list of design parameters is listed in Table 8 along with the results from material characterizations (by SEM, AFM, and XRD).

Table 8. AlGaN/GaN HEMT material characterizations

HEMT Structure	Carrier Gas	V-defect density ($/cm^2$)	RMS	AlGaN thickness	Al %	FWHM
T1172 (on GaN STINS)	H_2	1e6	0.31	20	30	0.4138
T1175 (on GaN STINS)	N_2	1e8	0.77	19	30	0.7928
T1180 (on GaN STINS)	N_2	4e8	0.40	20	30	0.8651
T1192 (on GaN STINS)	N_2	6.4e8	0.60	24	30	0.3251

The devices were grown by MOCVD in a T-shaped reactor using trimethylgallium and ammonia as the gallium, and nitrogen sources, respectively, with nitrogen as the carrier gas. Undoped GaN layers of 200 and 61 nm were grown on an Fe-doped semi-insulating

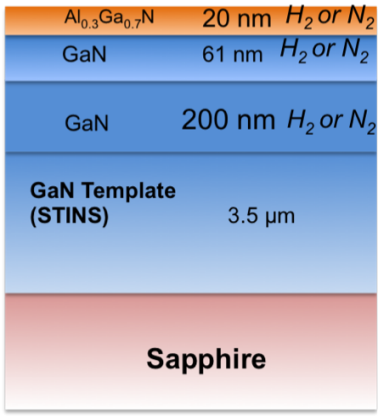

Figure 49. AlGaN/GaN HEMT structures grown at Georgia Tech Lorraine based on the optimizations from HEMT sensor simulations

GaN template on a sapphire substrate, followed by 19nm of AlGaN with an Al composition of 30%, which was verified by XRD measurements. AFM shows an RMS of 0.77nm and V-defect density of $1x10^{8}cm^{-2}$. Mercury probe and C-V characterizations using a probe station showed that a 2DEG is present with a channel concentration of 4e12cm^{-}2 for a 0V gate bias. From the first structures, T1172 and T1175, it was determined that changing the carrier gas from N_2 to H_2 decreased the V-defect density (i.e. better crystal quality), but increased the resistance and caused a loss of the 2DEG.

For device processing, a mask was designed in Layout Editor and purchased from Selba (Figure 50). The first mask, used for T1172, T1180, and T1192, contained a large range of gate dimensions. The mask is comprised of five layers: (1) ohmic contacts, (2) ion implantation to electrically isolate the active areas of the different devices, (3) gate/sensing area, (4) ohmic contact thickening with aluminum and placement of aluminum pads for probe contact, and (5) passivation with SiN_4 over everything except the sensing area. A second mask was used for T1175 and is adapted from a standard HEMT structure (the only difference being that we didn't include the passivation layer) with a small gate length (2x200μm) in order to fully study the effects of gate dimensions on sensing performance. The purpose of including several gate sizes is to optimize this parameter for the next sensor iterations.

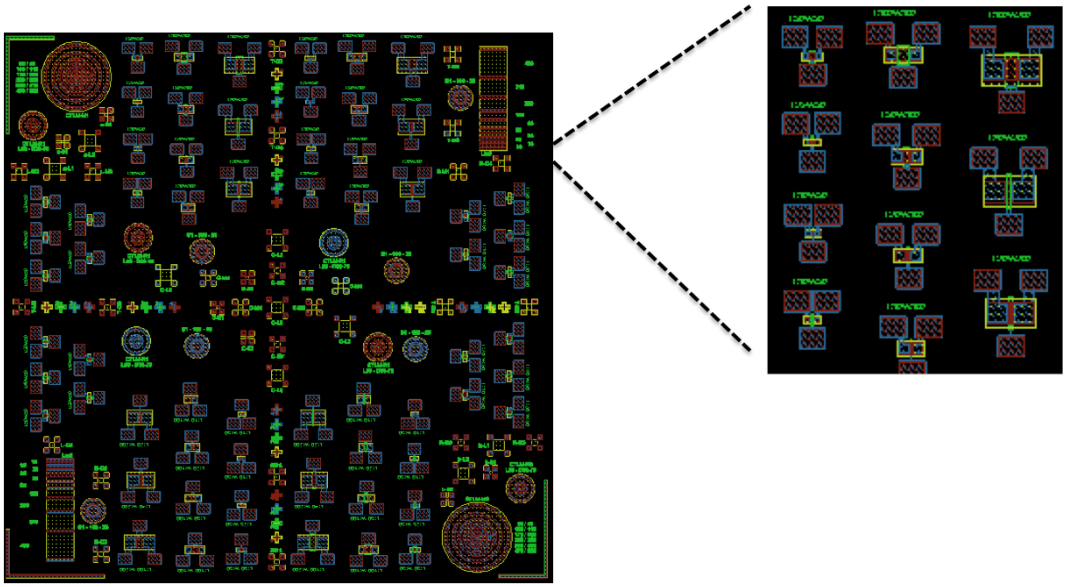

Figure 50. Photolithography mask designed for AlGaN/GaN HEMT sensors; several gate dimensions are included

The devices were processed in the cleanroom at IEMN in Lille, France. For each of the HEMT structures, the ohmic contacts are Ti/Al/Ni/Au (12/200/40/100 nm) deposited by evaporation followed by rapid thermal annealing at 900°C for 30s under N_2, and the gate is a 15nm Pt layer deposited by evaporation. Optical images of the devices processed using the two mask versions are shown in Figure 51, and SEM images showing the source, drain, and functionalized gate sensing areas are shown in Figure 52. For some measurements, gold wire bonding was connected from the source and drain contacts to copper electrodes on a circuit board that was adapted to the Linkam measurement system. This same circuit board configuration was used for the Schottky diode devices in chapter 2.

3.5 Experimental study of NO_2 detection using various gate dimensions

The current-voltage characteristic for three gate dimensions of T1180 at 25°C is shown in Figure 53 . From these measurements, we observe the expected increase in current for shorter gate lengths. According to our model, this should lead to a higher ΔI while the longer gate lengths are expected to have increased sensitivity.

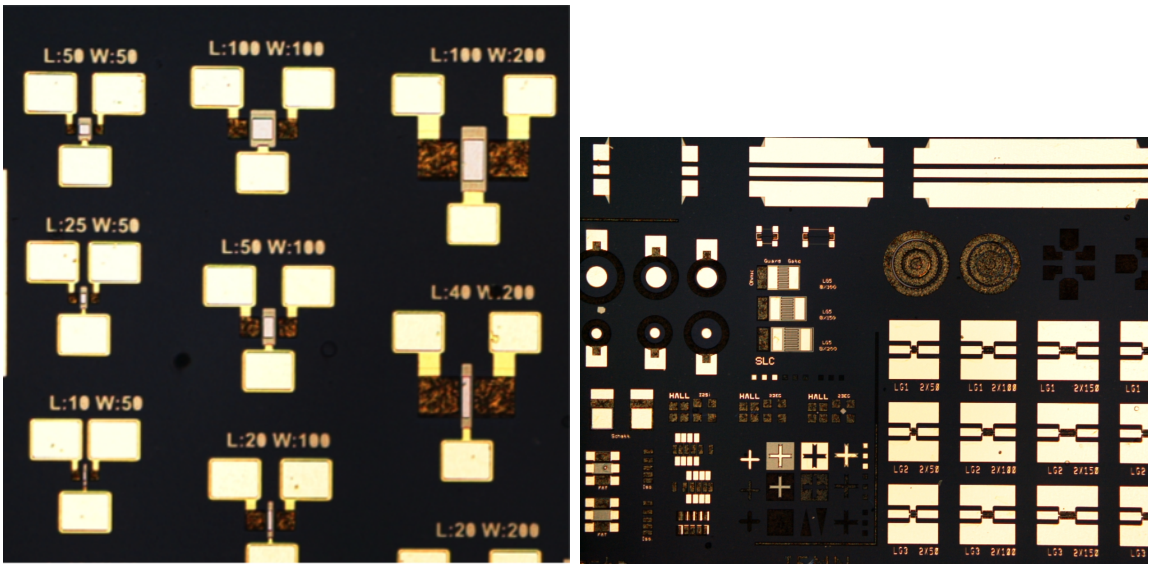

(a) (b)

Figure 51. Optical images of processed HEMT devices using two mask designs

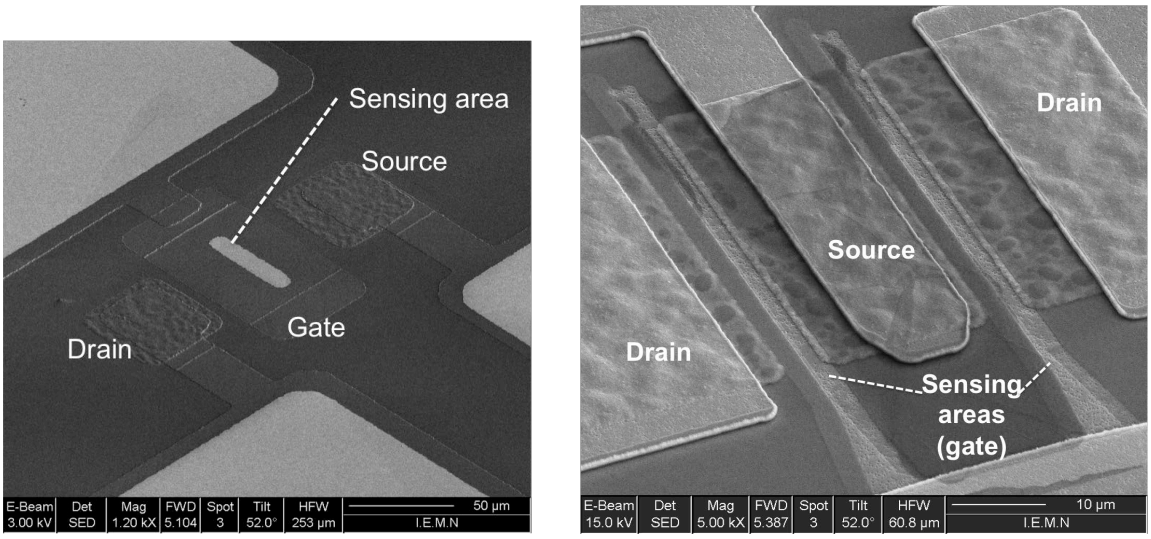

(a) (b)

Figure 52. SEM images of processed HEMT devices using two mask designs, showing the functionalized sensing areas

The same devices were tested at 25°C and 150°C under a 100sccm flux of 450 ppm NO_2 gas using the same methodology and equipment as the BGaN SL double Schottky junction sensors (chapter 2). As seen in Table 9, the correlation between dark current, ΔI, and sensitivity matches what we expect from the model. Additionally, we notice that the 50x50μm gate area gives the largest responsivity, but is not stable at high temperature. From

this study, we can conclude that the 20x200μm gate area gives the best balance between responsivity and thermal stability (Figure 54). Compared to the HEMT sensor reported in literature, we obtain similar performance even at a lower temperature, and thus expect that our HEMT structure should be superior to the reported device at 400°C. We found that the 2x200μm gate area on T1175 provided an even better balance between and stability at higher temperatures. The results of these measurements are shown and discussed in more detail in the next section.

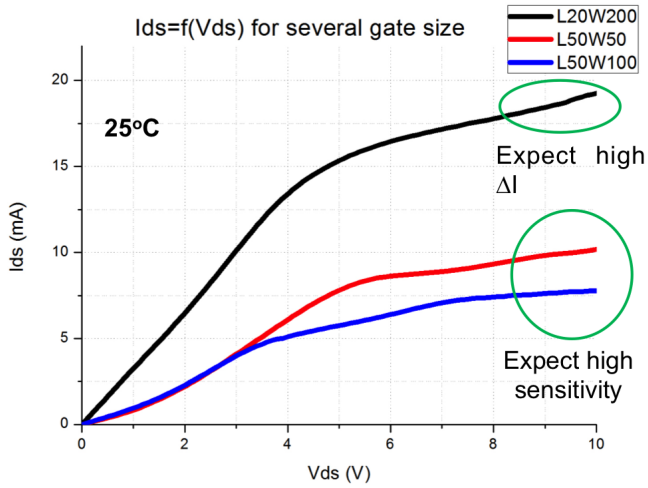

Figure 53. IV curve of T1180 HEMT at room temperature for various gate dimensions

Table 9. HEMT sensor performances in NO_2 gas for various gate dimensions

Gate dimensions (μ m)	I_0 (mA)	ΔI (mA)	S (%)	R (mA/cm^2/ppm)	T (^oC)	Reference
L20 W200	12.1	0.47	3.88	26.1	25	This work
L50 W100	3.94	0.34	8.58	15.1		This work
L50 W50	5.89	0.41	6.99	36.4		This work
L20 W200	6.53	0.63	9.69	35.0	150	This work
L50 W100	2.48	0.07	2.98	3.1		This work
L50 W50	N/A	N/A	N/A	N/A		This work
L70 W500	5	0.5	10	1.43	400	[38]

3.6 Experimental study of NO, NO_2, and NH_3 gas detection for large concentration and temperature ranges

In this section, we report AlGaN/GaN HEMT sensors that have been designed to enable NO detection. We provide in-depth characterization of the sensors operation under a large

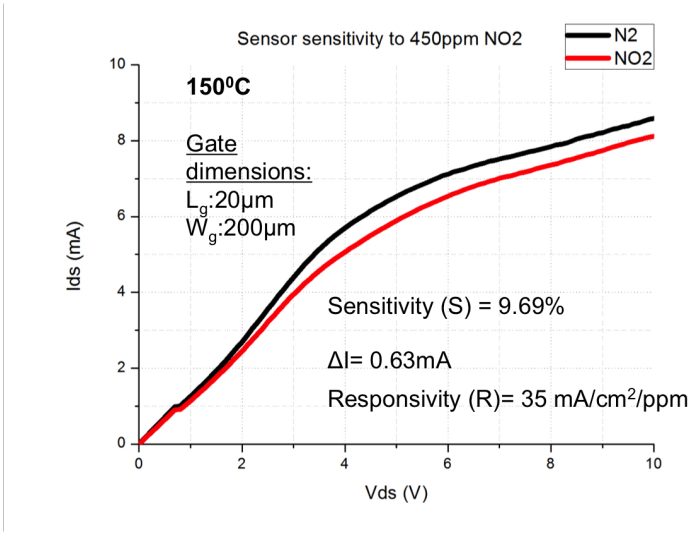

Figure 54. Measurement of T1180 HEMT at 150°C under N2 and 450 ppm N02, showing a sensitivity of 9.69% to NO_2

range of concentrations of NO, NO_2, and NH_3 from 100°C to 400°C and show excellent agreement with analytical models. This level of detailed characterization has not been reported for NO_x or for NH_3 HEMT sensors. Our results show that HEMT sensors possess stability and sensitivity when detecting NO, NO_2, and NH_3 gases even at very low concentrations. We outline the path forward to selective multi-sensor devices. We conclude that it is possible that HEMT sensors may become a key part of diesel anti-pollution systems that are designed to reduce NO and NO_2 pollution, improve fuel efficiency, and meet increasingly stringent regulatory requirements.

The HEMT sensor device was first tested under exposure of various concentrations of NO, NO_2, and NH_3 at 300°C. For each gas, it was determined that the sensor fully regenerated to its initial current under pure N_2 at temperatures greater than 280°C, while at lower temperatures we were only able to obtain a partial reset. We attribute the reset phenomenon to generating sufficient energy to break the chemical bonds that form between the gas ions and the interface traps at the AlGaN surface. We analyze the device performance by examining both the transient and steady state responses of the sensor to each gas. For the transient response, the device is exposed to a constant 100sccm flow of the test gas with

drain and gate biases of 5V and 0V, respectively, until a steady state value is reached, and then reset under pure N_2.

The simulated current-voltage characteristics for this sample are shown in Figure 55. In Figure 56, we can see that the model closely predicts the current change expected upon exposure to 1000ppm NO_2 at 25°C. In this simulation and experiment, we have plotted the steady state value at several drain biases using a 0V gate bias. Although there are some non-linear effects that appear in the experimental measurements that cause a deviation from ideal HEMT characteristics, the gas sensing response matches closely with our experimental observations and thus gives a good prediction for the ΔI and S. We can also use the simulation to extract information about the product of the interface state concentration and dipole moment, which allows us to better understand the chemical reaction occurring between the NO_2 and the interface traps. This is currently being explored and validated with data from deep level transient spectroscopy (DLTS) measurements.

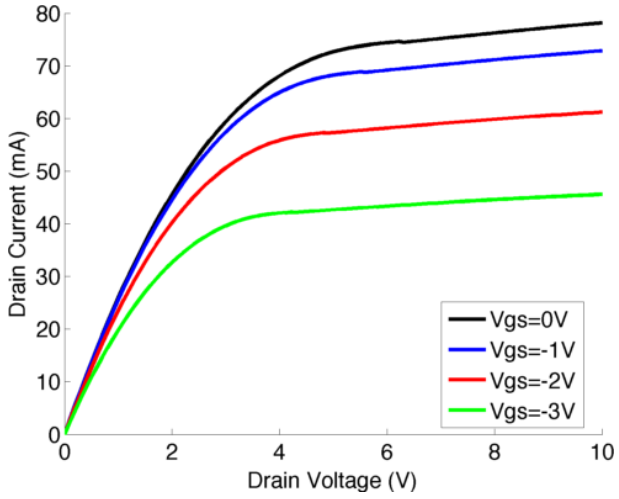

Figure 55. Analytical model of T1175 HEMT IV curve for various gate voltages.

The transient response of the HEMT sensor for 10-800ppm NO_2 was measured at 300°C (Figure 57). The ΔI and S increase as a function of concentration (Figure 57). Even at low concentrations of 10ppm, ΔI and S were found to be 0.35mA and 1.3%, respectively. At concentrations higher than 600ppm, however, we observe some saturation of both ΔI and S, consistent with the results from Schalwig for HEMT devices above 1000ppm. Since the

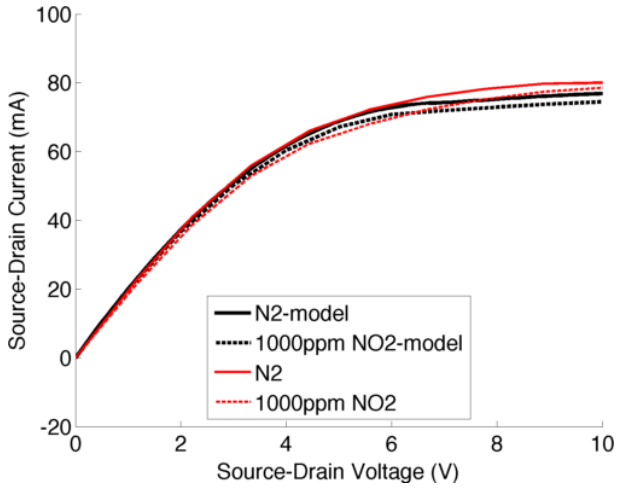

Figure 56. Analytical model of HEMT sensor to 1000ppm NO_2 at 25°C compared to experimental results

saturation phenomenon occurs when the interface coverage is maximized, increasing the concentration of interface traps could solve this issue. This is the first time that this range of concentrations for NO_2 has been studied for HEMT sensors. The transient response for 10ppm NO_2 was also modeled (see inset) by fitting the time constant with the steady state model. This allows us to calculate the adsorption time constant, τ_{ads}, and reaction rate of adsorption, r_{ads}, as 2 min and 0.5 min^{-1}, respectively. The desorption time constant, τ_{des}, and reaction rate of desorption, r_{des}, is calculated to be 2.2min and 0.45 min^{-1}, respectively.

Exposure of the same device to 10-800ppm NO at 300°C showed a ΔI and S that also increases as a function of concentration, with saturation beginning after 700ppm (Figure 58). The ΔI and S is less than that of NO_2, with 0.25mA and 0.85%, respectively, for 10ppm NO. This is the first time that this range of concentrations for NO has been studied for HEMT sensors, and the first time that any significant sensitivity has been reported for any concentration of NO using a HEMT device (Table 10). From the model (see inset) we calculate τ_{ads}=1.1 min, r_{ads}=0.91 min^{-1}, τ_{des}=1.6 min, and r_{des}=0.625 $^{-1}$. We note that the ability of our device to sense NO is likely due to the thin Pt layer compared to previously reported HEMT sensors. This is consistent with the fact that some Schottky sensors with Pt thicknesses less than 20nm have also shown some sensitivity to NO. The difference

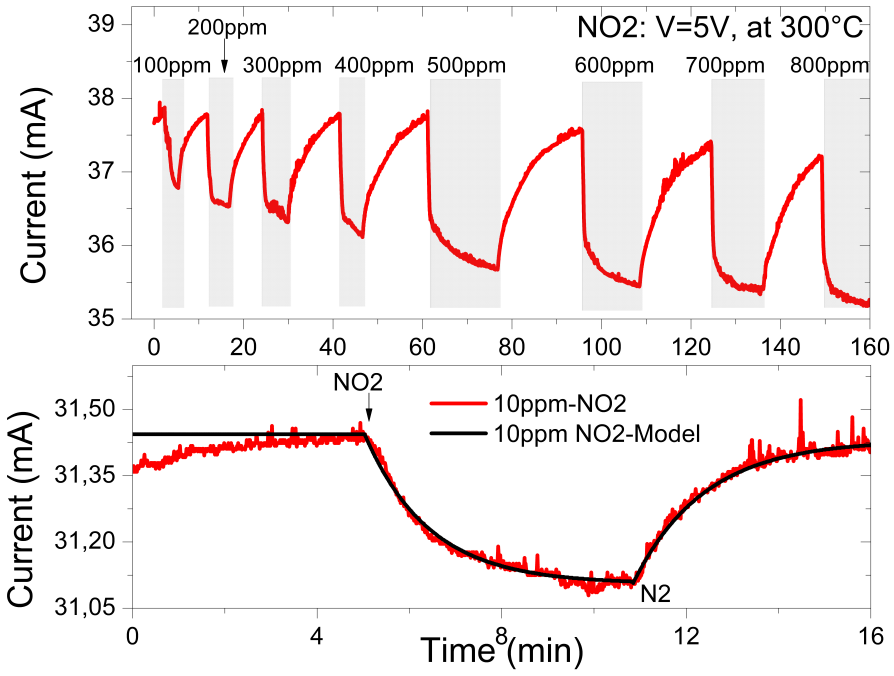

(a)

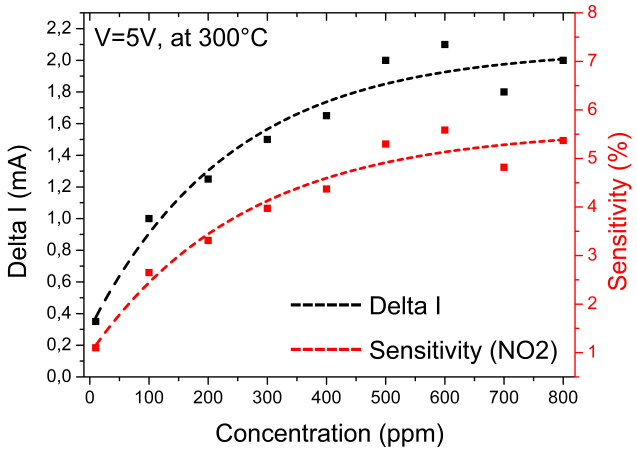

(b)

Figure 57. (a)Transient response of HEMT sensor to 10-800ppm NO_2 at 300°C with 0 gate bias. The grey area indicates the duration of gas exposure, while the white indicates reset under pure N2. The response at 10ppm is compared to the analytical model. (b) ΔI and S of HEMT sensor for 10-800ppm NO_2.

in sensitivity between NO_2 and NO is explained by a difference in detection mechanisms between the two gases. As previously discussed, NO_2 can readily dissociate on the Pt layer into oxygen ions that diffuse through grain boundaries to the AlGaN surface. NO, on the

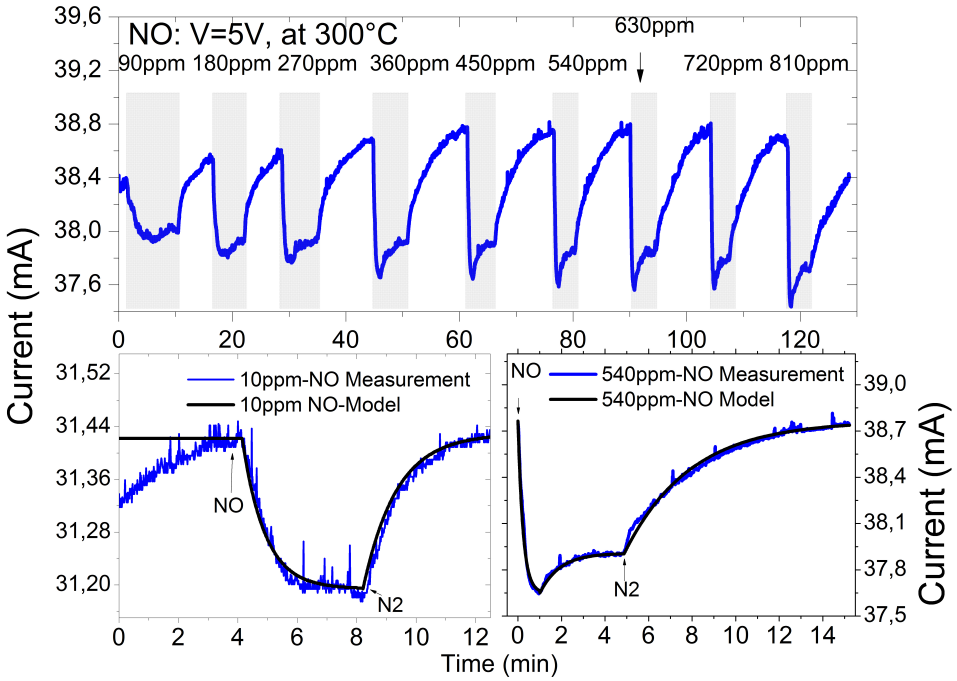

(a)

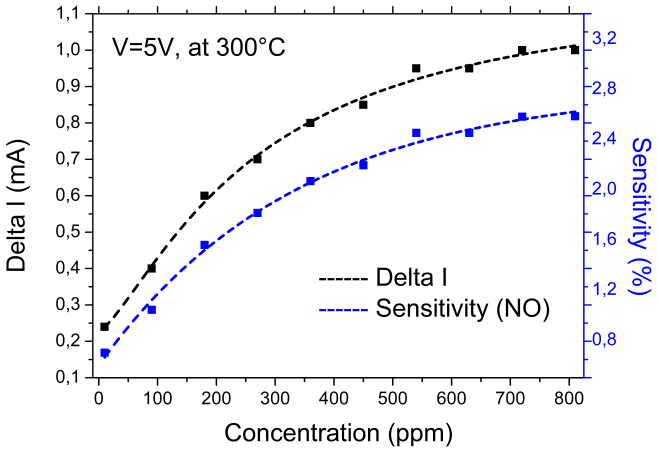

(b)

Figure 58. (a)Transient response of HEMT sensor to 10-800ppm NO at 300°C with 0 gate bias. The grey area indicates the duration of gas exposure, while the white indicates reset under pure N2. The response at 10ppm is compared to the analytical model. (b) ΔI and S of HEMT sensor for 10-800ppm NO.

other hand, does not readily dissociate into oxygen ions; instead, the NO gas molecules must interact directly with traps either at the AlGaN surface or capacitively through pores in the Pt layer. Information regarding the chemical reactions between NO and the AlGaN

Table 10. Updated comparison (with our results) of NO_2, NO, and NH_3 sensor performances, including sensitivity (S), responsivity (R), response time (τ_r) and recovery time (τ_R).

Gas	Device	Catalyzer	I_0 (mA)	ΔI (μA)	S (%)	R ($\frac{mA}{cm^2*ppm}$)	C ppm	T (C)	τ_r/τ_R (s)	Ref.
NO_2	SiC Schottky Diode	20-40nm Pt	0.02	3.8	19.35	0.002	200	300	90/120	[33]
	SNO_2 Schottky Diode	-	0.42	243	58.3	648	0.1	150	43/37	[39]
	GaN Schottky Diode	Pd/ZnO	4.5	860	19.1	2.74	10-100	250	60/120	[42]
	GaN Schottky Diode	**20nm Pt**	**11.5**	**370**	**3.2**	**1.14**	450	**200**	**300/300**	**this work (Ch. 2)**
	BGaN SL MSM	**100nm Pt**	**7.07**	**2140**	**30**	**6.7**	450	**250**	**5/80**	**this work (Ch. 2)**
	AlGaN/GaN HEMT	Pt	5	500	10	1.43	1000	400	n/a	[34]
	AlGaN/GaN HEMT	**15 nm Pt**	**16.5**	**2800**	**17**	**1556**	**450**	**400**	**540**	**this work**
	AlGaN/GaN HEMT	**15 nm Pt**	**35**	**350**	**1**	**8750**	**10**	**300**	**180/300**	**this work**
NO	SiC Schottky Diode	20-40nm Pt	0.108	10	9.26	0.03	40	400	188/99	[33]
	GaN Schottky Diode	Pd/ZnO	4.5	160	3.56	0.51	10-100	250	60/120	[42]
	AlGaN/GaN HEMT	Pt	5	negligible	negligible	negligible	1000	400	n/a	[34]
	AlGaN/GaN HEMT	**15 nm Pt**	**11.4**	**800**	**7**	**444**	**800**	**400**	**n/a**	**this work**
	AlGaN/GaN HEMT	**15 nm Pt**	**35.7**	**250**	**.7**	**6250**	**10**	**400**	**480/**	**this work**
NH_3	AlGaN/GaN Schottky	20nm Pt	nA range	nA range	3000	1.4e-8	35	70	600/900	[41]
	AlGaN/GaN Schottky	10nm Pt	21.5	640	2.98	18286	35	30	n/a	[43]
	AlGaN/GaN HEMT	**15nm Pt**	**45**	**320**	**0.7**	**5333**	**15**	**300**	**15/30**	**this work**
	AlGaN/GaN HEMT	**15nm Pt**	**45**	**90**	**0.2**	**150000**	**0.15**	**300**	**25/36**	**this work**

interface traps can be extracted from the transient response curves. First, we note that for 10ppm NO, the current under gas flow decreases until steady state, corresponding to a negative surface potential at the Pt/AlGaN interface. At higher concentrations, we observe an initial decrease followed by an increase in current after a given time, which we attribute to a second reaction mechanism with a different time response. As the concentration of NO is increased, the second reaction mechanism corresponding to a positive surface potential seems to saturate in magnitude faster than the initial negative peak, and so the overall sensitivity increases.

The same experiment was repeated for exposure to NH_3 gas using the same device, with concentrations ranging from 150ppb to 15ppm (Figure 59). We report a ΔI and S of 0.1mA and 0.2%, respectively, for 150ppb NH_3. Previously, the lowest reported NH_3 concentration measured using either Schottky or HEMT sensor devices was 35ppm. Interestingly, ΔI and S reach a maximum at 3ppm and follow a subsequent decrease as a function of increasing concentration. This is linked to the change in reaction mechanism that begins at 2ppm. At concentrations lower than 2ppm, the signal upon gas exposure decreases until steady state as with NO_2 and low concentrations of NO. At 2ppm, we observe an initial negative peak followed by an increase in signal until steady state is reached, as with higher concentrations

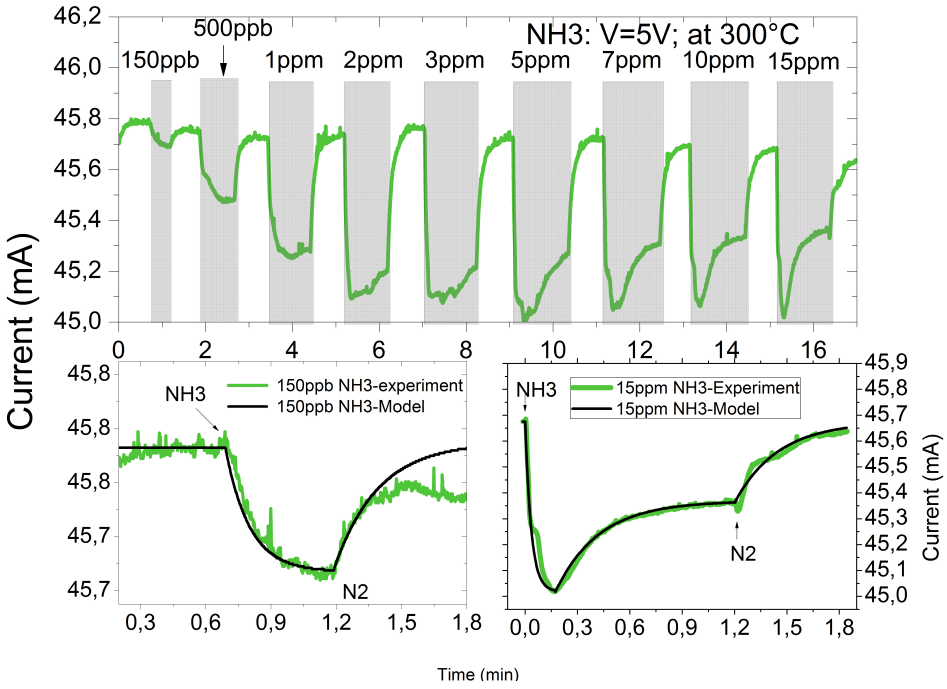

(a)

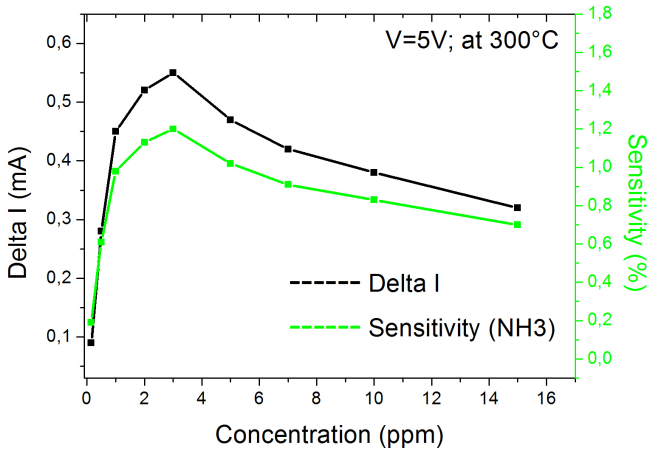

(b)

Figure 59. (a)Transient response of HEMT sensor to 150ppb-15ppm NH_3 at 300°C with 0 gate bias. The grey area indicates the duration of gas exposure, while the white indicates reset under pure N2. The response at 150ppb is compared to the analytical model. (b) ΔI and S of HEMT sensor for 150ppb-15ppm NH_3.

of NO. However, unlike the NO response, as the concentration is increased, the first negative mechanism saturates and the second positive mechanism becomes more dominant.

It is predicted that at higher concentrations the second reaction mechanism corresponding to a current increase will dominate the total response and the sensor will follow the trends previously reported. We attribute the observation of multiple reaction mechanisms to the interaction of each gas with several types of interface traps, with some interactions being more favorable depending on the gas ions or reaction intermediates that are a function of the concentration. Similar responses have been reported for semiconductor-based devices, but have not yet been fully explored or characterized. The different mechanisms and responses for each gas as a function of concentration provides a viable pathway for completely selective devices, which will be further explored.

The response and recovery times were measured using the transient measurements and analyzed as a function of concentration (Figure 60). For NO_2, we observe an increasing response time increases with concentration while for NO we observe the opposite trend. This is attributed to the different mechanism of detection for the two gases. Since NO interacts directly with traps via pores, the response time is faster compared to NO_2 which must first dissociate and then diffuse ions to the interface. Additionally, there may be a larger number of trap types that NO_2 can interact with, which would explain both the higher sensitivity and longer time to reach steady state compared to NO. The response time for NH_3 as a function of concentration exhibits a third, separate trend where the response time increases until 5ppm and subsequently decreases. This is linked with the addition of the second reaction mechanism discussed previously, and follows the same trend as the ΔI and S as a function of concentration. For each gas, the response time is comparable to other HEMT and Schottky-based sensors reported in literature. The different behaviors in response time as a function of concentration provide another pathway for obtaining completely selective devices. For example, in a mixture of exhaust gases it may be possible to extract information about each gas from the response time of different reaction mechanisms in addition to the ΔI and S. For each gas, the recovery time was found to increase with concentration. This is logical, since a higher concentration of adsorbed gas species will require more time

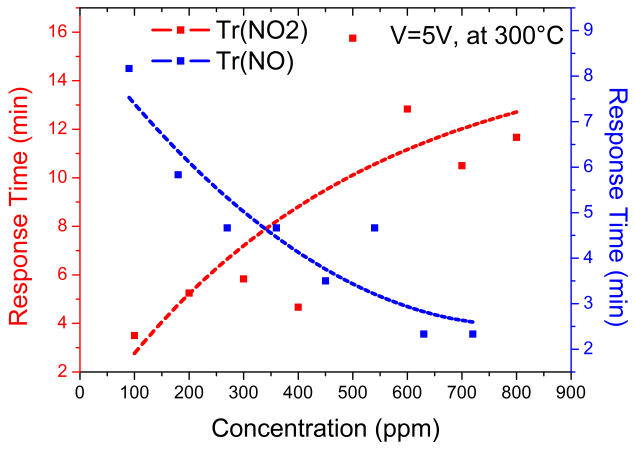

(a)

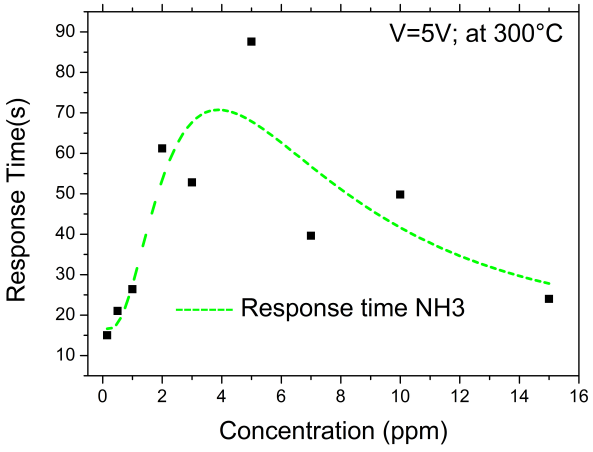

(b)

Figure 60. (a) 10-90% response time of 10-800ppm NO and NO_2 at 300°C with 0V gate bias (b)10-90% response time of 15ppb-15ppm NH_3 at 300°C with 0V gate bias.

to completely free all of the interface traps.

To understand how temperature affects the device performance of the HEMT sensor, ΔI and S was measured from 100-400°C using an intermediate concentration of 450ppm for NO_2 and NO and 15ppm for NH_3 (Figure 61). For NO_2, we observe a gradual increase in performance as a function of temperature from 100-300°C followed by a rapid increase up to 400°C. This is attributed to enhanced dissociation of NO_2 and diffusion of oxygen ions at temperatures greater than 300°C. At 400°C, we observe a high sensitivity of 18%, which is

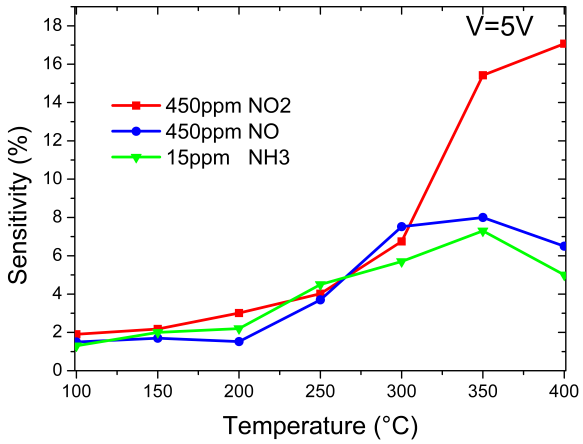

(a)

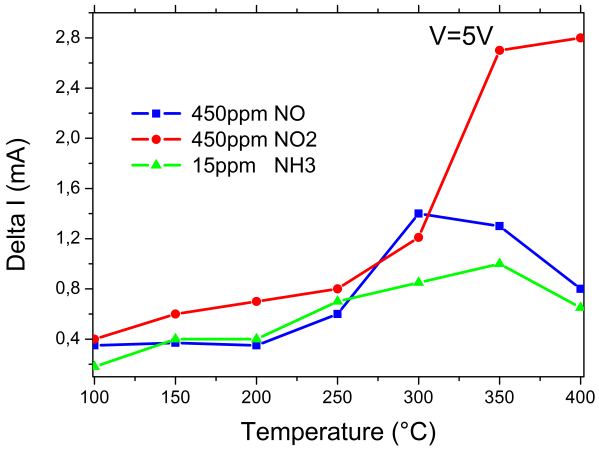

(b)

Figure 61. (a) Sensitivity of 450ppm NO and NO_2 and 15ppm NH_3 from 100-400°C with 0V gate bias (b)ΔI 450ppm NO and NO_2 and 15ppm NH_3 from 100-400°C with 0V gate bias

much larger than the reported value of 10% for 1000ppm NO_2 at the same temperature. NO exhibits lower ΔI and S than NO_2 and reaches peak performance at 300°C, followed by a decrease in both metrics. NH_3 behaves similarly, with a peak performance at 350°C. It was found that both the response and recovery times decreased with increasing temperature. The observation of different optimal temperatures may be useful for device selectivity. For example, a commercial device can operate different sensors at different temperatures in order to exclude the response of one or more gases, and to extract specific concentration

information from a mixture of exhaust gases.

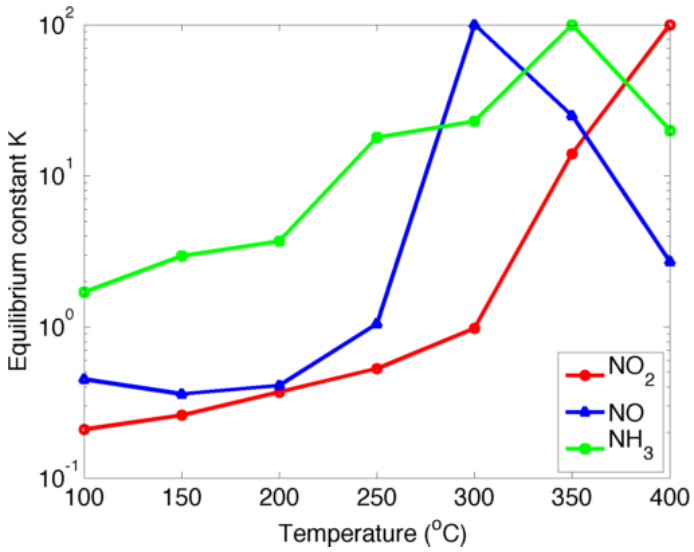

Figure 62. Equilibrium constant, K, for each gas as a function of temperature. The values were extracted from the experimental data using our analytical model, and show the optimal temperature for each gas.

Using our analytical model, the values for the dipole moment and equilibrium constant, K, can be extracted from our experimental curves for ΔI as a function of temperature for each gas (Figure 62). In the model we assume an interface trap density of 3e14cm^{-2}. Since we know the saturation maximum coverage for each gas at its optimal temperature from our experimental data, we fit the dipole moment to the observed ΔI value using K=100 as the threshold for saturated coverage. Higher values of K approach the limit of 1 for the coverage term, and it was found in our model that K=100 always gives a coverage value above 98% of the maximum coverage. Using this method, we obtain net dipole moments of 0.52D, 0.24D, and 0.19D for NO_2, NO, and NH_3, respectively. This gives insight into the strength of the chemisorption between each gas ion and the surface states at the AlGaN interfaceIt is interesting to note that the dipole moment for the NH_3/AlGaN interaction, which likely utilizes a hydrogen dipole layer, is close to the reported value of dipole moment of 0.2D for hydrogen detection using AlGaN/GaN HEMTs [53]. The values of K were then found for each gas as a function of temperature using the analytical model described in Section 2. For NO_2 and NO we calculate K values less than 1 for temperatures

below 300°C and 200°C, respectively. This corresponds to a regime where the desorption constant is greater than the adsorption constant, and explains the relatively small response at these temperatures and large increase in ΔI at temperatures higher than this threshold. For NH_3, on the other hand, the value of K is always greater than 1 which explains why we see a nearly linear increase in ΔI until the optimal temperature of 350°C.

In this section, we have designed, fabricated, and characterized Pt/AlGaN/GaN HEMT sensors for the detection of NO, NO_2, and NH_3 gases. For NO and NO_2, we have shown high ΔI and S for a range of 10-800ppm. This is the first time that significant response to NO has been realized using a HEMT device, and the first time that this concentration range has been fully studied. The transient and steady state responses show an excellent match to our model and allow us to extract some of the parameters related to the chemical mechanisms. The device also showed high sensitivity to NH_3 over a range of 150ppb-15ppm, which are the lowest concentrations studied using either HEMT or Schottky devices. For NO and NH_3, we observe multiple chemical reactions from the transient response. This is shown in the vastly different behavior of the response time as a function of concentration for each gas. We have also shown that the gases behave differently as a function of temperature, with each gas having a certain optimal temperature. The combination of these sensor properties could be exploited to obtain completely selective devices, which could be used to improve diesel automotive exhaust systems.

3.7 CO_2 and N_2O detection

The majority of the work presented so far focuses on detection of NO_2, NO, and NH_3 exhaust gases for the development of next generation sensors to be used in SCR systems. However, as was mentioned in Chapter 1, there are many more pollutants that are emitted from the exhaust that are hazardous to the environment. CO_2, for example, is released from the burning of carbon-based fuels and makes up a large proportion of the greenhouse gases in the atmosphere, which is a major contributor to global warming.

The HEMT sensor used in the previous section, T1175, was tested for the detection of CO_2 gas from a mixture of exhaust gases using the same procedure described in section 6 of this chapter. The composition of the gas mixture was 99.23% CO_2, 0.4% O2, 0.26% CO, 0.08% NO_2, and 0.04% C_3H_8 (methane). The response of the sensor at 300°C is shown in Figure 63.

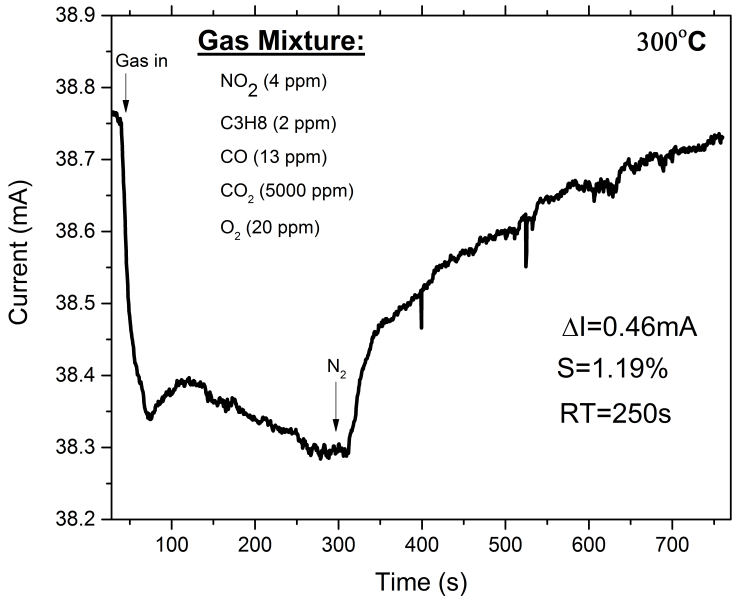

Figure 63. HEMT sensor response to 5000ppm CO_2 in a mixture of exhaust gases at 300°C

The sensor has a ΔI of 0.46mA and sensitivity of 1.19% to the gas mixture. Similar to the previous gas mixtures, we observe the presence of multiple reaction mechanisms. Initially we see a decrease, followed by an increase and then a second decrease in current. The response of the signal resembles the response observed for the mixture of NO_2 and NO, with the difference being that the second decreasing mechanism appears to be more dominant than the increasing mechanism. We speculate that the increase is due to CO since it has a similar molecular structure to NO, and that the dominant decreasing mechanism is primarily due to the high concentration of CO_2 in the mixture. The response and recovery times were 250 and 455 seconds, respectively. This response time is relatively fast

compared to high concentrations of NO_2.

Another measurement was taken using the same sensor to record the HEMT sensor response to 450ppm N_2O at 300°C (Figure 64). A ΔI and sensitivity of 0.13mA and 0.33%, respectively, was recorded for the device. We observe two reaction mechanisms that resembles the mechanisms found for NO detection, with an initial decreasing peak followed by an increase until steady state. This is likely due to a dissociation of N_20 into NO on the Pt surface. This is further supported by the fact that response time for the two gases are nearly the same at this concentration and temperature (180 seconds for N_20 and 200 seconds for NO).

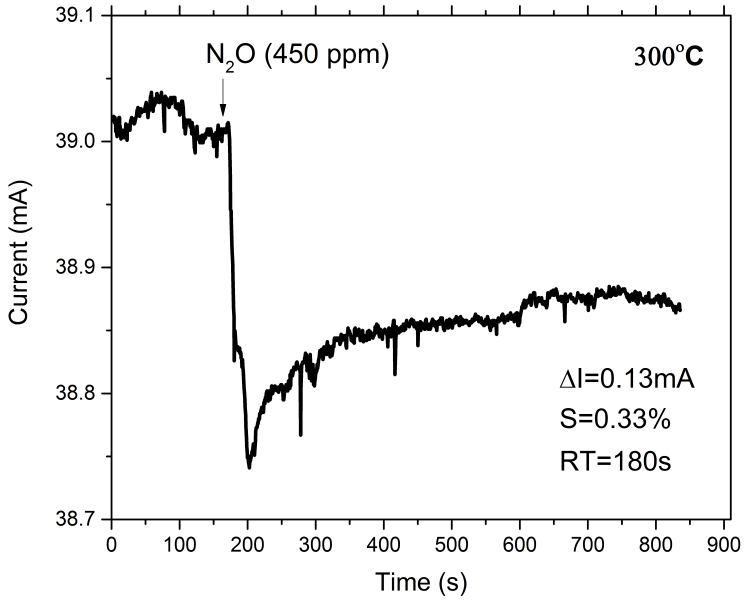

Figure 64. HEMT sensor response to 450ppm N_2O at 300°C

The results presented in this section show that HEMT sensors are capable of detecting a wide range of gas species and are promising options for gas sensors for many different applications. We also note that gas species with similar molecular compositions show similar detection mechanisms. This means that once complete selectivity is obtained for some gases, it should be translatable to other HEMT devices as well. Therefore the groundwork

laid out in this thesis for selective gas sensing is not limited to the gases we have studied, but rather may be transferrable to a large number of gas detection applications by only slightly modifying the designs of the functional layers.

3.8 Thermal fatigue test and long-term device stability measurements

3.8.1 Thermal fatigue test

For development of commercial sensors, it is important to know the physical limitations of the HEMT sensor devices. For example, it is useful to know at which temperature the device shows physical degradation and stops functioning as a sensor. This information is specifically useful for the packaging designs of the devices. In this study, we subject the sensor to various temperatures ranging from 25-900°C for 30 minutes and analyze the morphology changes of the different contacts and the electrical characteristics after each exposure. This was performed in a Linkam measurement system that allowed temperatures up to 1100°C, but did not allow for electrical measurements. Therefore, all of our electrical measurements were taken at room temperature once the device was removed from the high temperature environment. The different contacts examined are the aluminum pad, the ohmic contacts (gold on top), and the Pt gate (Figure 65).

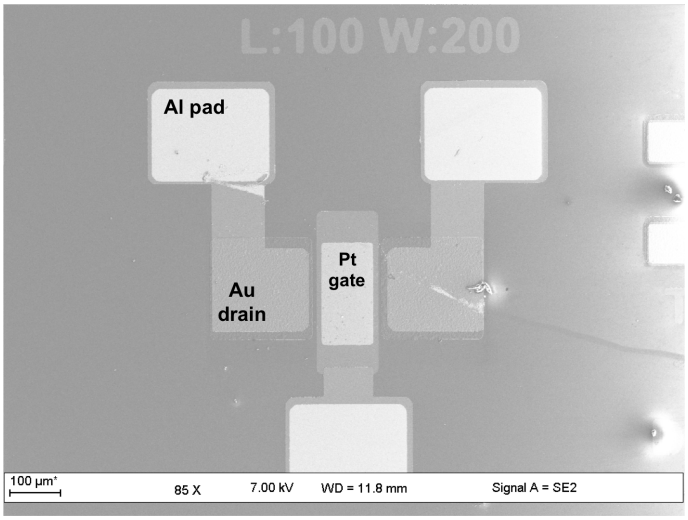

Figure 65. SEM image showing the Al pad, Au source/drain, and Pt gate analyzed in the thermal fatigue test

The progression of the thermal damage to the aluminum pads with temperature is shown in Figure 66. No changes were noticed until after 300°C; after this temperature we begin to see separation of the aluminum into discontinuous clusters. The connection between the pads and ohmic contacts became cracked and electrically disconnected at temperatures higher than 400°C due to a difference in thermal expansion between the different layers. The melting of the aluminum at temperatures higher than its melting point (660.3°C) is clearly shown in Figure 66c and d. In our first design, we chose aluminum as the material for the pads because it is less expensive than the other available materials. Based on this analysis, it would be better for a commercial device to use a metal with a higher melting point, such as tungsten. It should also be noted that the pads were put in place to allow experimental testing with probes in the Linkam measurements system. In a packaged device, the pads may not be necessary at all, as wire bonding can be placed directly from the ohmic contacts to larger electrodes on a circuit board that is protected from the high temperatures.

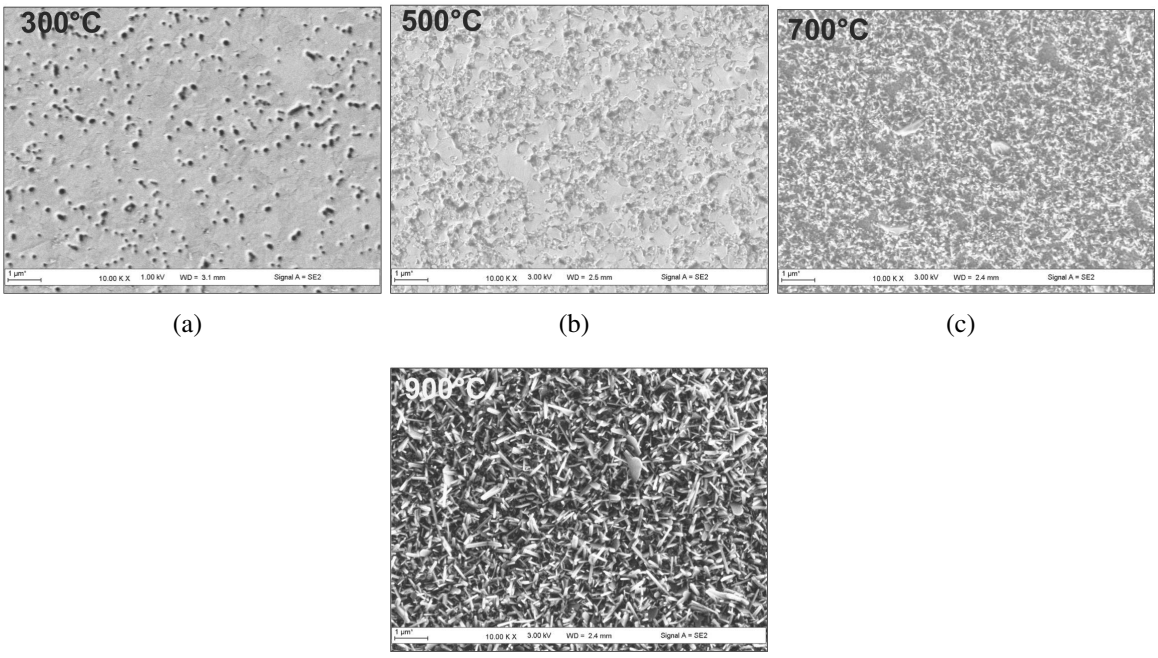

Figure 66. SEM images of the structural integrity and morphology of the aluminum pads at different temperatures

The progression of the ohmic contacts with increasing temperature is shown in Figure 67). Minimal damage damage is observed at temperatures lower than 700°C. At this temperature, we observe cracks beginning to form in the gold layer due to a difference in thermal expansion between the gold and underlying aluminum layer (Figure 67b. At 800°C, the gold begins to separate and form clusters, and we see folding of the gold layer (Figure 67d).

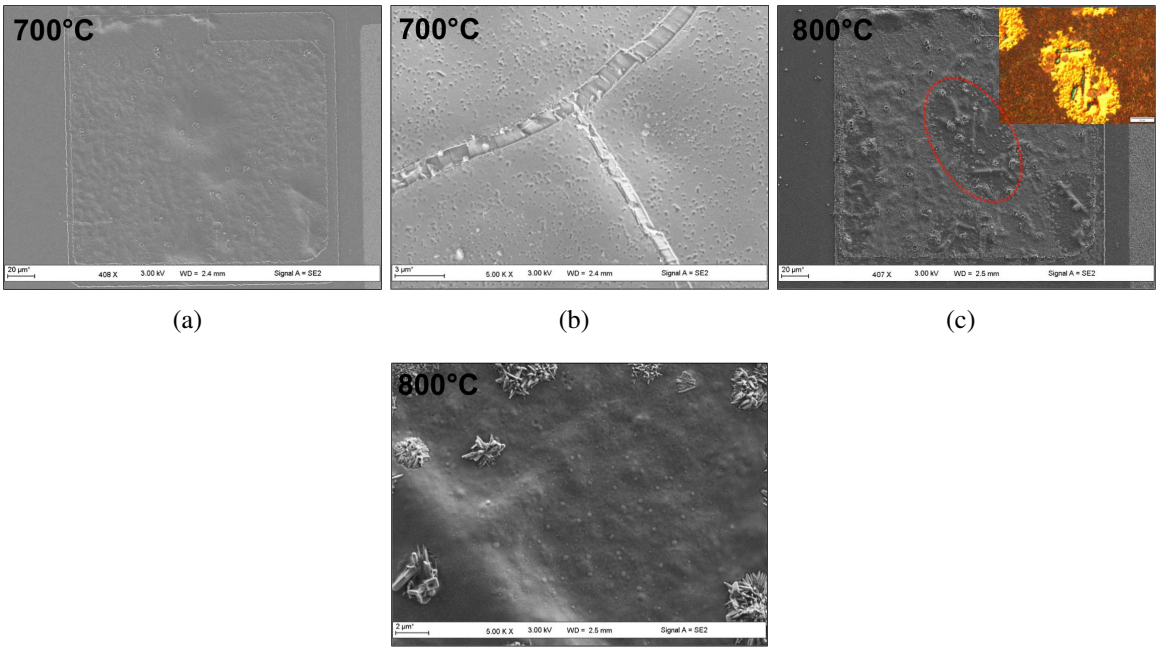

(a) (b) (c)

(d)

Figure 67. SEM images of the structural integrity and morphology of the ohmic contacts at different temperatures

Finally, and perhaps most importantly, we observe the morphology changes of the Pt sensing layer as a function of temperature (Figure 68). Minimal damage or morphological changes are observed below 500°C. At temperatures above 500°C, the Pt layer begins to separate and form clusters (Figure 68a). The gate continues to be functional up to 800°C, but with severe morphological changes (Figure 68d). At 900°C (Figure 68e), most of the Pt is separated and no longer forms a functional gate.

A separate fatigue test was performed on a different piece of the same sample at the University of Lorraine in Nancy, France. This test was performed in a probe station that

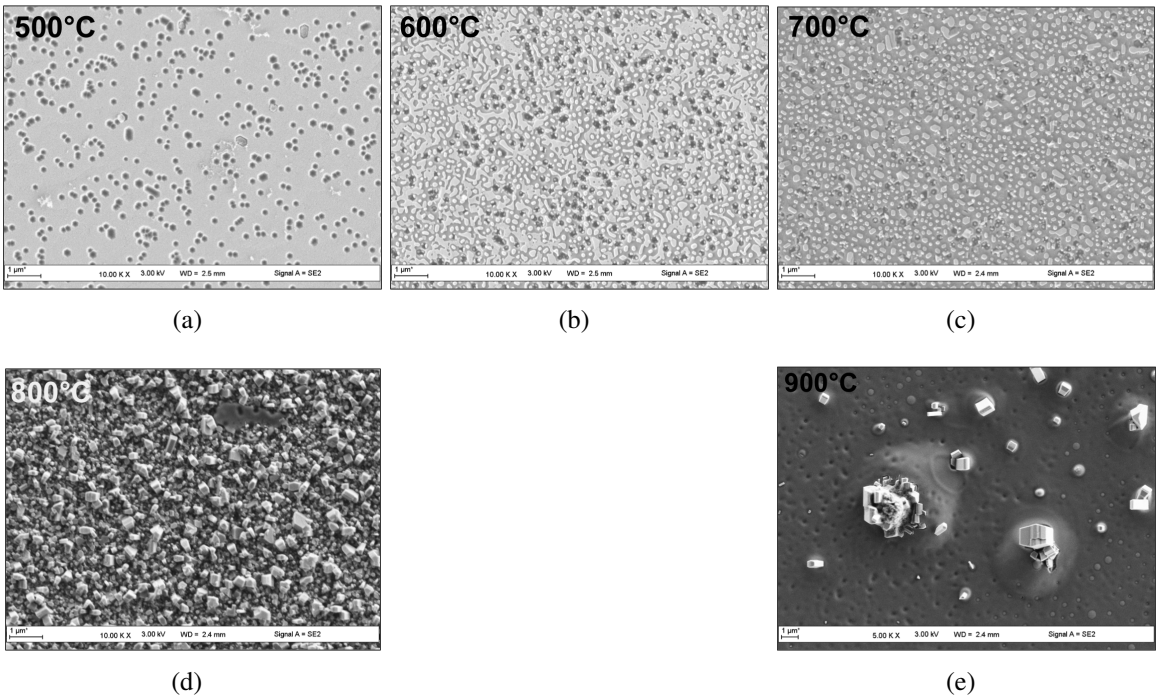

(a) (b) (c)

(d) (e)

Figure 68. SEM images of the structural integrity and morphology of the Pt gate at different temperatures

allowed electrical measurements up to 600°C. We observed the same behavior for each of the contacts, with the aluminum pads becoming electrically disconnected above 400°C. After this point, the probes were placed directly on the ohmic contacts for electrical measurements. Current-voltage measurements were taken from 25-600°C under ambient conditions. While morphological changes occur with the contacts, the device continued to function at 600°C even with exposure up to 45 minutes (Figure 69).

The conclusions of this study are that the Pt gate is limiting factor for the maximum operating temperature, which is 500°C for this device. Even though the device is still operational until 800°C, the severe morphological changes in the gate and ohmic contacts make this an unreasonable operating temperature for a commercial device. Therefore, packaging considerations should include protecting the sensor from temperatures above this critical point. It should be noted that the critical temperature is likely a function of the Pt thickness, and therefore will not be the same if different Pt thicknesses are used as a selectivity

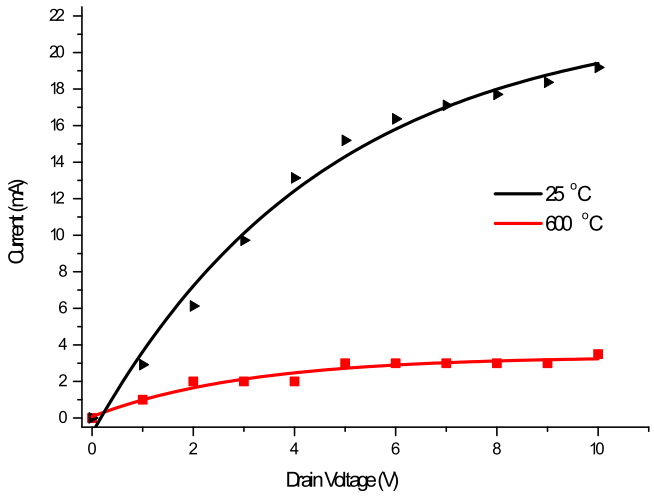

Figure 69. Current-voltage characteristics of the HEMT device at 25°C and 600°C

method. One possible packaging solution involves the use of housing the sensor in a separate compartment at a lower temperature and flowing the sample gas through a series of channels to cool the exhaust gas before it reaches the sensor. This part of the project is outside of the scope of this thesis, but is included in the future work and will be studied in detail at a later time.

CHAPTER 4

OTHER APPLICATIONS: LIQUID POLLUTION DETECTION AND WIRELESS SENSING

4.1 HEMT based liquid pollution sensors

Detection of nitrates and phosphates in fresh water bodies (lakes, streams, etc) is another application that has direct environmental and economic implications. These chemical compounds are nutrients for algae and must be regulated to control algae bloom that causes damage to the fish and plant populations in the ecosystem. Current methods of nitrate and phosphate focus on chemical assays that require the user to bring a sample of water from the surface of the lake to a lab, where the chemical tests performed can take hours or days to yield results. While the results are highly reliable and can give accurate detection on the ppb range, the time required to obtain results is often inconvenient. Additionally, the samples are taken from several spots on the surface of the lake and do not give an accurate representation of the chemical profile of the lake as a function of depth. This is a big issue because the density of the water layers changes with seasonal temperature changes, causing turnover and redistribution of the pollutants at different depths. Therefore, it would be ideal to have a device that can accurately detect nitrate and phosphate levels in real time (on the order of minutes for this application), allowing the potential for a larger number of measurements for a more statistically significant concentration profile. Devices allowing a three dimensional profile including the lake surface and depth would also be an improvement over current techniques.

HEMT sensors, such as the ones developed for exhaust gas detection in the previous chapter, provide an inexpensive solution for disposable, real-time monitoring of water pollutants. The high bandgap structure of the nitride materials GaN and AlGaN allow them to be chemically stable in aquatic environments, even when exposed to caustic chemicals. One of the main innovations that these solid-state, transistor-based sensors provide for this

application is that they allow fast detection of the target pollutants compared to current techniques that require bringing water samples into the lab. The ability of the devices to obtain complete selective detection could provide valuable information regarding the chemical composition of the water sample. The sensors are small enough so that hundreds can be produced on a single chip, making it economically viable for each individual sensor to be disposed of after a single use. Additionally, these sensors have the potential to be integrated with a robotics platform that can scan several lake depths, providing a real time measurement of the three dimensional pollutant profile that could be sent to an external processing and monitoring system (Figure 70).

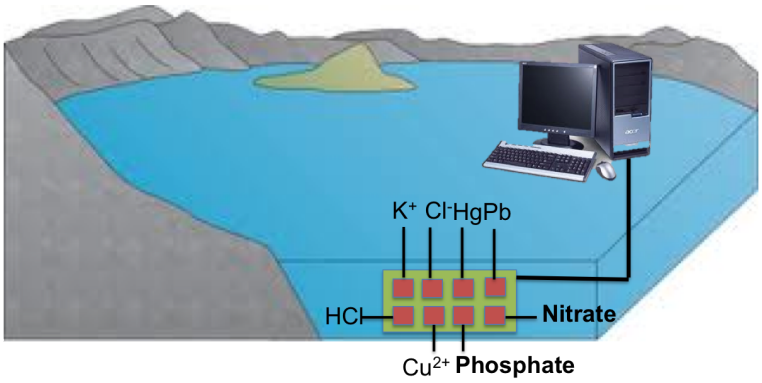

Figure 70. HEMT sensor designed with multiple integrated sensors functionalized for various liquid pollutants

HEMT sensors using an open gate have been developed and shown to be sensitive to liquids with varying polarity [82]. When subjecting the sensor to air, water, 50% acetone, and 75% acetone, the output signal remains detectable but varies significantly depending on the polar liquid. A second open-gate design was used for the detection of pH [83]; the device showed sensitivity between pH levels of 1.7 to 11.9, with higher signals for the more acidic solutions. Moreover, the linear region was very large for acids and decreased with more basic solutions. These two devices effectively show that HEMT sensors can operate in liquid environments, and that the polarity and pH can be adjusted for using an open-gate HEMT device. This can be used to calibrate other HEMT sensor designs that measure pollutants in a liquid environment.

Another open-gate HEMT sensor has been used to detect inorganic charged ions [84]. For a device grown with Ga-face, only a small effect is seen when exposing the HEMT to positive ions, but upon exposure to negative ions a current drop occurs that corresponds to a resistance increase of four orders of magnitude. Along with this high sensitivity, the response time is only 0.6 seconds and the recovery time is 150 seconds. For the N-face device, the effect is similar but the sensitivity is slightly reduced; a small resistance change occurs when the gate is exposed to positive ions, but there is a resistance change of three orders of magnitude when the gate is exposed to negative ions. This is coupled with a slower response time of 6 seconds, but a faster recovery time of 70 seconds.

A HEMT device using an ion-selective membrane in the gate region has been used to detect nitrates [85]. The membrane used in this HEMT device was originally developed for an ion-sensitive field effect transistor (ISFET) device and is selective for nitrates. However, the HEMT device reached a detection limit of 6.2ppb, which is much lower than the analogous ISFET. This indicates that HEMT sensing devices have the potential to reach sensitivities that are superior to the leading methods currently on the market, even when the sensing area consists of similar materials. We are currently investigating several possible gate materials that can be used in a HEMT device in order to detect phosphates in liquid environments. These gate designs are based on materials that have the ability to adsorb or filter phosphates and nitrates and may be incorporated into the HEMT structure to functionalize the gate.

A HEMT sensor with a gate functionalized with gold has been used to selectively detect Hg^{2+} from Cu^{2+} and Pb^{2+} with a detection limit of 200ppb [86]; functionalizing the gate with thioglycolic acid on a layer of gold results in a device that is sensitive to Hg^{2+} and Cu^{2+} with detection limits of 20ppb and 6.3ppb, respectively. This device is also selective against Pb^{2+}. Thus, it is possible to use the two HEMT sensors together in order to selectively detect both Hg^{2+} and Cu^{2+} at concentrations over 1000 times smaller than the leading market standard.

4.1.1 Experimental Setup

An experimental setup designed for testing our devices in liquid environments was developed at the Laboratoire Materiaux Optiques, Photonique et Systemes (LMOPS) in Metz. The setup was developed as an extension of the gas sensing setup and is integrated with the equipment already in place for the previous experiments of exhaust gas detection (Figure 71). Two tungsten probes plated with gold were assembled with directional position controllers in three dimensions and connected to an aluminum sample holder. Two micro pumps, optimized for 30ml/min flow when powered by a 6V supply from a Kiethley 2602 DC voltage supply, were connected as input and output pumps by plastic tubes sealed with silicon at holes on either side of the sample holder. The two probes are connected to a Kiethley 236 measurements system for IV measurements. Both voltage supplies are controlled using an automated LabView program that was developed in-house. The measurement setup has the possibility of operating in two possible modes: (1) static measurements where the liquid is pumped in until a certain volume, and the measurements are taken at a constant volume with no flow rate for a given pollutant concentration, and (2) dynamic measurements where the output pump is connected to the input pump, creating a closed loop for measurements under a constant volume and flow rate (30ml/min) for a given pollutant concentration. The measurement setup is pictured in Figure 72.

4.1.2 Device Fabrication

The HEMT device was grown by MOCVD in a T-shaped reactor using trimethylgallium and ammonia as the gallium and nitrogen sources, respectively, with nitrogen as the carrier gas. Undoped GaN layers of 200 and 61 nm were grown on an Fe-doped semi-insulating GaN template on a sapphire substrate, followed by 24nm of AlGaN with an Al composition of 30%, which was verified by XRD measurements. AFM shows an RMS of 0.6nm and V-defect density of $6.4 \times 10^{8} cm^{-2}$.

The device used in this study was T1192 from Table 8. In the mask designed for gas sensing (discussed in chapter 3) 3/4 of the mask was dedicated to gas sensor devices with

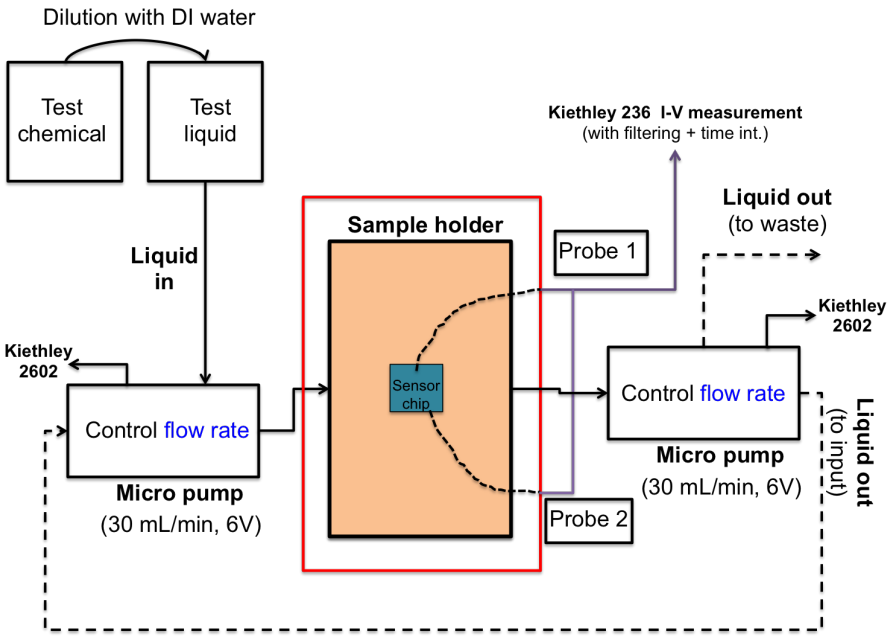

Figure 71. Schematic of the liquid sensor experimental setup, constructed at LMOPS and integrated with the gas sensing setup

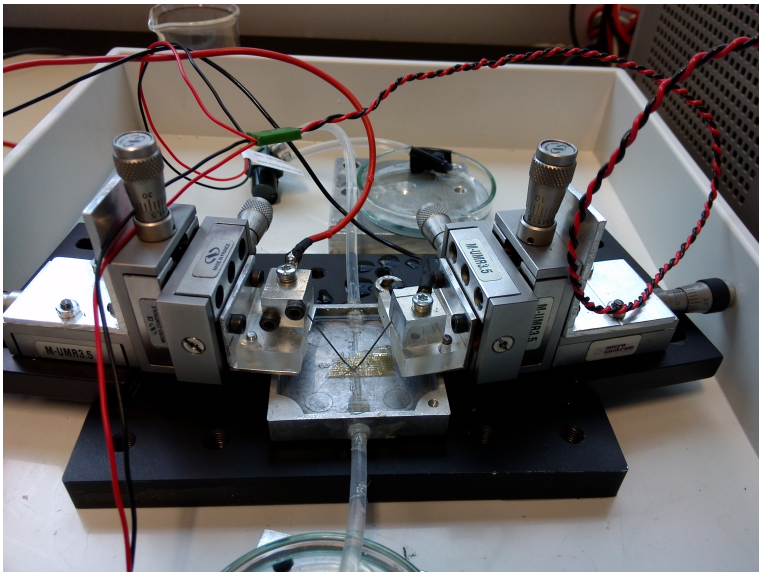

Figure 72. Photo of the liquid sensor experimental setup

Pt gates and the remaining 1/4 of the patterns were left as open gate HEMTs (Figure 73). The only difference in the mask design and process flow is that the Pt layer, and thus Pt deposition, is not included and the passivation blocking layer leaves a bare AlGaN surface as the sensing area, where the Pt gate would go for the gas sensor (Figure 74). The sensing

area dimensions are therefore the same as the gate dimensions for the gas sensors. This serves two purposes. First, the devices can be used as open gate HEMTs for liquid pollution to characterize the sensitivity of various chemicals by directly interacting with the AlGaN surface. Secondly, it allows the possibility for future functionalization of the gate using different gate materials that may provide a pathway for selective liquid pollution sensors.

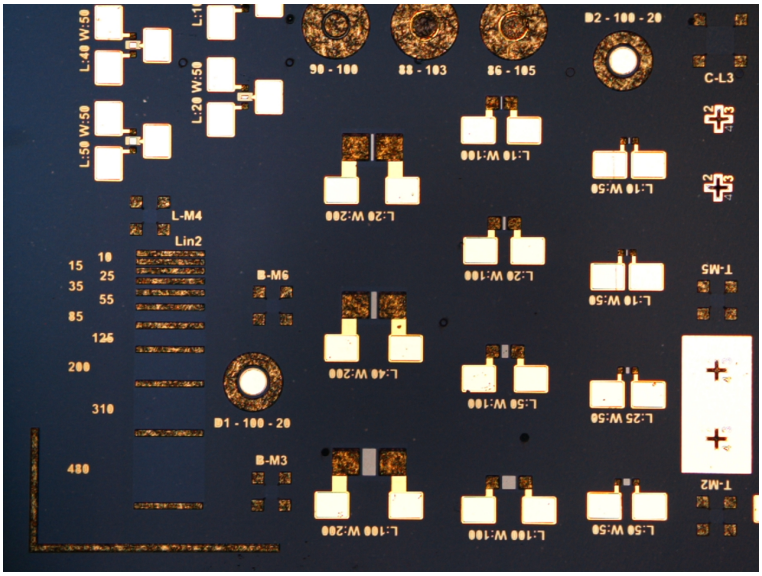

Figure 73. Optical image of the HEMT liquid sensors using an open-gate design

4.1.3 Experimental results: HEMT sensor for polar liquids

The open-gate HEMT sensors were tested for sensitivity for a variety of polar liquids. In this experiment, we used deionized water (dipole moment of 1.85D) and acetone (dipole moment of 2.91D) as the test liquids. The current-voltage measurement of the HEMT was taken in static mode, with the HEMT submersed in a volume of 10mL of liquid for each measurement and compared with the signal under atmospheric air. The results are shown in Figure 75.

The sensor shows sensitivity of 6.45% in DI water compared to atmospheric air at a drain-source bias of 10V. After the measurement in DI water, the water was pumped out and the sample was allowed to dry at room temperature. This reset the sensor signal back to its original signal under air. The acetone was then pumped in at the same volume and static

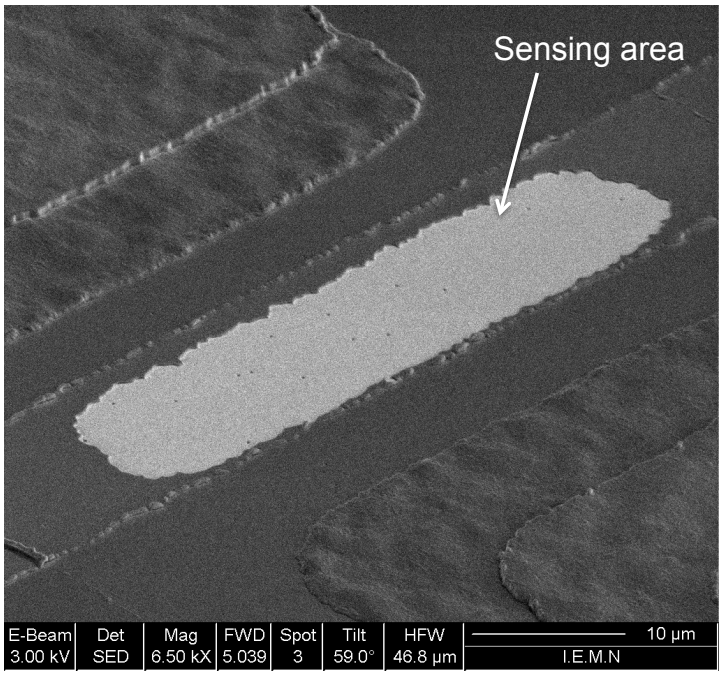

Figure 74. SEM image of the HEMT liquid sensor showing the open-gate sensing area

measurements were taken until the signal reached its maximum current change, indicating the steady state response of the sensor. The sensitivity of the HEMT to acetone was 10%, which is higher than the sensitivity to DI water. The signal again returned to its initial value when allowed to dry. This agrees with the results reported for a similar experiment by [82]. The ΔI and sensitivity of the device is directly linked to the dipole moment of the liquid. Since there is no gate, the liquid fills the sensing area that is exposed to the AlGaN surface. This liquid medium forms a pseudo-gate, with a work function defined by the dipole moment. The larger the dipole moment of the liquid, the larger the change in Schottky barrier height. In this case, the barrier height is increasing, causing a decrease in the sensor signal.

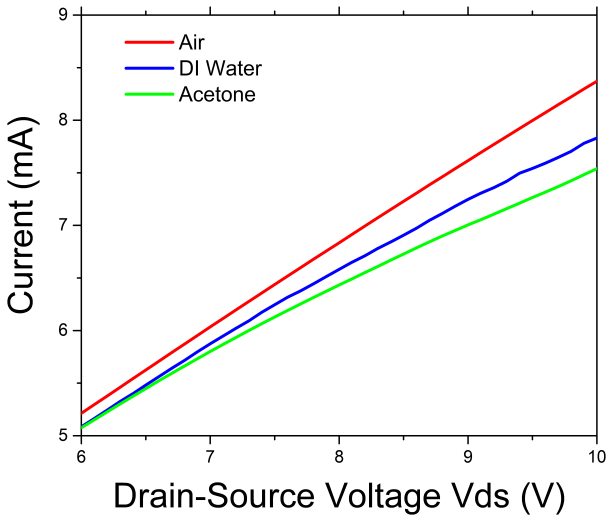

Figure 75. HEMT sensor sensitivity to different polar liquids

4.1.4 Experimental results: HEMT sensors for detection of phosphates and nitrates in water

A similar experiment was carried out to test the HEMT sensor response to nitrates and phosphates. To obtain the test liquid, potassium nitrate (KNO_3) and dihydrogen potassium phosphate (KH_2PO_4) soluble salts were diluted in water to obtain 1000ppm. In water, these salts dissolve into potassium and either phosphate (PO_4^{3-}) or nitrate (NO_3^-), respectively. As was the case for the polar liquids, the liquid medium forms a pseudo-gate on the exposed AlGaN area. The phosphate and nitrate ions can then interact with the interface traps and further change the Schottky barrier height. The experimental procedure to test the sensor response to 1000ppm of each of these ions was identical to the procedure outlined in the previous section for polar liquids. With exposure to ions, the sensor required a reset by rinsing with DI water between measurements to return the sensor to its initial current. The measurements were taken as two separate experiments using two different sensor devices. The phosphate detection was performed using a sensing area of 20x100um while the nitrate detection was tested on a HEMT sensor with a sensing area of 50x100um. The results for phosphate and nitrate detection are shown in Figure 76.

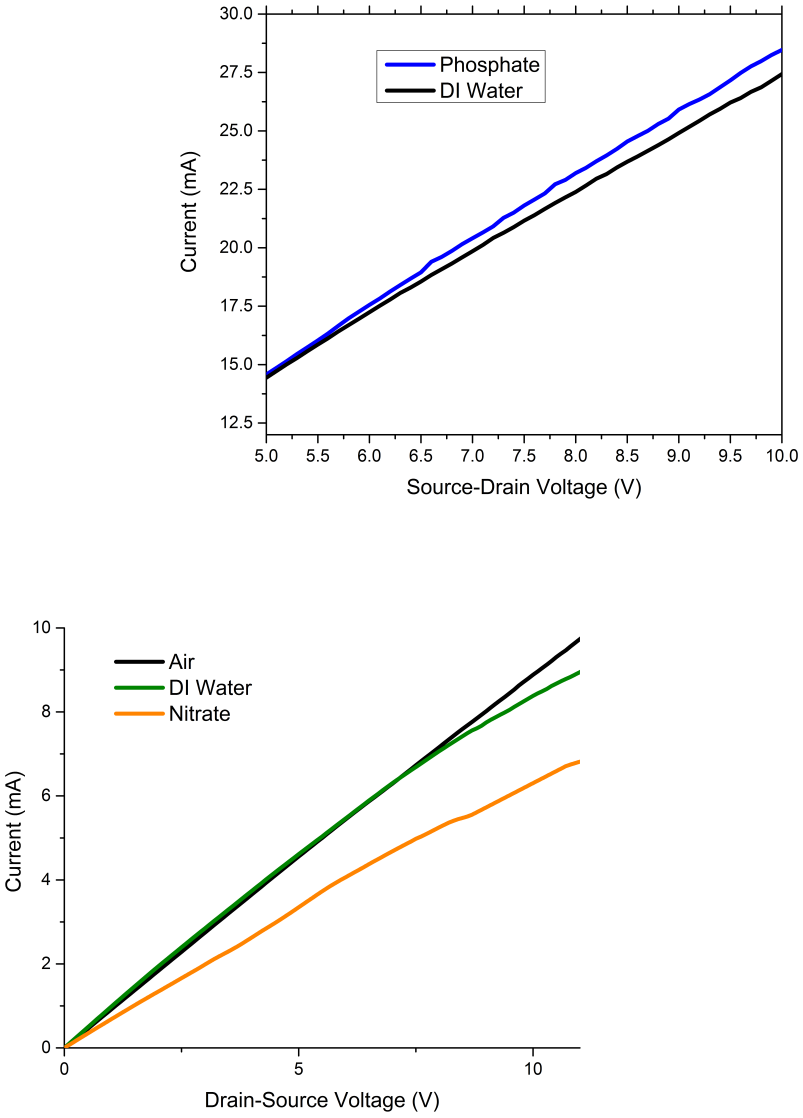

Figure 76. Detection of phosphate and nitrate in liquid using the HEMT sensor

The HEMT sensor shows a large response to both phosphate ions and nitrate ions (at 1000ppm) in DI water. A ΔI of 2.5mA and relative sensitivity of 9.1% was shown for exposure to the phosphate solution. This is the first time that phosphate detection has been reported using a HEMT sensor. A ΔI of 2mA and relative sensitivity of 25% was shown for exposure to the nitrate solution. While we can't directly compare the phosphate and nitrate results due to different sensing areas, these experiments give a very good indication that HEMT sensors are a promising option for phosphate and nitrate detection. Furthermore, the fact that the signal response is in the opposite direction for nitrate and phosphate could provide selectivity between the two chemicals. Future experiments are planned to test several concentrations of the two chemicals for a larger range of sensing area.

It may be possible to adapt the HEMT gas sensors for the selective detection of phosphates and nitrates in water by modifying the gate material. Instead of using an open-gate design as in our first experiments, or Pt as in the exhaust gas sensors, we propose to use either an open-gate design or specific adsorbing materials in combination with materials that can filter out unwanted chemical species. Several possible materials along with their design considerations have been identified and are listed in table 11 [87–90], along with relevant designs reported in literature.

Table 11. HEMT gate functionalization options for nitrate and phosphate detection in water

Target molecule	Gate design	Design considerations	Predicted detection limit
Nitrates	ion selective membrane		6.2ppb [85]
	polymer selective membrane	filtering mechanism	ppb
Phosphates	Zirconium hydroxide membrane	increase selectivity by comparing to sulfate specific HEMT	ppb
	Fe^{3+} oxide nano particles	calibrate pH with open-gate HEMT	ppb
	TiO_2	reversible using basic solution	ppb
	variable charge minerals		ppb
	Al(OH)x-oxalate		ppb
	Aluminum hydroxide		ppb
	Manganese(IV) hydroxide		ppb
	polymer selective membrane	filtering mechanism	ppb

The functionalization of the gate in this manner could provide selective chemical sensors. The HEMT sensor model (chapter 3) was modified to estimate the sensitivity of liquid sensors by removing the Pt gate and changing the dipole moment to that of water (1.85D);

this allows us to obtain a conservative estimate of the expected sensitivity. From the simulation results shown in Figure 77, we can expect ΔI= 1-10 μA at 6ppb, which corresponds to S=0.5-40% depending on the concentration of interface traps and the chosen functional layer (this part will need to be experimentally determined). This current range is readily detectible using standard equipment, and thus we can predict that our sensor designs should behave similarly to those already reported in the literature.

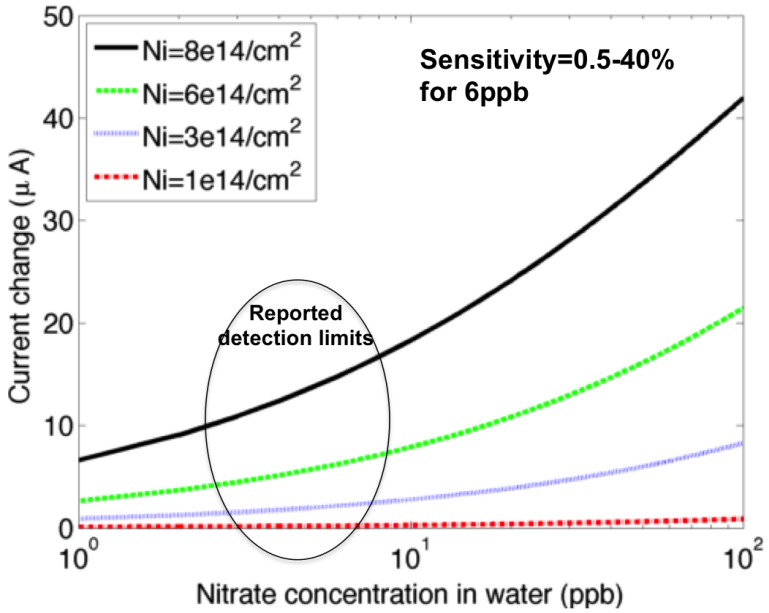

Figure 77. Simulation and expected results of HEMT nitrate sensor in water match closely with reported detection limits (ppb) of devices in the literature

4.2 Wireless HEMT sensors using split ring resonator devices

For both gas and liquid pollution detection, there are considerable advantages for wireless sensing options. One of the limiting factors for very high temperature applications is the metal contacts needed to apply voltage to a device. A device that doesn't need an applied voltage, on the other hand, could operate without these contacts allowing for much higher operating temperatures. Additionally, sensors that don't require electrical connections are ideal for operation in liquid environments. Finally, the processing and packaging steps could be significantly simplified for these devices, making the pathway for high throughput

commercial devices much more viable and cost effective.

We have developed an option for obtaining a wireless gas or liquid sensors by combining the HEMT and Schottky-based sensors developed in this thesis with a split ring resonator (SRR) device. An SRR is a type of metamaterial that takes advantage of electromagnetic resonance. There has already been some interest in using various metamerials for sensing applications, but it has not been reported using Schottky diode or HEMT sensors [94]. The SRR structure consists of two concentric rings each having a split. The structure acts as an LC circuit whose magnetic dipole resonates at a given frequency and acts as a waveguide by blocking the EM transmission at this frequency; the closed ring device, on the other hand, does not demonstrate a resonance frequency. The resonance frequency is a function of the capacitance across the split gap or the gap between the rings, given by $\omega_0 = 1/\sqrt{LC}$. Thus it is possible to change the resonant frequency by changing the split widths, adding a capacitor across the split, changing the metal or width dimensions, or changing the number of splits [95].

The SRR principle was experimentally tested using an SRR devices was developed at Georgia Tech using copper rings on an epoxy circuit board with split and ring gaps of 0.2cm (Figure 78). A 1pF capacitor was placed across the gap to reduce the resonant frequency below 3GHz (a limitation of the equipment available). An experimental setup was built by constructing two monopole antennas with a length of 5cm connected to an HP/Agilent signal generator and spectrum analyzer. The antennas were mounted to a wooden board with space for the SRR to fit between them with 0.5cm on each side. The device shows a strong resonance at 1.45GHz that is not present with the closed ring resonator (Figure 79).

The experiment was repeated using a single ring design with the same dimensions as the outer ring of the double ring SRR used in the previous measurement, with one closed ring resonator fabricated for reference. Capacitors ranging from 0.47 to 10pF were soldered across the gap, shifting the resonant frequency of each device. The transmission spectra is shown in Figure 80.

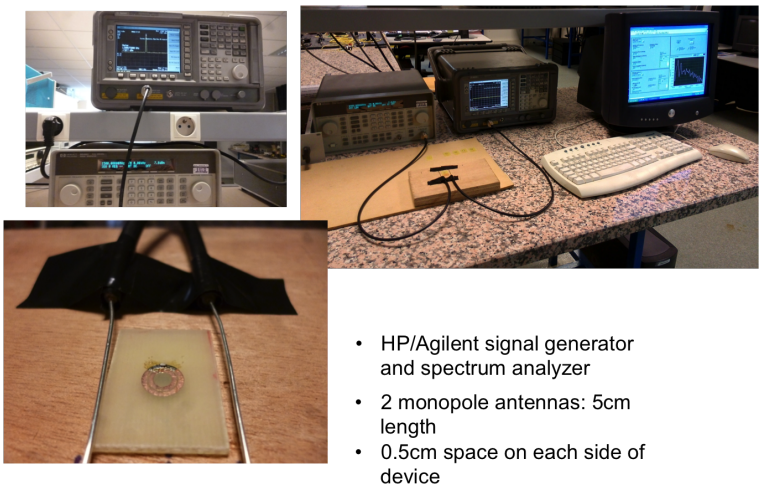

Figure 78. Split ring resonator experimental setup

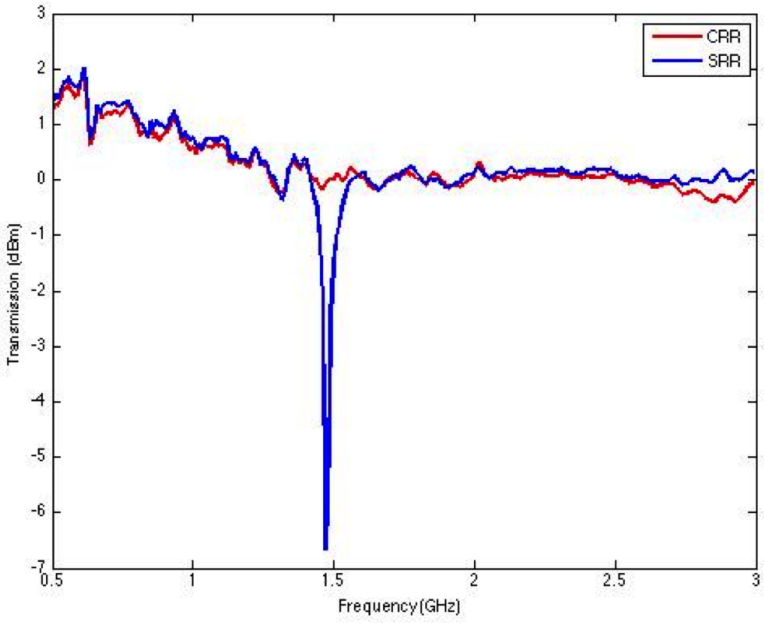

Figure 79. Split ring resonator measurement using the double split ring design with a 1pF capacitor across the gap; strong resonance is shown at 1.45GHz

The resonant peaks behave as expected. For a low capacitance, we see a strong resonance peak at a higher frequency; as the capacitance is increased, the resonance frequency is shifted down and the amplitude of the resonance is attenuated. For a capacitance of 1pF across the gap, we see a slightly lower resonant frequency with lower amplitude for the single ring design compared to the double ring, as expected.

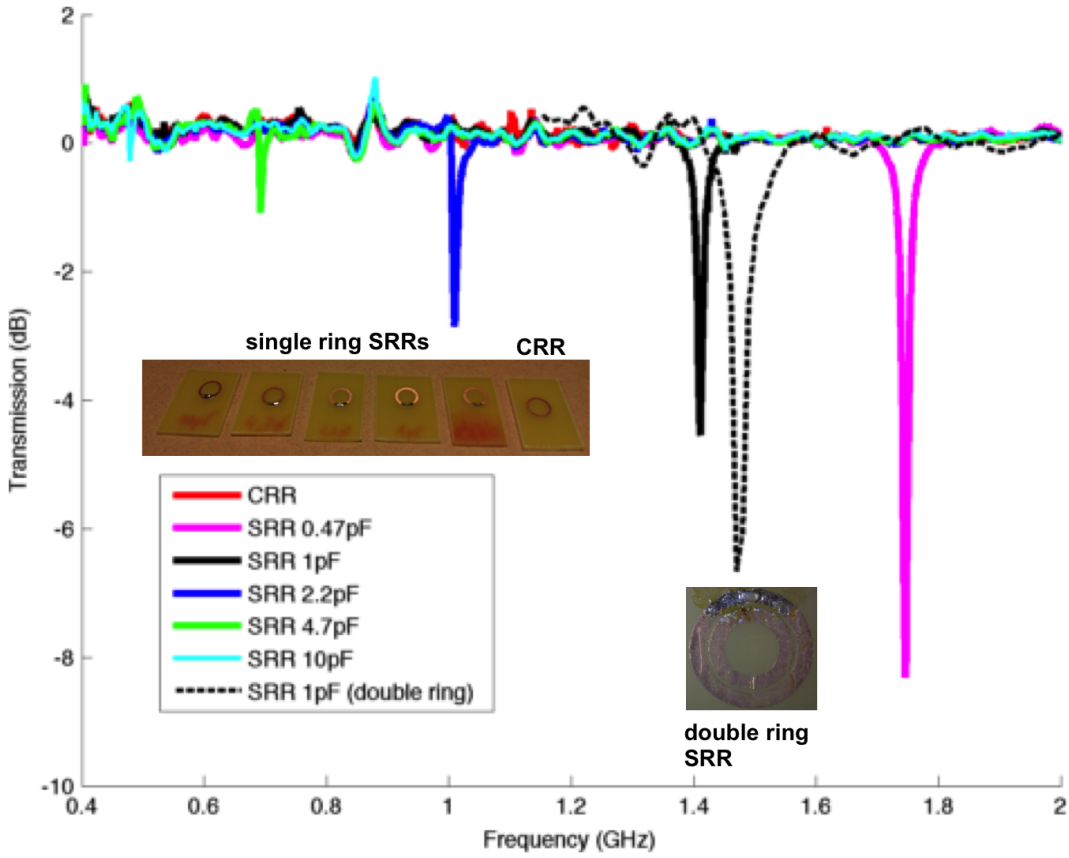

Figure 80. Split ring resonator measurements using single ring designs tuned for various resonant frequencies

Using these preliminary results, a concept for a sensor device was designed based on the following idea: since the capacitance across the HEMT changes upon gas exposure, we can place a HEMT between the split or ring gap so that the gas induces resonance frequency shift of the SRR. A schematic of this design is shown in Figure 81. With this design, a small change in capacitance results in a large frequency shift, increasing the sensitivity of the device. The design has the added benefit that the only contact needed is the functionalized Schottky contact since the capacitance is not directly measured, and therefore it can potentially reach higher temperatures than a fully contacted device. Additionally, the sensing area can be expanded to cover the entire AlGaN surface to sample a larger volume of gas.

The device can be configured in two possible modes: (1) connecting the SRR with the

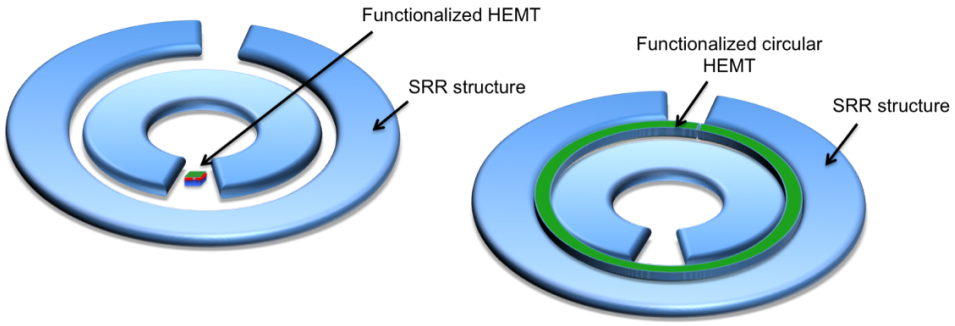

Figure 81. Designs for HEMT sensor devices integrated into split ring resonators

source and drain of the HEMT to cause a shift in the resonance intensity, or (2) connecting the SRR with the source and the gate of the HEMT to cause a frequency shift. The latter has the potential to be extremely sensitive, as shifts in frequency are calculated to be on the order of 10MHz, which is easily detectable using cheap, available technology that is already in use in devices such as cell phones. If the HEMT sensors are designed to be selective using one of the methods outlined in this thesis, different sensors designed for specific target molecules on a single chip could be connected to an SRR with a set frequency, and effectively be ”tuned” to operate at that frequency.

The main challenge for this device is the microfabrication process. It could be possible to grow the HEMT, and then selectively etch the area for the rings. For the rings, it would be beneficial to use tungsten instead of copper for high temperature applications since copper oxidizes at relatively low temperatures. After depositing the Pt gate on the HEMT, the rings could be deposited using evaporation or sputtering while masking the HEMT structure. For device testing, we can combine the SRR setup already constructed with the setup that we have constructed and used for gas testing (chapter 2).

While microfabricating an SRR with an integrated HEMT device would be the ideal solution, we attempted to perform a proof of concept using the HEMT gas sensors developed in this thesis. A piece of the T1192 sample with gas sensors was glued to a circuit board and sensors were connected with two SRRs designed to resonate at 1.7 and 1.4 GHz

(Figure 82). Two versions were constructed using both operation modes (intensity shift and frequency shift).

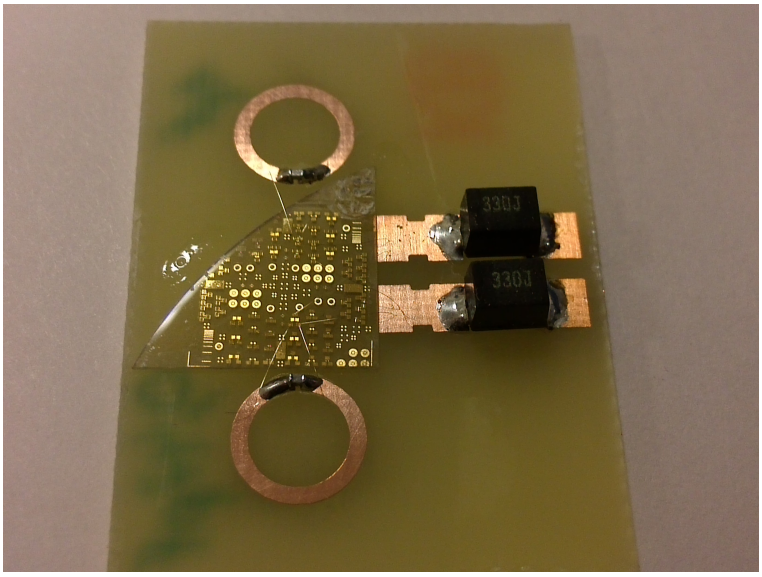

Figure 82. Prototype of HEMT gas sensor integrated with SRR for wireless sensing

The connected HEMT/SRR devices showed no resonance, as expected. This is because the HEMT is normally on with a 0V gate bias, so electrically connecting the SRR through the 2DEG channel creates a closed loop with very little capacitance across the gap, resembling the closed ring device. A negative voltage was then applied to the gate using a DC voltage supply to simulate the presence of one of the exhaust gases (since each gas causes a decrease in the sensor signal). Inductors were placed between the DC bias electrodes and the HEMT contacts to separate the AC and DC signals. We predict that at some negative gate bias, the device will again become resonant, and the frequency will shift in the device connected between the gate and source. At this point, the results are still inconclusive. It may be that the gold microwires used to connect the HEMT contacts to the SRR are too long, creating too much resistance. A microfabricated device would avoid this issue, and is planned as part of the future work of this project.

CHAPTER 5

CONCLUSION

5.1 Summary of the work

In this work we have developed new microsensor technology for the detection of exhaust gases (NO, NO_2, and NH_3) that shows excellent performance in terms of sensitivity, selectivity, thermal stability, and response time. The sensors that were developed in this thesis provide promising options for next generation sensors for use in the diesel SCR exhaust system and for meeting the upcoming European diesel exhaust regulations. Two main sensors options have been developed and studied for this application.

Double Schottky junction sensors based on BGaN/GaN superlattice structures show high sensitivity and responsivity to NO_2 gas compared to other devices reported in the literature, and provide the best tradeoff between the two metrics. Fast response times on the order of seconds were measured, and a linear response was shown for temperatures below 300°C. With this device, we showed, for the first time, complete selectivity to NO_2 for metal-semiconductor type sensors by optimizing the morphology and thickness of the Pt sensing layer. This selectivity method is currently being used to develop selective devices for NO and NH_3 in a second generation of BGaN sensors.

AlGaN/GaN HEMT sensors were developed using a thin Pt gate designed for the detection of NO, NO_2, and NH_3. An analytical model was developed to optimize the HEMT sensor design for a variety of material, environmental, and operational parameters. The optimized HEMT sensors that were fabricated in this study showed excellent sensitivity to each of the three studied exhaust gases. Detection of NO was shown for the first time using a HEMT sensor. Sensitivity to NO_2 was significantly higher than for previous HEMT sensors, and we were able to detect a concentration of 150ppb NH_3, which is the lowest reported concentration detected by either HEMT or Schottky-based sensors. For each gas, the sensor response is characterized for large concentration (10-1000ppm for NO and

NO_2 and 1.5ppb-15ppm for NH_3) and temperature ranges (25-400°C). This is the first time that this level of detailed characterization has been performed for these gases for HEMT or Schottky-based sensors. The information obtained about the optimal temperature and response times for the different gases can be utilized to improve device selectivity.

We also showed good agreement between our analytical model and the experimental results. This lead us to the development of novel selectivity methods by characterizing different reaction mechanisms for the different gases and extracting previously unknown information about the chemical mechanisms from the model. This is the first time that the different reaction mechanisms for NO and NH_3 have been characterized. A complete kinetic analysis of the various reaction mechanisms revealed that the response time and reaction rates can be used to identify individual gases from an exhaust gas mixture. Other information about the energy of adsorption was obtained from the kinetic analysis, and may lead to novel characterization techniques of determining interface trap concentrations.

A thermal fatigue test showed that the sensor structure can operate until 800°C, but that structural and morphological damage to the ohmic contacts and Pt sensing layer limit device operation to 500°C. This leads us to several packaging considerations for preventing damage to the sensor for exhaust applications. Long term stability tests showed that humidity can affect the sensor at temperatures below 100°C which can cause inaccuracies during a ”cold start”; however, at temperatures above 100°C we find that the sensor signal is stable for durations of at least 12 hours (this testing duration is limited by the testing equipment). Thicker Pt layers seem to protect the device from this humidity affect, and may be a good option for use during the cold start.

The HEMT sensors also show dynamic time response of at least 1 second, which is on the order of time needed for exhaust gas sensing. The sensors were tested in the simulated exhaust conditions with varied concentrations and time durations and showed measurable response under these conditions for all three gases. The different dynamic time responses of the three gases may be another method of selective detection.

We have also shown, using the HEMT sensor, successful detection of both CO_2 in a mixture of exhaust gas and N_2O gas. This is the first time that a HEMT sensor has been used to detect N_2O. The reaction mechanisms observed from the detection of these two gases are similar to the ones that we already characterized for NO, NO_2, and NH_3. This means that the work done on these exhaust gases, including the information about chemical mechanisms and our new selectivity methods, can be transferred to other gases in addition to the ones focused on in this thesis. This means that the work done in this research can be translated across a broad range of applications.

In addition to developing sensors for gas detection, we also developed HEMT sensors for the detection of nitrates and phosphates in liquid. This was the first time that phosphate detection has been shown with this type of sensor. HEMT sensors may therefore be an attractive option for cheap, disposable sensing devices for water treatment applications, and can easily be integrated with a robotics platform for obtaining real-time, three-dimensional concentration profiles of pollutants in fresh water bodies.

We also began the design and development of wireless sensors that integrate our gas and liquid HEMT sensors with split ring resonator devices. These devices provide a promising option for high sensitivity, frequency-based measurements. Additionally, the ohmic contacts can be imbedded in a microfabricated structure, providing a pathway for devices that can operate at very high temperatures. These devices also provide the unique ability to tune the sensor signal for operation at different frequencies, so that selective HEMT sensors designed for various target molecules can operate at a given frequency, and antennas operating at different bandwidths can easily distinguish between the sensor signals.

5.2 Future work

This work was carried out as a part of a larger project aimed at developing next generation sensors for SCR systems in the diesel exhaust. While many of the goals of the overall

project were completed during this thesis, there are still many aspects that need to be explored further in order to move towards the development of commercial sensor devices. One of the biggest aspects will be to further optimize the devices that were developed during this research in terms of repeatability, long-term stability, and response time. The methods that we have developed for selectivity also need to be further explored and optimized through the use of more realistic measurements in exhaust conditions. Some of the methods, such as the use of response time and reaction rates, requires extensive signal processing techniques that have not yet been developed. In addition to the selectivity methods developed in this thesis, it may also be possible to achieve selectivity using various functional layers, and this is a point that should be explored in the next generation of HEMT and Schottky sensors developed at Georgia Tech Lorraine. The results obtained from studying the sensing properties of the BGaN material in our Schottky diode device can be applied to the more complex HEMT design in a future generation of HEMT sensors. For example, we have designed one device that uses an AlGaN/GaN HEMT structure with a 2nm BGaN cap layer; this device utilizes the unique sensing properties that we found for BGaN materials and combines it with the advantages of the HEMT device.

In order to test the sensors in more realistic conditions, such as in an actual exhaust system, the sensors will need to be packaged. This provides both the ability to connect the sensor in the current exhaust system and a method of protecting the sensor from damage at temperatures above 500°C. This work is already being planned as part of the next steps of the project.

The technology developed in this thesis can also be adapted for other applications besides exhaust gas sensing. As we have seen, these sensors are promising options for the detection of liquid pollution such as nitrates and phosphates. Future work for this application includes the addition of functional layers to improve device selectivity. Another application that we have briefly discussed is the detection of harmful gases inside the cockpit of the car. For these sensors, the concentration changes are likely to be much slower

than the inside of the exhaust, and therefore the transient analysis technique for selectivity could be adapted for this application. Similarly, the sensors could be adapted for industrial applications, such as detection of NH_3 leaks in refrigeration applications or CO_2 monitoring in food and beverage plants; we have also looked at NH_3 monitoring in chicken houses. It may in fact be beneficial to further develop each of the different device types explored in thesis as a function of the requirements of specific applications. For example, if an application focuses more on robust sensors that do not degrade easily rather than extremely low detection limits (e.g. chicken houses), the Schottky device may be a better option for commercialization due to easier processing and potential for scalability. Other applications may require the more complex HEMT devices that provide lower detection limits. In any case, the foundation of microsensor technologies that we have developed in this thesis needs only to be slightly modified in order to adapt it to new applications, meaning that these devices can be used over a large range of potential markets.

REFERENCES

[1] A. Ougazzaden, C. Bishop, J.P. Salvestrini, P.L. Voss, L. Pradere, Y. Halfaya. Capteur Schottky de detection d'un constituant d'un gaz d'chappement. **FR 1462277** 2014.

[2] A. Ougazzaden, C. Bishop, J.P. Salvestrini, P.L. Voss, L. Pradere, Y. Halfaya. Capteur de detection d'un composant d'un gaz **FR 1462278** 2014.

[3] C. Bishop, et al. Applied Physics Letters 2015. (in review)

[4] K. Pantzas Journal of Crystal Growth **370**, 57(2013).

[5] N.P. Ngwangchang, Y. Lee, M. Alam, C. Bishop, and P.L. Voss LPHYS 12 (2012).

[6] K. Pantzas, et al 16th International Conference on MOVPE (2012).

[7] G.E. Likens and F.H. Bormann Science **184**, 1171 (1974).

[8] P.N. Pearson and M.R. Palmer Nature **406**, 695 (2000).

[9] E.J. Miravete, M.J. Moral, and J. Thurk European Economic Association Econometric Society (2014).

[10] T. Klier and J. Linn Journal of Environmental Economics and Management **66**, 280 (2013).

[11] K.C. Stein, et al Ind. Eng. Chem. **52**, 671 (1960).

[12] G. Madia, et al Ind. Eng. Chem. **41**, 4008 (2002).

[13] A.D. Brailsford, M. Youssouff, E.M. Logothetis, and M. Shane, Sens Act B Chem **25**, 362-365 (1995).

[14] J.T. Woestman and E.M. Logothetis Ind. Phys. **1**, 20 (1995).

[15] D.Y. Wang, et al, SAE International 2008-01-0919 (2007).

[16] M. Radecka, K. Zakrzewska, and M. Rekas, Sens Act B Chem **47**, 194-204 (1997).

[17] A.D. Brailsford, M. Youssouff, E.M. Logothetis, Sens Act B Chem **26**, 135-138 (1993).

[18] R.L. Liu, et al, J. Inorg. Mater. **21**, 793 (2006).

[19] O. Lupan, S. Shishiyanu, L. Chow, and T. Shishiyanu, THIN SOLID FILMS **516**, 3338 (2008).

[20] H.J. Lim, D.Y. Lee, and Y.J. Oh, Sens Act A Phys **125**, 405-410 (2006).

[21] K.I. Shimizu, et al, Sens Act B **130**, 707 (2008).

[22] A.Z. Sadek, et al, ILW Sens. I **7**, 414 (2007).

[23] A. Sutti, et al. Sens Act B Chem **130**, 567-573 (2008).

[24] M.D. Ellison, M.J. Crotty, D. Koh, R.L. Spray, and K.E. Tate, JOURNAL OF PHYSICAL CHEMISTRY B **108**, 7938 (2004).

[25] I. Lundstrom, M.S. Shivaraman, C.M. Svensson, and L. Lundkist Appl Phys Lett **26**, 55-57 (1975).

[26] I. Lundstrom, M.S. Shivaraman, and C.M. Svensson, J Appl Phys**46** (1975).

[27] I. Lundstrom, C. Svensson, Solid State Chemical Sensors (1985).

[28] I. Lundstrom, M. Armgarth, A. Spetz, and F. Winquist, Sens and Act **10**, 399 (1986).

[29] I. Lundstrom, Sens and Act A **56**, 75-82 (1996).

[30] S.J. Pearton, et al, Progress in Materials Science **55**, 1-59 (2010).

[31] A. Spetz, M. Armgarth, and I. Lundstrom, Journal of Applied Physics **64**, 1274-1283 (1988).

[32] L.M. Lechuga, et al, Sens and Act B **8**, 249-252 (1992).

[33] S. Khan, E. de Vasconcelos, Y. Hasegawa, and T. Katsube, Brazilian Journal of Physics **34**, 557-580 (2003).

[34] J. Schalwig, G. Muller, M. Eickhoff, O. Ambacher, and M. Stutzmann, Mat. Sci. Eng. B Solid State Materials for Advanced Technology **93**, 207-214 (2001).

[35] I. Lundstrom, M.S. Shivaraman, C. Svensson, and I. Lundkvist, Appl. Phys. Lett. **26**, 55-57 (1975).

[36] C. Christofides and A. Mandelis. Journal of Applied Physics. **68** R1,(1990)

[37] V. Tilak, K. Matocha, and P. Sandvik Phys Stat Sol **2**, 2555-2558 (2005).

[38] J. Schalwig, G. Muller, M. Eickhoff, O. Ambacher, and M. Stutzmann, Sens and Act B-Chemical **87**, 425-430 (2002).

[39] V.V. Quang, N.V. Dung, N.S. Trong, N.D. Hoa, N.V. Duy, and N.V. Hieu, Appl. Phys. Lett. **105**, 013107 (2014)

[40] A. Spetz, M. Armgarth, and I. Lundstrom, Journal of Applied Physics **64**, 1274-1283 (1988).

[41] T. Chen, et al, IEEE transactions on electronic devices **58** (2011)

[42] M. Miyoshi, S. Fujita, and T. Egawa. Journal of Vacuum Science Technology B **33** 013001, (2015)

[43] T.Y. Chen, et al. IEEE electron device letters **33** 612, (2012)

[44] I. Vurgaftman, J. R. Meyer, and L. R. Ram-Mohan Journal of Applied Physics **89**, (2001)

[45] The Nobel Prize in Physics 2014 Prize Announcement. Nobelprize.org. Nobel Media AB 2014. Web. 2 Mar 2015.

[46] S. Gautier, et al, Journal of Crystal Growth **315** 288(2011)

[47] Ougazzaden, et al, J. Cryst. Growth **298**, 316 (2007)

[48] A. Ougazzaden, et al, Appl Phys Lett **93** 083118(2008)

[49] V. Ranvindran, et al, Appl Phys Lett **100** 243503(2012)

[50] J. Dickerson, et al, European Physical Journal-Applied Physics **60** 30101(2012)

[51] H. Srour, J.P. Salvestrini, A. Ahaitouf, S. Gautier, T. Moudakir, B. Assouar, M. Abarkan, S. Hamady, and A. Ougazzaden, Applied Physics Letters **99**, 10.1063 (2011).

[52] J.P. Salvestrini, A. Ahaitouf, H. Srour, S. Gautier, T. Moudakir, B. Assouar, and A. Ougazzaden, Quantum Sensing and Nanophotonic Devices IX, Proceedings of SPIE **8268**, (2012).

[53] J. Song and W. Lu, IEEE Sensors **8**, 903-909 (2008)

[54] R.B. Getman, et al, Phys. Rev. Lett. **102** 076101(2009)

[55] W.K. Offermans, et al, J. Phys. Chem. C **111** 17551(2007)

[56] E.L. Murphy and R.H. Good, Jr. Physical Review **102** (1956)

[57] C.R. Crowell Solid-state Electronics **8** 395 (1965)

[58] A.C. Schmitz, et al Semicond. Sci. Technol. **11** 1464 (1996)

[59] V. Gopal, et al. Journal of Applied Physics. **104** 124506, (2008)

[60] I. Lundstrom, M. Armgarth, A. Spetz, and F. Winquist, Sensors and Actuators **10**, 399-421 (1986).

[61] M. Ali, V. Cimalla, V. Lebedev, H. Romanus, V. Tilak, D. Merfeld, P. Sandvik, and O. Ambacher, Sensors and Actuators B-Chemical **113**, 797-804 (2006).

[62] H. Hasegawa, M. Akazawa, Applied Surface Science **254**, 3653-3666 (2008).

[63] T. Baghdadli, S. Ould Saad Hamady, S. Gautier, T. Moudakir, B. Benyoucef, and A. Ougazzaden, Phys. Status Solidi C 6(S2), S1029 (2009).

[64] K. Potje-Kamloth Chem Rev **108**, 367-399 (2008).

[65] K. Son, et al. IEEE sensors **11** 3476 (2011).

[66] O. Ambacher, et al, J Appl Phys **85**, 3222 (1999)

[67] M. Germain, et al. Mat. Res. Soc. Symp. Proc. **798** (2004).

[68] L. Wang, et al, Electron Devices **55**, 261-267 (2008)

[69] M. Chattopadhyay and S. Tokekar Microwave and optical technology letters **49** (2007)

[70] M.A. Huque, et al, Solid-State Electronics **53**, 341-348 (2009)

[71] H. Wang, et al, App Phys Lett **87**, (2005)

[72] Eliza, Sazia A. and Dutta, Achyut K. Advanced environmental, chemical, and biological sensing technologies VII **7673** (2010).

[73] S.J. Pearton, et al. Progress in Materials Science. **55** 1:1, (2010)

[74] Guo, et al. Sensors and Actuators B-Chemical **176** 241 (2010).

[75] N. DasGupta and A. Dasgupta, Solid-State Electronics **36**, 201-203 (1993)

[76] F. Schwierz, et al. Solid State Electron **49**, 6:889 (2005).

[77] Y.F. Wu, et al. IEEE Electron Device Letters **18**, 6:290 (1997).

[78] Akita, et al. IEEE Electron Device Letters **22**, 8:376 (2001).

[79] A. D'Amico, et al. Sensors and Actuators B-Chemical **144**, 2:400 (2010).

[80] H. Kim, et al. Sensors and Actuators B-Chemical **164** 1:64 (2012).

[81] V. Fiorentini, et al. Physical Review B **60** 12:8849 (1999).

[82] R. Mehandru, et al, Solid-state electronicsl **48**, 351-353 (2004).

[83] M. Abidin, et al, Sensors **11**, 3067-3077 (2011).

[84] R. Neuberger, et al, Mat Sci Eng B **93**, 143-146 (2002).

[85] M. Myers, et al, IMCS (2012).

[86] H.T. Wang, et al, Electrochemical and Solid-State Letters **10**, 150-153 (2007).

[87] N.I. Chubar, et al, Colloids and Surfaces A **255**, 55-63 (2005)

[88] R. Chitrakar, et al, Journal of colloid and interface science **297**, 426-433 (2006)

[89] G. Zelmanov, R. Semiat, Environmental engineering and management journal **10**, 1923-1933 (2011)

[90] H.J. Kim, et al Transactions of the ASABE **50**, 415-425 (2007)

[91] H.T. Wang, et al, Electrochemical and Solid-state letters **10**, J150-J153 (2007).

[92] P. Bergveld,, et al, Sens and Act B-Chemical **88**, 1-20 (2003).

[93] S. Rabbaa and J. Stiens Journal of Physics D: Applied Physics **45**, (2012)

[94] T. Chen, S. Li, and H. Sun Sensors 2742 (2012)

[95] K. Aydin, et al. New Journal of Physics **7** (2005).